Doctoral Dissertation
Doctoral Program in Chemical Engineering (36th cycle)

Fundamental Research, Design and Process Optimization for Magnesium Hydroxide Precipitation

Development and Application of Modelling Tools to Support the Circular Economy

presented by

Antonello Raponi

Supervisor(s):
Prof. D. Marchisio, Supervisor
Prof. M. Vanni, Co-Supervisor
Prof. A. Buffo, Co-Supervisor

Doctoral Examination Committee:

Politecnico di Torino
2024

Declaration

I hereby declare that, the contents and organization of this dissertation constitute my own original work and does not compromise in any way the rights of third parties, including those relating to the security of personal data.

Antonello Raponi
2024

* This dissertation is presented in partial fulfillment of the requirements for **Ph.D. degree** in the Graduate School of Politecnico di Torino (ScuDo).

“I wish you only one thing: the good fortune to always be in a situation that allows you to freely maintain the integrity I mentioned − not to feel compelled to lose it in order to keep your job, find funds, or whatever. May you have this freedom”

- Richard Feynman

Acknowledgements

I would like to express my deepest gratitude to *Daniele*, my esteemed *docktorvater*. Throughout this journey, you have been more than just a mentor; you have shown unwavering care and support not only for our research but also for us as individuals. Your genuine kindness and consideration have been invaluable, fostering an environment where learning and growth thrive. Your guidance and encouragement have been instrumental in shaping this thesis and shaping me as a researcher. Thank you for believing in my potential and investing your time and effort in my academic and personal development. Your dedication to teaching and research has been a profound source of inspiration, and I will carry the lessons I've learned from you throughout my career.

Thank you, *Mohsen* for being a reference point during the intense years of doctoral studies. Your brilliance was inspiring and allowed me to learn so much. Thank you for the discussions that have always benefited my research.

Thank you, *Andrea Q.* for always giving me a sense of boundless respect, for pushing me to give my best, for the knowledge and passion we shared about precipitation, and for the super top-secret collaborations that entertained me beyond belief.

Thank you *Claudia* and *Vincenzo* for the advice, but above all, for the sacred moments when drinking coffee we could share jokes and release some stress.

Thanks to all the master students I had the privilege to supervise. By teaching you, I learned from each of you.

I am also indebted to all the professors and colleagues from MuSyChEn and CREST groups to have contributed to my academic journey, offering their support and encouragement along the way. Your collective wisdom has made this endeavour even more fulfilling.

Thanks to Prof. *Mazzotti* for allowing me to spend six transformative months at ETH with his amazing research group.

Thanks to the research group at the University of Palermo for allowing me to do research in the context of the European project SEArcularMINE.

Sofia, the thanks I owe you are too wide, to the extent that being able to give proper credit seems impossible. Thank you for the boundless love, respect, and warmth you bestowed upon me. You have been the architect of countless smiles and shared moments and an unwavering pillar of support. In your embrace, I found solace, understanding, and the courage to confront life's challenges with newfound strength. You are more than a friend; you are a sister of the heart, a twin flame that the universe graciously gifted me. Through you, I have learned the profound art of caring for others, realizing that in nurturing those around us, we find the path to nurturing ourselves. Together, we shine like stars, lighting up the cosmos with the brilliance of a bond that time cannot dim.

Thank you, *Andrea A.*, for being a big brother over the years. Thank you for the laughs, the travels and the unfailing support. Thank you for teaching me not to settle, to express myself and to remain silent when it was not worth it. Thank you for the shared experiences and for continuing to share them, albeit far away.

Thank you, *Lorena*, for the wonderful relationship we have established in a short time. For the long talks back home, for the hearty laughs, and your great gift of understanding and insight just by observing. Thank you for supporting my ideas and thank you for allowing me to support yours. My last year as a PhD gave me so much, and you were the best surprise of all. Thank you

Thank you, *Elena*, for the big sisterly advice, for your high regard for me, and for the kind words you have spent on me since the beginning. Thanks for the deep chats over Spritz, fancy ice cream, and exhausting workouts (although as a PT I'm not up to Max's standards). Everything we said to each other made a difference inside me, helping me with important decisions.

Thank you, *Ramona*, for simply being yourself. You are the best and most generous person I have met, always ready to help others no matter how much time it takes away from you. Thank you for getting me through six months of exchange that I can never forget. Thank you for shared dinners accompanied by a good glass of red wine, desserts eaten on the couch, and walks along bahnhofstraße. Thank you for

making me rediscover the beauty of sports and for welcoming me with a kind smile whenever I needed it.

Thank you, *Brandon* and *Morgan*, because you are proof that you don't need to see or hear each other every day to keep a relationship alive. Thank you for your love and for the thought that, overseas, always reaches me

Thank you, *Fabia* and *Matteo*, for being my own little piece of Italy in Zurich. Thank you for the feeling that binds us, for the determination that we share, and for the boundless sweetness that overflows from your eyes.

Thank you *Valerio* for making me discover the beauty of music again and for reminding me that one should always stay true to one's own *rhythm*. Thank you for the sweetness and daily care you use and for that humour that makes me smile, especially my heart, even when I am exhausted. For everything else *ça va sans dire*

Dear *mamma*, here I am finally at this thanks. Needless to say, words will never be able to thank you enough for all you have done for me over the years. Thank you for the mother's love that was a gentle caress that accompanied me. Thank you for being an example of stubbornness and determination. But most of all, thank you for believing in my dreams, even when you didn't understand them. Thank you for giving me every tool in your power to get me started on this long journey although I know how much it cost you. I am grateful and thankful for everything you have taught me.

Thank you, *Leonardo*, for your lifelong support. Thank you for the trust you have always placed in me and for making me the repository of your fears and joys. I don't think I have always lived up to it, I have certainly made mistakes but our relationship has grown stronger through them and has been shaped by our dreams.

Thank you, *papà*, for being an example of calm and peacefulness and for helping me understand who I wanted to become. Thank you for teaching me to recognize the beauty that surrounds us and for educating me about kindness. But most of all thank you for teaching me that in life whatever happens to us or whoever we meet serves to help us get to know each other.

Thank you, *zia Grazia*, for being my person even though life has tested us. Thank you for the determination and care you invested in achieving your dream and for teaching me that even when the odds are slim, you have to strive. Thank you for being a testimony that you have to 'fight until you can't fight anymore'. Last but

not least, thank you my beloved niece *Nina Marie*. Thank you for being the living example of how strongly a dream can burn.

Thanks to everyone who, in one way or another, has been part of this journey. I take with me the lessons from each one.

Abstract

In recent years, the number of Critical Raw Materials (CRMs) has expanded and, among others, magnesium was included. Often dismissed as waste, brines and bitterns are found to contain high magnesium levels. Consequently, innovative circular economy-based processes have been devised to harness magnesium recovery. A sustainable alternative is the precipitation as magnesium hydroxide employing a reaction with an alkaline solution. The focus of the doctoral research is dedicated to the development of a computational modelling framework aimed at accurately describing the precipitation of magnesium hydroxide. The initial phase of the study involved characterizing mixing in both square and circular cross-sectional T-mixers. Experimental data describing the mixing of food dyes were acquired through image analysis and subsequently modelled using Computational Fluid Dynamics (CFD) with the β-Probability Density Function (β-PDF). This approach enabled tuning and validating the flow field and turbulent properties, which were critical for accurately describing the precipitation process.

Following the validation of the mixing characteristics, precipitation tests were conducted to gather experimental Particle Size Distribution (PSD) data under various operating conditions and reactor configurations. A T-mixer with a circular cross-section and constant diameter was employed to assess the impact of (i) initial magnesium concentration and (ii) flow rates. Additionally, a Y-mixer, featuring two diverging channels and a final pipe of constant diameter, was used to investigate the effects of extending (iii) the initial magnesium concentration range, specifically expanding it towards smaller concentrations.

Parametric identification was conducted following two approaches: (i) the first involved the use of traditional algorithms such as the Conjugate Gradient (CG) and the Particle Swarm Optimization (PSO) and (ii) the second involved the development of an innovative methodology involving the use of deep-learning algorithms.

Specifically, the second approach adopts the following procedure. Leveraging a Population Balance Model (PBM) coupled with Computational Fluid Dynamics (CFD) simulations of T- and Y-mixers, a numerical dataset was created to train a Neural Network (NN), referred to as the 'mirror model,' which predicts kinetics parameters based on experimental sizes. Notably, the PBM, fitted with the dataset (i), excels at describing changes in flow rate (dataset (ii)) and substantial reductions in reactant concentrations in the Y-mixer (dataset (iii)), even though these conditions were not encountered during the fitting step. Key Performance Indicators (KPIs) reveal that the mirror model consistently outperforms the CG and PSO, highlighting its remarkable potential for practical applications.

Finally, a three-dimensional one-way coupled CFD-PBM model was implemented to conduct the optimization of a prototype for the precipitation of magnesium hydroxide. In this regard, a collaboration between ResourSEAs and the University of Palermo resulted in the design of a pilot-scale prototype for magnesium hydroxide precipitation, patented by ResourSEAs S.r.l. The initial design process, based on trial and error, lacked a specific optimization tool. Addressing this gap, the research emphasizes the practical applications of modelling tools to support the circular economy and prototype optimization. The research navigates through analytical insights guiding the prototype's optimization, considering constraints imposed by the patent. This exploration offers a comprehensive understanding of considerations and decisions crucial to enhancing the innovative solution, aiming to bridge theoretical foundations with tangible outcomes and contribute to the advancement of magnesium hydroxide precipitation technologies.

Contents

List of Figures

List of Tables

Nomenclature

Roman Symbols

a_{eq}	equilibrium activity
$\mathbf{g}$	gravitational acceleration
$\mathbf{u}$	velocity vector
$\overline{u_i' u_j'}$	Reynolds stress tensor
C_μ	$k-\varepsilon$ model parameter
$C_{\varepsilon 1}$	$k-\varepsilon$ model parameter
$C_{\varepsilon 2}$	$k-\varepsilon$ model parameter
p	pressure
t	time
u_i	velocity i-component
u_x	velocity x-component
u_y	velocity y-component
u_z	velocity z-component
x_i	spatial i-coordinate
$\bar{c}_{\mathrm{Mg^{2+}}}$	magnesium ions concentration
$\bar{c}_{\mathrm{OH^-}}$	hydroxyl ions concentration

ΔG Gibbs free energy

a solution activity

A_1 maximum value of homogeneous nucleation rate

A_2 maximum value of heterogeneous nucleation rate

B_1 exponential factor of the homogeneous nucleation rate

B_2 exponential factor of heterogeneous nucleation rate

k_{sp} solubility product thermodynamic constant

L_{c} critical size

n_{i} number of moles of the i^{th} ion

T Temperature

Greek Symbols

ν kinematic viscosity

ν_t turbulent kinematic viscosity

ρ fluid density

σ_ε $k-\varepsilon$ model parameter, ε equation

ε turbulent kinetic energy dissipation rate

k turbulent kinetic energy

$\Delta\mu^{\mathrm{cp}}$ chemical potential variation

γ_{sl} interfacial tension between the solid and liquid phase

$\gamma_{\pm}$ solution activity coefficient

$\mu_{\mathrm{p}}^{\mathrm{cp}}$ chemical potential of the molecule in the solid particle bulk

$\mu_{\mathrm{s,i}}^{\mathrm{cp}}$ chemical potential of the i^{th} ion

$\mu_{\mathrm{s}}^{\mathrm{cp}}$ chemical potential of the molecule in the solution

σ_k $k-\varepsilon$ model parameter, k equation

k_B Boltzmann constant

P_ε turbulent kinetic energy generation rate

Superscripts

cp chemical potential

Subscripts

eq equilibrium

p particle

s solution

Other Symbols

∂ partial derivative

Acronyms / Abbreviations

CFD Computation Fluid Dynamics

CNT Classical Nucleation Theory

CRMs Critical Raw Materials

LES Large Eddies Simulations

MCM Multi-Class Methods

MSMPR Mixed Suspension Mixed Product Removal

NN Neural Network

PBE Population Balance Equation

PBM Population Balance Model

PDF Probability Density Function

PSD Particle Size Distribution

QMOM Quadrature Method Of Moments

RANS Reynolds Averaged Navier Stokes

WRM Weighted Residual Methods

Chapter 1

Introduction

1.1 Importance and Applications of Critical Raw Materials

Raw materials form the backbone of economies, serving as the fundamental building blocks for industrial production and innovation. However, reliable and uninterrupted access to certain raw materials has emerged as a growing concern both within the European Union (EU) and worldwide. In response to this challenge, the European Commission has developed a list of critical raw materials (CRMs) specific to the EU, which undergoes regular review and updates [1, 2]. These CRMs encompass raw materials of utmost importance to the EU economy, while also carrying risks associated with their supply chains. CRMs hold significant importance in various aspects of our society, contributing to industry, technological advancements, and environmental sustainability [3–5]. For instance, raw materials enable the miniaturization, durability, and efficiency that we expect from our electronic devices, making them indispensable to modern technology. Raw materials also play a crucial role in promoting environmental sustainability through the development of clean technologies [6]. They are irreplaceable components in solar panels, wind turbines, electric vehicles, and energy-efficient lighting systems. By harnessing renewable energy sources and reducing greenhouse gas emissions, these clean technologies help mitigate the environmental impact of traditional energy production methods. Special attention is dedicated to the management of mineral resources, particularly in light of the European Green Deal's focus on achieving economic growth that is decoupled

from resource consumption. The ambitious goal of the European Green Deal, aimed at fostering sustainable development and environmental protection while ensuring economic prosperity, can be realized through the adoption of a circular economy (CE) approach [7–9]. In an era marked by growing environmental concerns and the need for sustainable development, mineral extraction processes have come under scrutiny for their significant impact on the environment and natural resources. This thesis aims to address these challenges and does so within the framework of the SEArcularMINE European Project. This project undertakes a transformative journey, focusing on the development of a sustainable circular approach to mineral extraction. SEArcularMINE project is centered around building upon the traditional saltworks process, wherein seawater undergoes natural evaporation and crystallization in shallow basins. This brine contains high concentrations of valuable trace elements. The primary goal of the project is to develop sustainable and cost-effective technologies that will play a critical role in securing European access to CRMs through a circular processing approach, utilizing abundant brine resources. The project focuses on several key areas:

- Development of three innovative technologies targeting the extraction of Magnesium (Mg), Lithium (Li), and other trace elements (Rb, Sr, Cs, Ga, Ge, Co) [10–14].
- Establishment of multiple auxiliary processes to ensure complete circularity during the production process.
- Utilization of salinity gradient power and on-site solar and wind energy to meet energy needs [15].
- Creation of advanced modelling tools to simulate, size, and evaluate processes, optimizing resource usage under various framework conditions.
- Characterization of brine availability across Europe and the entire Mediterranean basin.

This opens the way for further development, widespread adoption, and acceptance of the circular processing approach. SEArcularMINE aims to transform mineral extraction in the EU by creating innovative technologies that unlock new resources, support economic growth, and protect the environment. The project's circular approach, using only seawater as an input, reduces the need for external chemicals

and minimizes energy and freshwater usage, promoting sustainability. Additionally, SEArcularMINE explores integrating its technologies with seawater desalination, offering a cost-effective solution to address freshwater scarcity and support sustainable water management. The focus of this thesis is to exclusively analyze, characterize, and model the recovery of magnesium.

1.2 Research Objectives and Motivation

Motivated by the EU's emphasis on achieving circular economy principles and resource independence, this research has been driven by the vision to extract magnesium efficiently and sustainably from highly concentrated solutions, specifically brines. Magnesium concentrations in seawater typically range from 1.1 to 1.7 g/L, while in brines, it can reach levels as high as 60 g/L. Recent years have witnessed a sharp rise in the magnesium market, and further substantial growth is anticipated in the future. The strategic importance of magnesium is highlighted by its inclusion among the 30 CRMs for the EU. This recognition is primarily attributed to the geographical distribution of magnesium producers, mainly situated in the USA, China, and Russia [16]. Magnesium finds widespread application in the form of magnesium hydroxide ($Mg(OH)_2$) and magnesium oxide (MgO). Both $Mg(OH)_2$ and MgO belong to a group of compounds known for their numerous favorable properties and potential practical applications [17]. $Mg(OH)_2$, owing to its remarkable properties, serves as a versatile compound with a multitude of practical applications. It acts as a flame-retardant filler in composite materials, exhibiting endothermic dehydration at high temperatures. Additionally, $Mg(OH)_2$ functions as an effective acidic waste neutralizer and finds utility as a pharmaceutical excipient. In the pulp and paper industry, it serves as a preservative, while in the realm of fertilizers, it acts as an additive. Moreover, $Mg(OH)_2$ plays a crucial role as a component in ethanol chemical sensors. Notably, it serves as the most vital precursor for the preparation of MgO, a catalyst widely employed in various industrial processes [18]. Numerous methods have been employed to obtain $Mg(OH)_2$ nanostructures. These methods include microwave or ultrasonic/hydrothermal treatment [19, 20], precipitation [21–25], precipitation with the aid of additives [26], hydrothermal process [27] and an innovative ionic exchange membrane crystallizer [28, 29]. These diverse approaches offer exciting possibilities for tailoring $Mg(OH)_2$ crystalline structures to suit spe-

cific applications, enhancing its potential for various technological advancements. The extraction of magnesium from highly concentrated solutions presents a highly intricate task. Several research studies have explored innovative approaches to tackle this challenge effectively.

A widely used route in large-scale processes is the hydrothermal method. In this approach, a magnesium precursor, such as $Mg(NO_3)_2 \cdot 6H_2O$, reacts with an alkaline solution in a stirred reactor at room temperature. It is then transferred to an autoclave system for hydrothermal treatment at a constant temperature (150-180 °C), followed by cooling back to room temperature. The resulting mixture is separated using a centrifuge, washed with water to remove impurities, and then washed with ethanol to prevent agglomeration. Finally, the product is dried in an inert gas atmosphere. Additionally, the solvothermal method is worth mentioning briefly. It shares many similarities with the hydrothermal method but can serve as a replacement when a high-purity product is required. By employing solutions under critical conditions instead of aqueous solutions, the solvothermal method can yield a product with much higher purity [30]. However, both the hydrothermal and solvothermal methods are relatively expensive in terms of energy and equipment requirements. As a result, the precipitation process has been favored as a simpler and more cost-effective alternative.

Turek and Gnot [25] achieved success by effectively extracting $Mg(OH)_2$ through a precipitation process from hard coal mine brine containing 2.84 g/L of magnesium. Similarly, Cipollina et al. [21] demonstrated their prowess in producing high-purity $Mg(OH)_2$ using real brines. Meanwhile, Yousefi et al. [24] utilized a surfactant, poly(ethylene glycol, PEG 4000), to synthesize $Mg(OH)_2$, employing a chemical precipitation method on an impure brine. These diverse investigations showcase the intricate nature of magnesium recovery from concentrated solutions and the ingenuity required to overcome this scientific challenge. The precipitation mechanism of $Mg(OH)_2$ involves a complex interplay of various phenomena, spanning different scales, including the molecular-level (micro-scale) and geometry-level (macro-scale) aspects. This complexity arises from chemical reactions, homogeneous and heterogeneous nucleation, molecular growth, aggregation, and agglomeration. When the precipitation kinetics are remarkably fast, as observed in the production of $Mg(OH)_2$ from concentrated solutions, the role of mixing becomes crucial in determining the final particle size distribution (PSD). Numerous investigations have been conducted to explore and characterize the precipitation kinetics of $Mg(OH)_2$ [31–35].

Researchers have employed various experimental setups, including T-shaped static mixers and stirred reactors. These studies have revealed that the induction time, representing the duration between the formation of supersaturated solutions and the appearance of precipitates, is extremely short, often on the order of a few seconds, even at low magnesium concentrations, such as ~ 0.03 g/L. Such rapid precipitation highlights the intricacy of the process and underscores the significance of comprehending and optimizing the mixing conditions to achieve desired particle attributes during the production of $Mg(OH)_2$. Only a restricted number of investigations have addressed the impact of mixing on the precipitation processes of $Mg(OH)_2$ from concentrated solutions. For instance, Shirure et al. [36] examined the precipitation of $Mg(OH)_2$ from $MgCl_2$ solutions (up to 24 g/L) using T and Y-shaped static mixers. The researchers observed that higher reactant flow rates resulted in the production of smaller $Mg(OH)_2$ particles. To measure the PSDs, they introduced the surfactant Tween 20 to the $Mg(OH)_2$ suspensions, and the volume-average particle size was found to range from 5 μm to 30 μm. Similarly, Song et al. [37] successfully synthesized pure $Mg(OH)_2$ particles by employing $MgCl_2$ solutions (~ 40 g/L) with NaCl as an assistant additive in a glass reactor under vigorous stirring. The PSDs were measured using static light scattering (SLS) granulometry analysis without the use of surfactants, and particles in the micrometer range were reported. Moreover, SEM images revealed significant aggregates/agglomerates. Furthermore, Tai et al. [38] researched the precipitation of $Mg(OH)_2$ nanoparticles from highly concentrated $MgCl_2$ solutions (up to 20 g/L) utilizing a spinning disk reactor. The spinning disk reactor enabled an excellent degree of mixing, with a mixing time below 1 ms, which facilitated the synthesis of lamellar $Mg(OH)_2$ particles. These particles exhibited a length ranging from 50 to 80 nm and a thickness of approximately 10 nm. To aid in dispersion, the authors utilized a sonicator along with poly(acrylic acid, sodium salt) (PAA) and sodium hexametaphosphate as dispersants. Particle measurements were performed using dynamic light scattering (DLS) technology, yielding a number-average particle size ranging from 40.0 to 47.5 nm. Shen et al. [39] introduced a novel impinging stream-rotating packed bed reactor. To assess the particle size and distribution, the prepared samples were dispersed in distilled water through sonication for 10 minutes, utilizing a 2% sodium hexametaphosphate solution as a dispersant. Wide size distributions were observed at low liquid flow rates and rotating packed bed speeds. Furthermore, the PSDs became narrower as both the liquid flow rates and the rotating packed bed speeds increased. Beyond

spinning disk reactors, some other high-mixing efficiency devices can be utilized in the context of precipitation processes. For instance, T- or Y-shaped static mixers are chosen for their ability to feed reactants from opposite sides, causing them to collide and react within the mixing channel. Schikarski et al. [40] investigated such systems and found considerably high mixing efficiencies due to the extremely high turbulence generated. Similarly, Orlewski and Mazzotti [41] utilized a Y-mixer reactor to investigate the precipitation process of barium sulfate, conducting both experimental and computational studies. However, the literature review of $Mg(OH)_2$ precipitation has mainly focused on batch or semi-batch experimental tests. For instance, Alamdari et al. [23] investigated $Mg(OH)_2$ precipitation in both configurations to study the process and derive kinetics parameters. They performed preliminary experimental tests to identify operative conditions where primary nucleation could be neglected. The batch experiments led to rapid supersaturation and the formation of numerous fine particles due to primary nucleation. On the other hand, the semi-batch configuration resulted in a coarser product size due to the gradual addition of alkaline reactant to the magnesium precursor solution. As a result, the semi-batch approach was adopted, considering only secondary nucleation, growth rates, and aggregation, while neglecting the micro-mixing effect. Additionally, Yuan et al. [33] investigated primary nucleation and growth rates within a batch system with low concentrations using the electrical conductivity method, which is related to ion concentrations. This measurement allowed the determination of the induction time of nucleation, enabling the inference of certain kinetics parameters. Indeed, the identification of precipitation kinetics is of utmost importance in controlling the shape and size distribution of crystals during the precipitation process. Understanding the underlying kinetics allows for precise manipulation of various parameters, such as reaction conditions, which directly influence the final product's characteristics. By gaining insights into kinetics, the process can be optimized to achieve desired particles' properties, leading to better performance and applicability in various industrial applications. This thesis aims to achieve two main objectives: (i) identify the precipitation kinetics set of magnesium hydroxide that is independent of a specific system and operating conditions, and (ii) develop a robust framework for modelling and predicting particle outcomes. Despite extensive efforts in characterizing the precipitation of magnesium hydroxide, existing literature lacks a comprehensive model capable of describing its precipitation under varying conditions.

1.3 A Roadmap to Chapters 2-8

This doctoral thesis delves into a comprehensive exploration of various phenomena and processes relevant to reactive crystallization systems, focusing on computational modelling, mixing dynamics, precipitation kinetics, and 3D modelling techniques. The thesis is organized into several chapters, each contributing uniquely to our understanding of the subject matter.

Chapter 2: Computational Fluid Dynamics (CFD) Modeling This chapter introduces the fundamental aspects of modelling critical phenomena such as turbulent mixing, fast irreversible reactions, nucleation, growth, and aggregation using Computational Fluid Dynamics (CFD) techniques. The chapter aims to establish a theoretical foundation for understanding the complex dynamics governing reactive crystallization systems.

Chapter 3: Mixing Dynamics and Precipitation Processes The third chapter centers on the pivotal role of mixing in influencing the outcomes of precipitation processes within fluid systems. Static mixers, particularly T-shaped mixers, are extensively explored through numerical simulations and experimental investigations. This chapter lays the groundwork for understanding how mixing parameters affect the kinetics of reactive crystallization. In this chapter, the candidate has entirely taken care of the modelling side.

Chapter 4: Experimental Study on Precipitation Dynamics In this experimental chapter, a comprehensive study is presented on the precipitation of magnesium hydroxide ($Mg(OH)_2$) from highly concentrated synthetic $MgCl_2$ solutions. Circular cross-sectional T-shaped mixers are employed to control reactant homogenization, providing insights into particle size distribution and aggregation/agglomeration dynamics. In this chapter, the candidate collaborated in the experimental campaign, conducting replicates of some tests and measuring the zeta potential.

Chapter 5: Kinetic Parameters Inference and Modeling The fifth chapter aims to develop a comprehensive model for inferring kinetic parameters related to primary nucleation, molecular growth, and aggregate strength in reactive crystallization

systems. Through a combination of theoretical modelling and experimental data, this chapter contributes to enhancing our understanding of precipitation kinetics. In this chapter, the candidate has done all the work

Chapter 6: Machine Learning Optimization Approach In this innovative chapter, a machine-learning-based optimization approach is introduced for optimizing precipitation kinetics parameters. The integration of artificial intelligence with experimental data and mechanistic models provides a robust framework for optimizing complex engineering processes. In this chapter, the candidate has done all the work

Chapter 7: 3D Modeling for Precipitation System Design The final chapter leverages 3D modelling techniques to calibrate and validate a precipitation model for magnesium hydroxide synthesis. The calibrated model serves as a powerful tool for designing and optimizing prototype precipitation systems, showcasing the practical applications of the research findings. In this chapter, the candidate has done all the work

Chapter 8: Comprehensive Overview and Practical Applications Chapter 8 represents a culmination and synthesis of the research efforts undertaken throughout this doctoral thesis, bridging theoretical insights with tangible applications in magnesium recovery from brines and bitterns, with a specific emphasis on critical raw materials (CRMs) and circular economy principles.

Chapter 2

Fundamentals and Theoretical Background

The focus of this chapter is the description of the modelling of the main phenomena involved: Computational Fluid Dynamics (CFD), turbulent mixing, fast irreversible reaction, nucleation, growth, and aggregation.

2.1 Modelling of Turbulent Mixing

In the field of fluid mechanics, the study involves categorizing flows into distinct types: laminar and turbulent flow. This classification relies on the characteristics observed in streamlines and velocity levels. Turbulence characterizes the unpredictable motion that envelops fluid as it swiftly traverses a surface or navigates through confined spaces. The distinctive nature of turbulence is shaped by its intricate, multi-layered structure, unfolding as a cascade of swirling eddies or vortices. These intriguing eddies organize themselves in a hierarchical structure, encompassing a range of scales that extend from substantial dimensions down to incredibly small sizes, measuring a few micrometers. The exploration of turbulence drives the development of mathematical frameworks and empirical approaches, all aimed at comprehending the intricate dynamics. The mathematical framework finds expression through diverse methodologies, encompassing approaches such as Direct Numerical Simulation (DNS), Large Eddy Simulation (LES), and the modelling techniques embodied by Reynolds-Averaged Navier-Stokes (RANS). These models

solve and model the scales involved differently (Figure 2.1) and, as a result, have different computational costs:

- **DNS:** Complete Resolving of Flow (No Modeling)
  DNS models simulate the entire range of turbulent scales without modelling, offering unparalleled accuracy but requiring significant computational resources.
- **LES:** Partial Modeling of Flow
  LES models simulate larger turbulent structures directly while modelling smaller scales. This strikes a balance between accuracy and computational efficiency.
- **RANS:** Complete Modelling of Flow
  RANS models are based on time-averaged equations and treat turbulent fluctuations as a separate term. This approach provides a comprehensive representation of turbulence.

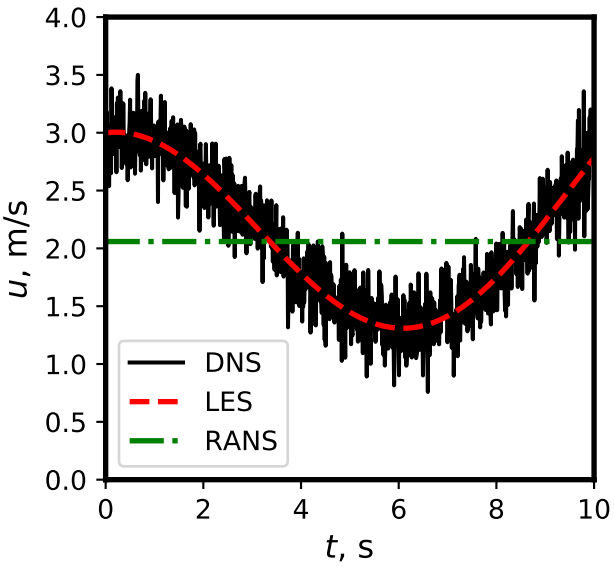

Figure 2.1 Comparison of three turbulence models: (i) DNS (solid black line), (ii) LES (dashed red line) and RANS (dot-dashed green line)

In the current pursuit, the attention is directed toward the utilization of RANS models. RANS equations describe the time-averaged behaviour of fluid flow and account for the effects of turbulence. RANS equations for Newtonian, single-phase, incompressible flow are as follows:

Continuity Equation:

$$\frac{\partial \bar{u}_i}{\partial x_i} = 0 \tag{2.1}$$

The continuity equation ensures that the rate of change of mass within a region is balanced by the net flow of mass across its boundaries. Here, $\mathbf{u} = (u_x, u_y, u_z)$ represents the velocity vector.

Momentum Equations (Navier-Stokes Equations):

$$\frac{\partial \bar{u}_i}{\partial t} + \bar{u}_j \frac{\partial \bar{u}_i}{\partial x_j} = \frac{\partial}{\partial x_j}\left(\nu\left(\frac{\partial \bar{u}_i}{\partial x_j} + \frac{\partial \bar{u}_j}{\partial x_i}\right) - \overline{u_i' u_j'}\right) - \frac{1}{\rho}\frac{\partial \bar{p}}{\partial x_i} + \mathrm{g}_i \tag{2.2}$$

These equations govern the momentum conservation for each coordinate direction i (where i can be x, y, or z). They describe how the velocity changes due to pressure gradients, viscous forces, and Reynolds stresses. Here, p is pressure, ρ is density, $\mathbf{g}$ is the gravitational acceleration, μ is dynamic viscosity, and $\overline{u_i' u_j'}$ represents the Reynolds stress tensor, which characterizes turbulent fluctuations and it can be closed as follows:

$$\overline{u_i' u_j'} = \nu_t\left(\frac{\partial \bar{u}_i}{\partial x_j} + \frac{\partial \bar{u}_j}{\partial x_i}\right) \tag{2.3}$$

Here, ν_t is the turbulent viscosity. The RANS equations are based on the concept of Reynolds averaging, which separates the flow variables into mean and fluctuating components. Turbulence models provide additional closure by relating the Reynolds stresses to flow properties, enabling the prediction of turbulent behavior in various engineering simulations.

$k-\varepsilon$ model

The $k-\varepsilon$ model is one of the simplest turbulence models. It predicts the turbulent kinetic energy (k) and the rate of dissipation of k (ε) through transport equations.
Turbulent kinetic energy equation:

$$\frac{\partial k}{\partial t} + \frac{\partial (\bar{u}_i k)}{\partial x_i} = \frac{\partial}{\partial x_i}\left((\nu + \sigma_k \nu_t)\frac{\partial k}{\partial x_i}\right) + P_\varepsilon - \varepsilon \tag{2.4}$$

Turbulent kinetic energy dissipation rate equation:

$$\frac{\partial \varepsilon}{\partial t} + \frac{\partial (\bar{u}_i \varepsilon)}{\partial x_i} = \frac{\partial}{\partial x_i}\left((\nu + \sigma_\varepsilon \nu_t)\frac{\partial \varepsilon}{\partial x_i}\right) + C_{\varepsilon 1}\frac{\varepsilon}{k}P_\varepsilon - C_{\varepsilon 2}\frac{\varepsilon^2}{k} \tag{2.5}$$

$$\nu_t = C_\mu \frac{k^2}{\varepsilon} \tag{2.6}$$

Here, P_ε represents turbulent production, ν_t is the turbulent viscosity from Launder and Spalding [42] and σ_k, σ_ε, $C_{\varepsilon 1}$, $C_{\varepsilon 2}$ and C_μ are model parameters and their value is reported in Table 2.1 [43].

Table 2.1 $k-\varepsilon$ model parameters

Parameter	σ_k	σ_ε	$C_{\varepsilon 1}$	$C_{\varepsilon 2}$	C_μ
Typical Value	1.0	1.3	1.44	1.92	0.09

$k-\omega$ SST model

The $k-\omega$ SST model employs two transport equations: one for turbulent kinetic energy (k) and another for the specific dissipation rate of turbulence (ω) [44, 45].

Turbulent kinetic energy equation:

$$\frac{\partial k}{\partial t} + \frac{\partial (\bar{u}_i k)}{\partial x_i} = \frac{\partial}{\partial x_i}\left((\nu + \sigma_k \nu_t)\frac{\partial k}{\partial x_i}\right) + P_\omega - \beta^* \omega k \tag{2.7}$$

Specific dissipation rate equation:

$$\frac{\partial \omega}{\partial t} + \frac{\partial (\bar{u}_i \omega)}{\partial x_i} = \frac{\partial}{\partial x_i}\left((\nu + \sigma_\omega \nu_t)\frac{\partial \omega}{\partial x_i}\right) + \frac{\gamma}{\rho \nu_t}P_\omega - \beta \omega^2 \tag{2.8}$$
$$+ 2(1-F_1)\frac{\sigma_{\omega 2}}{\omega}\frac{\partial k}{\partial x_i}\frac{\partial \omega}{\partial x_i}$$

$$\nu_t = \frac{a_1 k}{\max(a_1 \omega, b_1 F_{23} S)} \tag{2.9}$$

Here, P_ω represents turbulent production, F_1 is a blending function and σ_k, σ_ω, γ, β, $\sigma_{\omega 2}$, a_1 and b_1 are model parameters and the procedure to compute their value is reported in Menter [46] Appendix.

RNG $k-\varepsilon$ model

The RNG $k-\varepsilon$ model employs transport equations for turbulent kinetic energy (k) and the rate of dissipation of turbulence (ε). The turbulent kinetic energy equation for RNG $k-\varepsilon$ is equal to standard $k-\varepsilon$ (see Eq. (2.4)). Dissipation rate equation:

$$\frac{\partial \varepsilon}{\partial t}+\frac{\partial(\rho \bar{u}_i \varepsilon)}{\partial x_i}=\frac{\partial}{\partial x_i}\left((\nu+\sigma_\varepsilon \nu_t)\frac{\partial \varepsilon}{\partial x_i}\right)+C_\varepsilon \frac{\varepsilon}{k}P_\varepsilon - C^*_{\varepsilon 2}\frac{\varepsilon^2}{k} \tag{2.10}$$

Here, P_ε represents turbulent production, ν_t is equal to Eq. (2.6) and σ_k, σ_ε, $C_{\varepsilon 1}$, $C^*_{\varepsilon 2}$ and C_μ are model parameters and their value can be calculated following Yakhot et al. [47]. The difference between the standard $k-\varepsilon$ model and the RNG $k-\varepsilon$ model lies in the calculation of some of the parameters, including $C^*_{\varepsilon 2}$. While small, this difference demonstrates the impact that parameters have on the quality of turbulence description.

2.2 Reactive Turbulent Flows

Turbulent reacting flows are complex fluid dynamics phenomena that involve the interaction between turbulence and chemical reactions [48]. This intricate coupling of fluid motion and chemical processes occurs in a wide range of natural and engineered systems, such as atmospheric chemistry [49], and industrial combustion processes [50]. Turbulence itself refers to the irregular and chaotic motion of a fluid, characterized by the presence of eddies and vortices at different scales. These turbulent eddies enhance the mixing of different fluid components, leading to an efficient exchange of heat, mass, and momentum. In the context of reactive flows, this enhanced mixing is crucial as it enables the reactants to come into close proximity, promoting chemical reactions and influencing the overall kinetics [51–53].

The behaviour of turbulent reacting flows is determined by several key factors. First, the initial conditions, such as the temperature, pressure, and concentrations of the reactants, significantly influence the reaction pathways and their rates. Second, the specific characteristics of the turbulent flow, including turbulence intensity, length scales, and Reynolds number, dictate the level of mixing and thus affect the reaction rates. The coupling between turbulence and chemistry is often described using two main approaches: the Reynolds-Averaged Navier-Stokes equations and Large

Eddy Simulation [54–58]. RANS equations average the turbulent flow properties over time, providing a computationally efficient method, but they might miss some important small-scale turbulent structures that are crucial for accurate predictions of the reaction rates [59]. On the other hand, LES directly simulates the large-scale turbulent structures while modelling the smaller ones, offering a more detailed representation of the flow, but at a higher computational cost.

Researchers in the field of turbulent reacting flows face numerous challenges. The non-linear nature of turbulence and the complex interactions between chemical reactions and fluid dynamics necessitate sophisticated mathematical and numerical methods. Additionally, the wide range of length and time scales involved requires resolving a significant span of scales, which can be computationally demanding [40, 60].

Governing Equations

Modelling chemical reactions in the turbulent regime begins with solving the continuity (Eq. (2.1)), the flow field (Eqs. (2.2)) and turbulence (e.g., Eqs. (2.4), (2.5) and (2.6)). Since the fluid comprises a blend of C interactive chemical species, it becomes essential to establish the measure of each species's concentration, denoted as $\bar{c}_i$. In this context, the index $\alpha = 1, 2, 3, \ldots, C$ is used to distinguish between various constituents. In light of chemical dynamics, the concentrations of individual constituents within the fluid vary in space and time, as governed by the ensuing scalar transport equation:

$$\frac{\partial \bar{c_\alpha}}{\partial t} + \bar{u_j}\frac{\partial \bar{c_\alpha}}{\partial x_j} = \frac{\partial}{\partial x_j}\left(D_\alpha \frac{\partial \bar{c_\alpha}}{\partial x_j}\right) + R_\alpha(\mathbf{c}) \tag{2.11}$$

Here D_α is the diffusion coefficient of the i^{th} component in the fluid phase and $R_i(c)$ represents the sink term. It is possible to make the Eqs. (2.2) and (2.11) dimensionless to obtain dimensionless groups based on the molecular properties of fluids that allow *a-priori* understanding of what the controlling resistance of the process is [61]. Therefore, it is necessary to identify a characteristic length, L, of the system, and a characteristic velocity, U. The dimensionless groups are:

- *Reynold number*, $Re = LU/\nu$ is defined as the ratio of the inertial and viscous forces

- *Schmidt number*, $S\bar{c}_i = \nu/D_i$ is defined as the ratio of the momentum transport rate to the molecular diffusion rate
- *Damkhöler number*, $Da = \tau_f/\tau_r$ is defined as the ratio of the time scale of fluid flow to the reaction time

It is worth mentioning that each of these groups was obtained from the molecular transport properties of the fluid and accounts for the system studied (e.g., the *Re* changes when the system changes) and consequently are dimensionless system-dependent groups. Conversely, one can define the same dimensionless groups based on the turbulent properties of the system (e.g. k and ε) by making these turbulent dimensionless groups independent of the system and dependent only on the momentum conditions.

Premixed and Non-Premixed Reactive Flow Configurations

When studying reacting flows, it is important to differentiate between premixed and non-premixed configurations, as they exhibit distinct reactive characteristics. In premixed flows, the reacting species are intimately mixed before entering the combustion zone. This creates a uniform mixture with a defined reacting species ratio. The reaction occurs uniformly throughout the mixture. An example of a premixed configuration is found in combustion processes [62, 63] In contrast, non-premixed flows involve the separate injection of reacting species into the reaction zone [64, 65]. This leads to a region where the reacting species exist in distinct spatial domains. Non-premixed reacting species often exhibit complex structures and are more sensitive to changes in the flow conditions. Examples of non-premixed flows are (i) fast reaction in diffusion flames [66] or (ii) acid-base reaction in a liquid [67].

Slow, Finite-rate and Fast Chemical Reactions

In the world of chemical reactions, there's a spectrum that shows how fast these reactions happen compared to the flow of fluids. This spectrum has two ends that

help us understand how reacting systems work. The Damkhöler number is the key player in defining this spectrum. A schematic representation is provided in Figure 2.2:

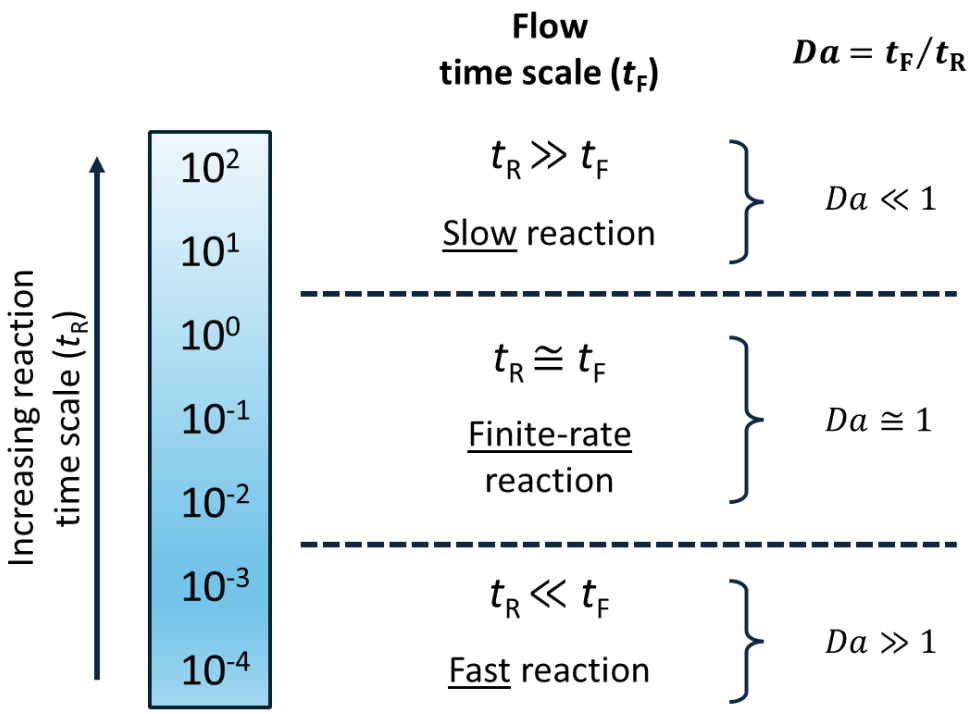

Figure 2.2 Schematic representation of the reaction time scale (t_R) compared with the flow time scale (t_F) and the corresponding Damkhöler number

On one side of the spectrum, when the Damkhöler number is way less than one, it tells us that fluids are flowing much faster than chemical reactions are taking place. This means that chemical reactions are happening slowly compared to the quick mixing in the system. We call this 'slow' chemical reactions. But if the Damkhöler number is way bigger than one, it means that chemical reactions are happening quickly compared to the flow of fluids. This is what we mean by 'fast' chemical reactions. When the Damkhöler number is around one, it's a balance point between chemical reactions and fluid flow. This is called 'finite-rate' chemical reactions. In this situation, the timescales for both processes are comparable. This study primarily revolves around non-premixed turbulent reacting flows, with a special emphasis on swift chemical reactions occurring within a liquid phase.

Computational Modelling of fast, irreversible reactions

The multi-scale nature of turbulence presents a significant challenge in its modelling, particularly when chemical reactions are involved. In such situations, the chemical reaction itself cannot occur unless the reactants are thoroughly mixed both at the largest scales (macro-mixing) and at the smallest scales, (micro-mixing). Addressing this complex interaction between mixing and reactions has been a subject of research for many years, leading to the development of various approaches to account for their interference. Several studies have proposed different methodologies to model the interplay between mixing and reactions. Notable examples include the works by Pohorecki and Baldyga [68] and Fox [69]. These approaches aimed to capture the intricate dynamics of turbulence-chemistry interaction, where mixing plays a crucial role in determining the reaction rates and species distributions. In this thesis, we adopt the approach utilized by Baldyga et al. [70] and elaborated upon by Marchisio and Fox [53] specifically for fast irreversible reactions. This approach aims to address the challenges posed by fast, irreversible reactions occurring in turbulent flows. The rapid nature of such reactions necessitates a detailed understanding of mixing effects, as they directly impact the reaction kinetics and overall reaction behaviour. By incorporating the mixing effects into the modelling approach, researchers can gain valuable insights into the interaction between turbulent mixing and chemical reactions.

In reactive turbulent flow modelling, it is crucial to properly tune the governing equations to decouple macro-mixing and micro-mixing processes. Macro-mixing is described through the mixture fraction equation, while the variance of the mixture fraction represents micro-mixing. The mixture fraction equation can be written as follows:

$$\frac{\partial \bar{\alpha}}{\partial t} + \bar{u_j}\frac{\partial \bar{\alpha}}{\partial x_j} = \frac{\partial}{\partial x_j}\left(D_t \frac{\partial \bar{\alpha}}{\partial x_j}\right) \tag{2.12}$$

where $\bar{\alpha}$ is the Reynolds-averaged mixture fraction and D_t is the turbulent diffusion coefficient defined as:

$$D_t = \frac{\nu_t}{Sc_t} \tag{2.13}$$

Here Sc_t is the turbulent Schmidt number. The diffusive term in Eq. (2.12) is responsible for gradient flattening, which depends on the turbulence conditions and can be tuned by changing parameters like Sc_t or C_μ. In high turbulent conditions, a smaller Sc_t leads to reduced gradients, indicating more effective turbulent mixing.

The mixture fraction, $\bar{\alpha}$, is physically linked to the relative amount of two fluids in a known control volume. Specifically, $\bar{\alpha}$ will be 0 (1) when only A solution (B) is present and 0.5 when both A and B solutions are equally present. The variance of the mixture fraction, $\overline{\alpha'^2}$, is described by the following equation:

$$\frac{\partial \overline{\alpha'^2}}{\partial t} + \bar{u_j}\frac{\partial \overline{\alpha'^2}}{\partial x_j} = \frac{\partial}{\partial x_j}\left(D_t \frac{\partial \overline{\alpha'^2}}{\partial x_j}\right) + \underbrace{2D_t\left(\frac{\partial \bar{\alpha}}{\partial x_j}\cdot\frac{\partial \bar{\alpha}}{\partial x_j}\right)}_{\text{Production}} - \underbrace{\varepsilon_{\overline{\alpha'^2}}}_{\text{Dissipation}} \tag{2.14}$$

Besides the terms previously explained, the second and third terms on the right-hand side of Eq. (2.14) represent, respectively, the production and dissipation of the variance. Notably, the production term occurs at a larger scale, involving the mixture fraction, while the dissipation term takes place at a smaller scale, reflecting the Batchelor micro-scale. This observation emphasises the multi-scale nature of mixing phenomena. Unlike the mixture fraction equation, the variance equation is not fully mathematically closed. The dissipation term in the variance equation requires a closure expression to account for the variance dissipation rate, denoted as γ. Marchisio et al. [71] proposed the following equation to calculate γ:

$$\gamma = C_f \frac{C_\phi}{2}\frac{\varepsilon}{k} \tag{2.15}$$

$$\varepsilon_{\overline{\alpha'^2}} = \gamma \overline{\alpha'^2} \tag{2.16}$$

Here, k/ε represents the micro-mixing characteristic time. C_f and C_ϕ are model parameters. The parameter C_f can be easily tuned with known experimental data to accurately describe the variance dissipation rate [72]. Regarding C_ϕ, two approaches can be adopted. For high-Reynolds flows, it can be assumed constant and equal to 2 [53]. Alternatively, it can be calculated based on the local turbulence characteristics. Liu and Fox [73] provided a correlation for C_ϕ as a function of k and ε:

$$C_\phi = \sum_{n=1}^{6} a_n \left(\log_{10} Re_l\right)^n \tag{2.17}$$

Here, a_n are fitting parameters reported in Liu and Fox [73] and Re_l is the local Reynolds number, $Re_l = k/\sqrt{\varepsilon\nu}$, which depends on the turbulent properties and the fluid kinematic viscosity, ν.

Probability Density Function

A well-established approach to describing chemical reactions in turbulent flows is to use the presumed Probability density function (PDF). The PDF represents the probability of finding the monitored property of interest in an infinitesimal spatial interval [74, 75]. One can, therefore, use the PDF $f(\alpha)$ to derive the mixing fraction and its variance, as follows:

$$\int_0^1 f(\alpha)d\alpha = 1 \tag{2.18}$$

$$\int_0^1 f(\alpha)\alpha d\alpha = \bar{\alpha} \tag{2.19}$$

$$\int_0^1 f(\alpha)(\alpha-\bar{\alpha})^2 d\alpha = \overline{\alpha'^2} \tag{2.20}$$

The benefit of this approach is that one can use an *a priori* chosen functional form for the PDF and reconstruct it using only low-order moments (i.e., the mixing fraction and its variance). In this way, it is not necessary to solve a transport equation of the PDF. Several types of PDF have been studied, however, in this paper the focus is on the f_β PDF (i.e., β probability density function):

$$f_\beta(\alpha) = \frac{\alpha^{n-1}(1-\alpha)^{m-1}}{\int_0^1 \alpha^{n-1}(1-\alpha)^{m-1}d\alpha} \tag{2.21}$$

Here, $n = \bar{\alpha}\left(\frac{1}{I_s}-1\right)$ and $m = (1-\bar{\alpha})\left(\frac{1}{I_s}-1\right)$ and $I_\mathrm{s} = \frac{\overline{\alpha'^2}}{\bar{\alpha}(1-\bar{\alpha})}$

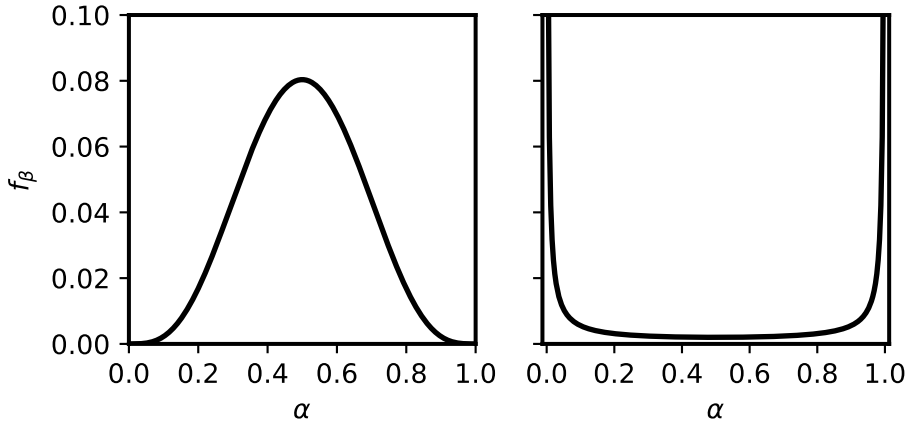

Figure 2.3 $f_\beta(\alpha)$ for two values of I_s and a constant value of $\bar{\alpha} = 0.5$. $I_\mathrm{s} = 0.1$ on the left and $I_\mathrm{s} = 1$ on the right

Figure 2.3 shows the shape that the f_β PDF assumes in the two boundary cases ($\bar{\alpha} = 0.5$, $I_s = 0.1$ (*left*) and (ii) $I_s = 1$ (*right*)). When the I_s is low (0.1 in Figure 2.3-*left*), f_β assumes higher values at mixing fractions equal to the imposed $\bar{\alpha}$ value (0.5 in this case). In other words, the probability of finding regions in the reaction domain where the two fluids are mixed is higher. Conversely, when the I_s is high (1 in Figure 2.3-*right*) the probability of finding regions in the reaction domain where only the two pure liquids exist (corresponding to α = 0 and 1) is higher.

Instantaneous, irreversible reactions

In the case of instantaneous and irreversible reactions, algebraic relationships can be obtained that link the concentration $\phi_i(\alpha)$ of the i^{th} chemical species involved to the local mixture fraction. In the case of reactions in which only two reactants are involved, for example, an acid A and a base B forming a product P ($A + rB \rightarrow P$), the equations become:

$$\frac{\phi_A(\alpha)}{\phi_A^{(0)}} = 1 - \frac{\alpha}{\alpha_s}, \qquad \frac{\phi_B(\alpha)}{\phi_B^{(0)}} = 0, \qquad \text{if } \alpha \in [0, \alpha_s] \tag{2.22}$$

$$\frac{\phi_A(\alpha)}{\phi_A^{(0)}} = 0, \qquad \frac{\phi_B(\alpha)}{\phi_B^{(0)}} = \frac{\alpha - \alpha_s}{1 - \alpha_s}, \qquad \text{if } \alpha \in [\alpha_s, 1] \tag{2.23}$$

where α_s is the stoichiometric mixture fraction defined as follows:

$$\alpha_s = \frac{r\phi_A^{(0)}}{r\phi_A^{(0)} + \phi_B^{(0)}} \tag{2.24}$$

Here $\phi_A^{(0)}$ and $\phi_B^{(0)}$ represent the reactant concentrations fed to the reaction volume. Eqs. (2.22), (2.23) and (2.24) are derived assuming that a mixture fraction of 0 corresponds to pure A and a mixture fraction of 1 corresponds to pure B. Similarly, algebraic equations can be derived for the P product:

$$\frac{\phi_P}{\phi_B^{(0)}} = \frac{\alpha}{\alpha_s r}, \qquad \text{if } \alpha \in [0, \alpha_s] \tag{2.25}$$

$$\frac{\phi_P}{\phi_B^{(0)}} = \frac{1}{r}\left(\frac{1 - \alpha}{1 - \alpha_s}\right), \qquad \text{if } \alpha \in [\alpha_s, 1] \tag{2.26}$$

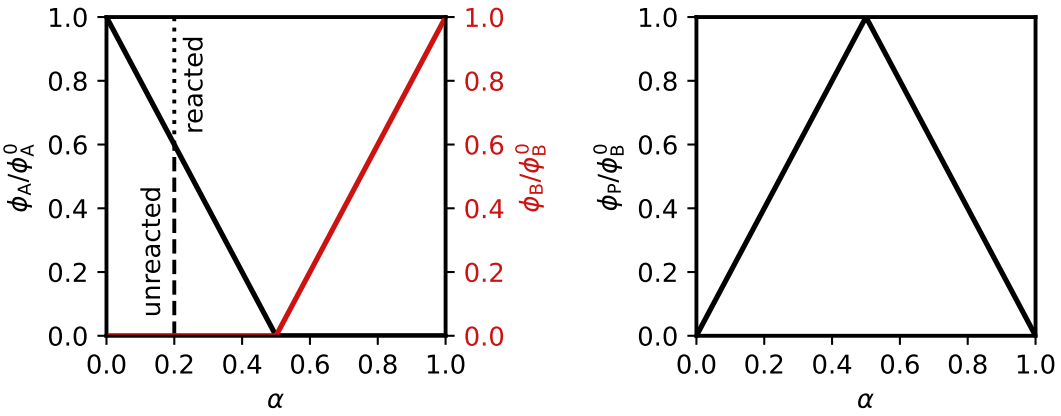

Figure 2.4 A, B and P dimensionless concentrations when $I_s = 0$. A and B reactants on the left and P product on the right

For simplicity, let's consider the case where $r = 1$ and $\alpha_s = 0.5$ to plot A, B and P dimensionless concentrations. Figure 2.4-*left* shows the dimensionless concentration in terms of reactants while Figure 2.4-*right* shows the product concentration. These profiles refer to an $I_s = 0$. It means that the reactants are perfectly micro-mixed. In this case, since the reaction is instantaneous and irreversible, the two reactants cannot coexist and, depending on the α value, a certain amount of A (B) will react to form P while any excess will remain unreacted. When, however, the mixing conditions do not correspond to perfect micro-mixing one has to weigh the concentration that can react at the micro-scale with the f_β. Therefore, assuming a functional form for the PDF, concentrations can be calculated for any value of $\bar{\alpha}$ and $\overline{\alpha'^2}$ (i.e., for any mixing condition) as follows:

$$\bar{\phi}_A = \int_0^1 \left(\phi_A f_\beta\right)(\alpha) \mathrm{d}\alpha \tag{2.27}$$

$$\bar{\phi}_B = \int_0^1 \left(\phi_B f_\beta\right)(\alpha) \mathrm{d}\alpha \tag{2.28}$$

$$\bar{\phi}_P = \int_0^1 \left(\phi_P f_\beta\right)(\alpha) \mathrm{d}\alpha \tag{2.29}$$

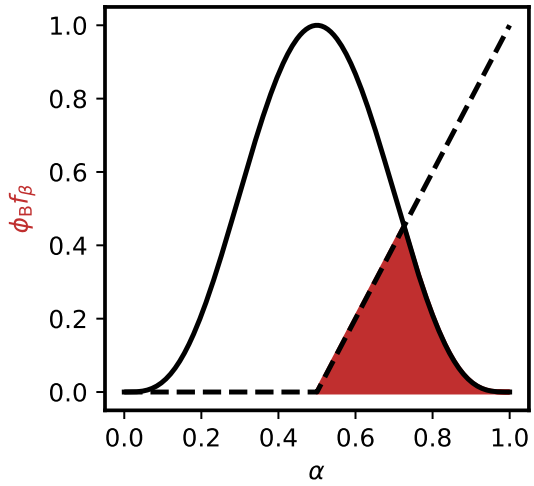

Figure 2.5 Representation of the product $\phi_B f_\beta$. It is valid for all the products in Eqs. (2.27), (2.28) and (2.29) and for any value of $\bar{\alpha}$ and I_s.

The central idea of this approach lies in encapsulating the impact of turbulence on the chemistry through the functional expression, f_β. This is because the chemical reactions happen so rapidly compared to the mixing timescale. Figure 2.5 shows that when I_s is low but other than zero, the mixing (f_β) plays a role and it can be mathematically accounted for by multiplying the f_β with the concentration in perfectly micro-mixed conditions resulting in the red area. Moreover, in CFD applications, tackling the integrals described in Eqs. (2.27), (2.28) and (2.29) can be quite time-intensive, especially for equilibrium and non-isothermal reactions. Consequently, to mitigate this, the values of these integrals are computed beforehand. This pre-computation involves evaluating the integrals only for a limited set of mean mixture fraction values ranging from 0 to 1, and variance of the mixture fraction values from 0 to $\bar{\alpha}(1-\bar{\alpha})$. This collected data is then organized into a lookup table. The integral values (computed only once) are stored at specific points (nodes) in this table, and to estimate integral values between these nodes, bi-linear interpolation is employed. Moreover, Eqs. (2.27), (2.28) and (2.29), to compute the nodes' values, have been solved analytically, and the integration procedure is given in the appendix A.1.

2.3 Precipitation Modelling

Precipitation is a special type of crystallization, also known as *reactive crystallization*, in which the time scales of solid formation are much smaller than the supersaturation generation (i.e., the time required for the reaction to occur). The typical phenomena of precipitation processes can be divided into primary and secondary [76]. Primary or molecular processes include primary nucleation (homogeneous and heterogeneous) and growth. These processes are called primary or molecular because they are responsible for the transfer of solid from the aqueous phase (solute molecules) to the solid phase (precipitated solid). In this thesis, solids formed as a consequence of primary processes will be called 'primary particles'. Secondary processes, on the other hand, include aggregation and agglomeration. These processes are termed secondary because they refer to the interaction between primary particles which may aggregate or agglomerate to form secondary particles. The term secondary particles is, subsequently, also extended to the interaction between primary particles with newborn secondary particles or between secondary particles and secondary particles. The description of the particle assemblage and interaction encounters challenges due to conflicting definitions of "agglomerates" and "aggregates" among different authors and sources [77, 78]. To summarize, the following terminologies will be employed:

- Primary particles refer to individual crystals or crystals composed of crystallites (or grains).
- Aggregates consist of primary and/or secondary particles that are bound together by strong chemical bonds, resulting in resistance to disruption from fluid shear stresses and sonication.
- Agglomerates, on the other hand, involve relatively loose arrangements of primary particles primary and/or secondary, held together by weak crystalline bridges, soaked liquid or electrostatic forces. Agglomerates are weaker than aggregates and can be separated through physical treatments such as sonication and stabilized through anti-agglomeration agents.

Moreover, in precipitation processes, the effect of secondary nucleation is usually neglected, since it is peculiar to those systems in which supersaturation is low, namely close to the metastable region [79].

Supersaturation

The driving force in precipitation processes is represented by supersaturation, S, which indicates the excess of solute in the aqueous phase with respect of its solubility limit represented instead by the solubility product k_{sp}. In rigorous terms, the driving force can be expressed as the difference between two chemical potentials, $\Delta\mu^{cp}$. The first is that of the molecules in solution, μ_s^{cp}, while the second is that in the bulk of the solid particle, μ_p^{cp}:

$$\Delta\mu^{cp} = \mu_s^{cp} - \mu_p^{cp} \tag{2.30}$$

It can be assumed that the chemical potential of the molecules in the bulk of the particle coincides with the equilibrium potential between the particle and the solution, μ_{eq}^{cp}:

$$\mu_p^{cp} = \mu_{eq}^{cp} \tag{2.31}$$

The chemical potential of the molecule in solution, on the other hand, is expressed as:

$$\mu_s^{cp} = \mu_{eq}^{cp} + k_B T \ln(a/a_{eq}) \tag{2.32}$$

Here, k_B is the Boltzmann constant, T is the temperature, a and a_{eq} are the actual molecules' activity in the solution and the equilibrium one. For ionic compounds that dissociate completely in solution, the chemical potential can be written as:

$$\mu_s^{cp} = n_1\mu_{s,1}^{cp} + n_2\mu_{s,2}^{cp} + \ldots + n_m\mu_{s,m}^{cp} \tag{2.33}$$

Here, n_i is the number of moles of the i^{th} ion in the molecule and $\mu_{s,i}^{cp}$ is its corresponding chemical potential. In the case of magnesium hydroxide, supersaturation is generated when the concentration of Mg^{2+} and OH^- increases and, subsequently, $Mg(OH)_2$ is formed, following the reaction:

$$Mg^{2+}_{(aq)} + 2OH^-_{(aq)} \rightarrow Mg(OH)_{2(s)} \downarrow \tag{2.34}$$

Therefore the $\Delta\mu^{cp}$ can be expressed combining Eqs. (2.30), (2.31), (2.32), (2.33):

$$\Delta\mu^{cp} = k_B T \ln\left(\frac{a_{Mg^{2+}}\, a_{OH^-}}{a_{Mg^{2+},eq}\, a_{OH^-,eq}}\right) \tag{2.35}$$

Therefore, it follows that:

$$S = \frac{a_{\mathrm{Mg^{2+}}}\, a_{\mathrm{OH^-}}}{a_{\mathrm{Mg^{2+},eq}}\, a_{\mathrm{OH^-,eq}}} - 1 \tag{2.36}$$

Primary Nucleation

The term primary nucleation includes both homogeneous and heterogeneous nucleation, which involves the formation of stable nuclei without the presence of solute crystals. Following Classical Nucleation Theory (CNT), it is assumed that when the driving force is sufficiently high, the collisions between solute molecules are such that they form molecular clusters. If the molecular clusters exceed a certain critical size (L_c), the Gibbs free energy (ΔG) associated with the cluster is such that the cluster is stable and a new nucleus is formed. The primary nucleation rate, J, is usually expressed as follows [80–85]:

$$J = \underbrace{A_1 \mathrm{e}^{\left(-\frac{B_1}{\ln^2(S+1)}\right)}}_{\text{Homogeneous}} + \underbrace{A_2 \mathrm{e}^{\left(-\frac{B_2}{\ln^2(S+1)}\right)}}_{\text{Heterogeneous}} \tag{2.37}$$

Here A_1 and A_2 $\left(\text{particle no. m}^{-3}\text{s}^{-1}\right)$ represent the maximum value of homogeneous and heterogeneous nucleation rates, respectively. B_1 and B_2 (dimensionless), on the other hand, are related to properties that relate the liquid and solid phases, such as the interfacial tension γ_{sl}. The value of B_1 is proportional to the value of γ_1^{sl}, representing the value of the interfacial tension between the liquid and the solid under study (i.e., liquid-$\mathrm{Mg(OH)_2}$). On the other hand, the value of B_2 is proportional to the value of γ_2^{sl}, which represents the value of the interfacial tension between the liquid and any foreign solid (i.e., liquid-foreign solid), such as impurities.

Molecular Growth

The growth of a primary particle is a two-stage process. The first involves the diffusion of solute molecules from the bulk of the liquid phase to the particle surface (diffusion step). The second consists of the incorporation of solute molecules into the particle lattice (integration step). Depending on the operating conditions that result, therefore, in a supersaturation profile, the growth mechanism can be either diffusion- or integration-controlled. A common expression to describe molecular

growth is the power-law [41, 72]:

$$G = k_{\mathrm{g}} S^{\mathrm{g}} \tag{2.38}$$

Here, k_{g} $\left(\mathrm{ms}^{-1}\right)$ modulates the growth rate while the exponent g (dimensionless) describes the mechanism. For example, when g equals 1, the growth process is controlled by diffusion, and the term k_{g} coincides with the mass exchange coefficient, k_{d}, between the liquid bulk and the solid interface. In that case, the following equalities can be easily derived:

$$G = \frac{ShDM_{\mathrm{p}}}{L\rho_{\mathrm{p}}k_{\mathrm{v}}}\left(a - a_{\mathrm{eq}}\right) = \frac{ShDM_{\mathrm{p}}}{L\rho_{\mathrm{p}}k_{\mathrm{v}}}a_{\mathrm{eq}}S \tag{2.39}$$

$$k_{\mathrm{g}} = k_{\mathrm{d}} = \frac{ShDM_{\mathrm{p}}a_{\mathrm{eq}}}{L\rho_{\mathrm{p}}k_{\mathrm{v}}}, \quad \mathrm{g} = 1 \tag{2.40}$$

Here, D is the diffusion coefficient of the ion in the solution, M_{p} is the molecular weight of the particle, L is the particle size, ρ_{p} is the particle density, k_{v} is the shape factor and Sh is the Sherwood number. The Sherwood number can be calculated using some semi-empirical correlations [76, 86]:

$$Sh = 2 + 0.52Re_{\mathrm{p}}^{0.52}Sc^{1/3} \tag{2.41}$$

$$Re_{\mathrm{p}} = \left(\frac{\varepsilon L^4}{\nu^3}\right)^{1/3} \tag{2.42}$$

$$Sc = \frac{\nu}{D} \tag{2.43}$$

Here, Re_{p} is the Reynolds number for colloidal particles and Sc is the Schmidt number. Although in Eq. (2.39) there are no parameters to be experimentally fit, it is not possible to use this expression because the growth mechanism is not known *a priori*. One can, therefore, use a general expression (Eq. (2.38)), and if parameters fitting results in g equal to 1, it could be inferred that the growth mechanism is diffusion-controlled.

Secondary processes

In addition to the primary processes, particles are subject to the action of secondary processes such as aggregation, agglomeration and breakage. Although the focus

will be on aggregation, a brief explanation of agglomeration and breakage is also reported in this section. The term agglomeration refers to that process whereby, as a result of the collision between particles, weak interaction bonds are formed such as:

- Van der Waals forces or weak electrostatic forces
- Weak forces due to the surrounding liquid

This process, therefore, is completely reversible because the forces involved are such that they can be overcome by chemical and/or physical treatments. It is possible, for example, to stabilize the particle suspension by appropriately changing its ionic strength, or by adding stabilizing agents known as anti-agglomeration agents (chemical treatments). Otherwise, suspended particles can be de-agglomerated by sonication (physical treatment). Regardless of the treatment used, it is therefore always possible to change the state of agglomerates by separating the primary/secondary particles from which they are formed. For this reason, agglomeration is also known as *reversible aggregation* [87]. The second secondary process discussed is aggregation. In this case, the interaction forces holding primary/secondary particles together are extremely strong [81] such as strong crystalline bonds. These forces cannot be overcome through either physical or chemical treatments. For this reason, therefore, we speak of *irreversible aggregation*. The last secondary process is breakage. Cluster breakage occurs when forces, that act on the particle, can overcome the strength of the material. The mechanical forces such as to overcome the strength of the material inducing its failure are:

- Combination of normal and shear stress
- Forces arising as a result of cluster collisions
- Forces arising as a result of cluster-wall collision
- Forces arising as a result of the interaction between clusters and moving and/or rotating mechanical components

It is also worth noting that the breakage of clusters such as aggregation and agglomeration are particularly affected by the operating conditions and the material under consideration. It is, therefore, difficult to model and predict their mechanism in an absolute sense. Consider, for example, the breakage. It might be the case that high

loads, above the breaking limit of the material, acting however few times do not induce cluster breakage. Conversely, it might be the case that loads much lower than the breaking limit of the material acting, however, for long times or in a cyclic manner lead to cluster failure [88]. It is easy to see, then, how dependent these processes are on the system under investigation. Ultimately, as anticipated at the beginning of the section, only aggregation will be deepened of all the secondary processes. This choice is dictated by the fact that agglomeration can easily be decoupled from the other phenomena by being reversible whereas the breakage of nanometric particles would require such high forces or long cycles that it can be neglected.

Aggregation

Particle aggregation is a two-step process, analogous to the process of molecular growth with the difference that during growth a molecule is ideally integrated into the particle structure and, instead, during aggregation another particle is integrated through the formation of a solid crystalline bridge. For aggregation to occur, two conditions must be met:

1. **Collision event.** Two particles (primary and/or secondary) must approach each other through a transport mechanism to the point of collision.
2. **Aggregation efficiency**. As a consequence of the collision and, therefore, contact, there must be enough time for a solid crystalline bridge to form between the two particles such that it cannot be broken.

The aggregation rate, β_{agg}, therefore, will be proportional to the product of collision frequency, β_{col}, and aggregation efficiency, η_{agg}, being the two steps in series:

$$\beta_{\text{agg}} = \beta_{\text{col}} \eta_{\text{agg}} \tag{2.44}$$

The collision frequency represents the sum of collision events (step 1.) in the unit of time. The mechanisms as a result of which collision events can occur are (i) the solution thermal agitation and (ii) the fluid velocity fluctuations due to turbulence. The first mechanism, due to Brownian motion, is named Brownian or perikinetic aggregation while the second, due to turbulence in the system, is known as turbulent

or orthokinetic aggregation. Brownian aggregation rate, β_{br}, is defined as [89]:

$$\beta_{\text{br}} = \frac{2k_{\text{B}}T}{3\mu}\frac{(L+\lambda)^2}{L\lambda} \tag{2.45}$$

Here, k_{B} is the Boltzmann constant, T is the temperature, μ is the fluid dynamic viscosity, L and λ are the sizes of the colliding particles. Turbulent aggregation rate, on the other hand, depends on turbulent fluctuations. In the turbulent regime, the energy supplied to the system results in the formation of larger eddies that transfer their energy to smaller eddies at the level of which it is dissipated through viscous interactions. The characteristic size of the smallest eddies is the size of the Kolmogorov micro-scale η_k:

$$\eta_k = \left(\frac{\nu^3}{\varepsilon}\right)^{1/4} \tag{2.46}$$

Here, ν is the kinematic viscosity and ε is the turbulent kinetic energy dissipation rate. Turbulent aggregation rate, β_{tr}, is in turn divided into two mechanisms:

- **Viscous sub-range mechanism:** this mechanism affects the aggregation of particles with sizes smaller than the Kolmogorov micro-scale.
- **Inertial sub-range mechanism:** this mechanism influences the aggregation of particles with sizes larger than the Kolmogorov micro-scale.

The turbulent aggregation rate for particles subject to the viscous sub-range mechanism was studied by Saffman and Turner [90]. Based on their work, the collision frequency can be expressed as:

$$\beta_{\text{tr}}^{\textbf{vis}} = \sqrt{\frac{8\pi}{15}}\sqrt{\frac{\varepsilon}{\nu}}\frac{(L+\lambda)^3}{2} \tag{2.47}$$

On the other hand, the turbulent aggregation rate for particles subject to the inertial sub-range mechanism was studied by Abrahamson [91]. In this case, the collision frequency can be expressed as:

$$\beta_{\text{tr}}^{\textbf{inr}} = 2^{3/2}\sqrt{\pi}\frac{(L+\lambda)^2}{4}\sqrt{\left(\mathbf{u}_L^2+\mathbf{u}_\lambda^2\right)} \tag{2.48}$$

Here, $\mathbf{u}_L$ and $\mathbf{u}_\lambda$ are the velocities of colliding particles. To understand, therefore, which of the two mechanisms the particles will be subject to, it is sufficient to look

at the Stokes number, St, of the particle defined as the ratio of the particle time scale, $\left(\frac{\rho_p L^2}{18\rho_s \nu}\right)$, to the characteristic time, $\sqrt{\frac{\nu}{\varepsilon}}$, of the Kolmogorov micro-scale. If the Stokes number is less than or, at most, of the order of magnitude of 1 then it can be assumed that the particles will have the same velocity as the fluid and, therefore, will be subjected only to the viscous sub-range mechanism. For Stokes numbers greater than 1, however, particle inertia will not be negligible. The particles, therefore, will move with a velocity different from that of the fluid, and the dominant aggregation mechanism will be that of the inertial sub-range. In precipitation, it is easily verified that the Stokes number is less than 1. Under these conditions, as mentioned, it can be assumed that the only turbulent aggregation mechanism is that of viscous sub-range, and if the particle sizes are small enough (i.e., roughly for sizes from a few tens of nanometers up to the order of 1-10 µm). In addition, it can be assumed that the Brownian and turbulent mechanisms act in parallel on the particles, and as a result, the two contributions can be summed [92]:

$$\beta_{\text{col}} = 10^{C_T} \left(\beta_{\mathbf{br}} + \beta_{\text{tr}}\right) \tag{2.49}$$

Here, the parameter C_T represents a correction factor to consider any deviation from the condition in which the aggregation kernels were derived [72, 93]. The second step for aggregation to occur is for the impact to be effective. It is necessary, therefore, that the particles actually have time to form a solid crystalline bridge [94]. This contribution is represented by aggregation efficiency. Two functional forms have been developed depending on the system [95, 96]:

$$\eta_{\text{agg}} = e^{-\theta} \tag{2.50}$$

$$\eta_{\text{agg}} = (1+\theta)^{-1} \tag{2.51}$$

Here, θ represents the ratio between the cementation time, t_{cem}, and the interaction time, t_{int}. The interaction time is equal to the characteristic time of the Kolmogorov micro-scale:

$$t_{\text{int}} = \sqrt{\frac{\nu}{\varepsilon}} \tag{2.52}$$

and represents the time during which the two particles are close enough to interact while the cementation time is defined as:

$$t_{\text{cem}} = \frac{D_{\text{b}}}{f(\delta)\, G} \tag{2.53}$$

$$D_{\text{b}} = \frac{L_{\text{eqv}} \rho_{\text{p}}^{0.5} \left(\varepsilon \nu\right)^{0.25}}{A_{\text{p}}^{0.5}} \tag{2.54}$$

$$L_{\text{eqv}} = \frac{L\lambda}{\left(L^2 + \lambda^2 - L\lambda\right)^{0.5}} \tag{2.55}$$

It represents the time required for the irreversible formation of a solid crystalline bridge to occur. Here, A_{p} is a tuning parameter that refers to the solid crystalline bridge strength and $f(\delta)$ is a shape function defined as follows [97]:

$$f(\delta) = \frac{4\left(1 + \delta - \delta'\right)}{1/3 + \delta - \delta' - \left(\delta - \delta'\right)^2 \left(2\delta/3 + \delta'/3\right)} \tag{2.56}$$

$$\delta = L/\lambda \tag{2.57}$$

$$\delta' = \sqrt{\delta^2 - 1} \tag{2.58}$$

Both Eqs. (2.50) and (2.51) describe the probability of an impact being effective by comparing precipitation and hydrodynamic conditions. Cementation time indicates the time required for a solid crystalline bridge to form irreversibly. If this time is of the same order or less than the interaction time then the collision between the particles will be effective (i.e., $\eta_{\text{agg}} \to 1$). In the case where, on the other hand, the time required to cement two particles together is longer than the interaction time then the impact will not be effective (i.e., $\eta_{\text{agg}} \to 0$).

Population Balance Model

The evolution of particle size is a critical parameter that significantly influences product quality, process efficiency, and resource utilization. Understanding and predicting how particles change in size over time is essential for designing and optimizing processes. A powerful tool for addressing this challenge is the Population Balance Model (PBM). A PBM is based on the resolution of a Population Balance Equation (PBE) [98]. In this section, therefore, PBE and the techniques most

commonly used for its resolution are presented. Although crystallization is a unitary operation in chemical engineering widely used and established, PBE was initially applied starting from ideal systems and then extended. For example, the ideal system most widely considered is the mixed-suspension mixed-product removal (MSMPR) [99]. In the case of MSMPR, PBE's solution is valid for a perfectly mixed and homogeneous system. This results in considerable simplification, to the point that, in some cases, there is an analytical solution to the PBE. Obviously, in real crystallizers, these simplifications do not apply, especially when considering the inhomogeneity of turbulent properties within the reactor. For this reason, therefore, there was a move to gradually more sophisticated models that, for example, also considered the fluid dynamics of the coupling system CFD with PBE. Given, therefore, the increasing computational demands, methods were developed to achieve an optimal trade-off between reliable solutions and computational time. Up to date, PBE integration methods can be divided into four main categories: (i) stochastic methods, Multi-Class Methods (MCM) (ii), Weighted Residual Methods (WRM) (iii) and (iv) the methods of moments [100]. Among all the methods mentioned, only the methods of moments will be referred to in this thesis with a focus on the Quadrature Method of Moments (QMOM).

Population Balance Equation

The PBE for a system in which PSD varies in time and space is given below:

$$\frac{\partial \bar{n}}{\partial t} + \frac{\partial}{\partial x_i}\left(\bar{u}_i \bar{n}\right) + \frac{\partial}{\partial L}\left(G\bar{n}\right) = h \tag{2.59}$$

Here:

- $\bar{n}(t, \mathbf{x}, L)$ represents the Reynolds-Averaged Particle Size Distribution (PSD), describing the distribution of particles over time (t), spatial coordinates ($\mathbf{x}$), and a characteristic property (typically size, denoted as L).
- $\frac{\partial \bar{n}(t,\mathbf{x},L)}{\partial t}$ represents the rate of change of the population density concerning time.
- $\frac{\partial}{\partial x_i}\left(\bar{u}_i \bar{n}(t, \mathbf{x}, L)\right)$ involves the divergence of the flux ($\bar{\mathbf{u}}\bar{n}(t, \mathbf{x}, L)$), representing the change in population within a region due to the flow.

- $\frac{\partial(G\bar{n}(t,\mathbf{x},L))}{\partial L}$ denotes the change in population density, with G often representing a growth or dissolution term.
- $h(t,\mathbf{x},L)$ accounts for additional sources or sinks in the population, such as aggregation and/or breakage.

The term on the right-hand side of Eq. 2.59 can be mathematically closed. Let's consider a scenario where the only relevant phenomena are aggregation and breakage. Consequently, the source term is then expressed as:

$$h = \frac{1}{2}\int_0^L \beta_{\text{agg}}(L-L')n(L-L')n(L)\mathrm{d}L' + \int_L^\infty \beta_{\text{brk}}(L')\beta_{\text{dgt}}(L|L')n(L')\mathrm{d}L' \\ - n(L)\int_0^\infty \beta_{\text{agg}}(L,L')n(L')\mathrm{d}L' - \beta_{\text{brk}}(L)n(L) \tag{2.60}$$

Here β_{agg} denotes the aggregation rate between two particles of sizes L and L', β_{brk} signifies the breakage rate between particles with sizes L and L', and β_{dgt} characterizes the daughter distribution. The daughter distribution reflects the resultant distribution emerging after a particle breakage [101].

Quadrature Method of Moments

A widely used method, especially in the framework of RANS simulations, is the QMOM [102–104]. This method exploits the quadrature approximation of moments as follows:

$$m_k = \int_0^\infty n\,(t,\mathbf{x},L)L^k\mathrm{d}L \simeq \sum_i w_i L_i^k \tag{2.61}$$

Here w_i are the weights and L_i are the abscissas. The Gauss quadrature method calculates the integral of a function by defining N weights and abscissas, resulting in an order of $2N-1$. The abscissas and weights can be fully specified in terms of low-order moments. For example, to obtain a quadrature method of order $N=3$, it is sufficient to know the first $2N=6$ moments. The weights and abscissas can be calculated by exploiting the product-difference (PD) or the adaptative Wheeler algorithms (see Appendix A.1). Once the values of weights and integration nodes are obtained, it is possible to solve the equations that approximate the moments. Starting from Eq. (2.59), for the first 6 moments of the distribution, the following set

of differential equations is obtained:

$$\frac{\partial \bar{m}_k}{\partial t} + u_i \frac{\partial \bar{m}_k}{\partial x_i} = \frac{\partial}{\partial x_i}\left(D_t \frac{\partial \bar{m}_k}{\partial x_i}\right) + h_k \tag{2.62}$$

$$h_k = J_k L_c^k + k \sum_{i=1}^{N} G L_i^{k-1} w_i + \frac{1}{2} \sum_{i=1}^{N} w_i \sum_{j=1}^{N} w_j \beta_{agg} (L_i^3 + L_j^3)^{\frac{k}{3}} - \sum_{i=1}^{N} w_i L_i^k \sum_{j=1}^{N} w_j \beta_{agg} \tag{2.63}$$

where L_c is the critical size of nuclei [105]. From left to right in Eq. 2.63, we find terms associated with nucleation, growth, and aggregation, which modify the moments of the PSD.

Mass Balance

The chemical reaction induces supersaturation, prompting the precipitation of the product as it shifts from the aqueous matrix to a solid state. The rate of this transition is predominantly influenced by the specific chemical species undergoing precipitation and the operating conditions, such as the temperature. Therefore, a mass balance is necessary to account for this mass transfer. The concentration of the i-th reactive ion changes as follows:

$$\frac{\partial \bar{c}_i}{\partial t} + \frac{\partial}{\partial x_i}(\bar{u}_i \bar{\bar{c}}_i) = \frac{\partial}{\partial x_i}\left(D_t \frac{\partial \bar{c}_i}{\partial x_i}\right) + Q_i \tag{2.64}$$

Here Q_i is the sink term associated with the precipitation. It can be further expanded as follows:

$$Q_i = -\frac{\nu_i \rho_\mathrm{p} k_\mathrm{v}}{M_\mathrm{p}} \frac{\partial m_3}{\partial t} \tag{2.65}$$

Here ν_i is the stoichiometric coefficient in the precipitation reaction, ρ_p is the particle density, k_v is the shape factor ($\pi/6$ for spheres) and M_p is the molecular weight of the precipitating species.

Equations Summary

In this paragraph, a summary of the presented equations is reported.

Navier-Stokes Equation:

$$\frac{\partial \bar{u}_i}{\partial t} + \bar{u}_j \frac{\partial \bar{u}_i}{\partial x_j} = \frac{\partial}{\partial x_j}\left(\nu\left(\frac{\partial \bar{u}_i}{\partial x_j} + \frac{\partial \bar{u}_j}{\partial x_i}\right) - \overline{u_i' u_j'}\right) - \frac{1}{\rho}\frac{\partial \bar{p}}{\partial x_i} + \mathrm{g}_i$$

Turbulent Kinetic Energy Equation:

$$\frac{\partial k}{\partial t} + \bar{u}_i \frac{\partial k}{\partial x_i} = \frac{\partial}{\partial x_i}\left((\nu + \sigma_k \nu_t)\frac{\partial k}{\partial x_i}\right) + P_\varepsilon - \varepsilon$$

Turbulent Dissipation Rate Equation:

$$\frac{\partial \varepsilon}{\partial t} + \bar{u}_i \frac{\partial \varepsilon}{\partial x_i} = \frac{\partial}{\partial x_i}\left((\nu + \sigma_\varepsilon \nu_t)\frac{\partial \varepsilon}{\partial x_i}\right) + C_{\varepsilon 1}\frac{\varepsilon}{k}P_\varepsilon - C_{\varepsilon 2}\frac{\varepsilon^2}{k}$$

Transport Equation for $\bar{\alpha}$:

$$\frac{\partial \bar{\alpha}}{\partial t} + \bar{u}_i \frac{\partial \bar{\alpha}}{\partial x_i} = \frac{\partial}{\partial x_i}\left(D_t \frac{\partial \bar{\alpha}}{\partial x_i}\right)$$

Transport Equation for $\overline{\alpha'^2}$:

$$\frac{\partial \overline{\alpha'^2}}{\partial t} + \bar{u}_i \frac{\partial \overline{\alpha'^2}}{\partial x_i} = \frac{\partial}{\partial x_i}\left(D_t \frac{\partial \overline{\alpha'^2}}{\partial x_i}\right) + 2D_t\left(\frac{\partial \bar{\alpha}}{\partial x_i}\cdot\frac{\partial \bar{\alpha}}{\partial x_i}\right) - C_f \frac{C_\phi}{2}\frac{\varepsilon}{k}\overline{\alpha'^2}$$

Transport Equation for m_k:

$$\frac{\partial \bar{m}_k}{\partial t} + u_i \frac{\partial \bar{m}_k}{\partial x_i} = \frac{\partial}{\partial x_i}\left(D_t \frac{\partial \bar{m}_k}{\partial x_i}\right) + JL_\mathrm{c}^k + kGm_{k-1} + \overline{B}_k - \overline{D}_k$$

Transport Equation for $\bar{c}_i$ (reacting ions):

$$\frac{\partial \bar{c}_i}{\partial t} + \bar{u}_i \frac{\partial \bar{c}_i}{\partial x_i} = \frac{\partial}{\partial x_i}\left(D_t \frac{\partial \bar{c}_i}{\partial x_i}\right) - \frac{\nu_i \rho_\mathrm{p} k_\mathrm{v}}{M_\mathrm{p}}\frac{\partial m_3}{\partial t}$$

Chapter 3

Mixing and Reaction in T-Mixers

Some of the work described in this chapter has also been previously published in Battaglia et al. [106] (Experimental activities were done in collaboration with the University of Palermo).

Mixing serves as a cornerstone process that actively reduces gradients in composition, properties, and temperature within fluid systems, thereby influencing the dynamics and outcomes of the final products. Mixing has immense significance in industries such as biotechnology, pharmaceuticals, and food processing [107], as well as nuclear engineering [59, 108–111] and chemical engineering fields [11, 70, 112, 113]. This chapter embarks on a comprehensive exploration of mixing in static mixers, laying the groundwork for understanding how mixing influences precipitation processes. Over the past few decades, there has been considerable exploration into micro- and millimeter-sized static mixers through both numerical simulations and experiments [114, 115]. Particular attention has been drawn to Confined Imping Jets (CIJs) [116, 117] and T- or Y-shaped mixers [40, 118].

In the last 40 years, micro- and millimetre-sized static mixers have been extensively investigated both numerically and experimentally [115, 114]. Much attention has been drawn by Confined Imping Jets (CIJs) [116, 117] and T- or Y- shaped mixers [40, 118].

The relevance of mixing in these devices is still a hot topic in the scientific panorama. Recently, Bie et al. [119] analysed mixing phenomena in a novel T-T jet reactor made of two consecutive T-impinging configurations. The T-T design exhibited better mixing performance compared to classical T-jet configurations.

Mariotti et al. [120] assessed the influence of lateral inclined walls cross-sectional T-mixers. Mixing was moderately improved depending on the wall inclination angle and the fluid flow regime. Li et al. [121] investigated the influence of induced swirling flow on mixing properties in a circular cross-sectional T-mixer. Swirling motion was found to considerably enhance mixing in the device. The vivid research interest in CIJs and T- or Y- shaped mixers is due to the high mixing degree control and short mixing times attained in these devices.

In reactive crystallization systems, short mixing times are required to tune and control the final product characteristics. Most often, circular cross-sectional mixers are adopted since they are easy to build and edge-free. In addition, unbalanced reactants volumetric fluid flow rates can be desired to employ low concentrated reactants, guaranteeing, at the same time, the required molar or mass flow rates. In this context, few works have dealt with the study of mixing phenomena in cross-sectional T- or Y- mixers and even fewer with unbalanced fluid flow rate conditions. Mixing in circular cross-sectional mixers has been characterized experimentally by parallel/competitive consecutive reaction systems Gillian and Kirwan [122], Lindenberg et al. [123], Wojtas et al. [118]. Laminar and turbulent regimes have also been numerically investigated by Direct Numerical Simulations (DNS) [124, 125], Reynolds Averaged Navier-Stokes Equations (RANS) [123] and Large Eddy Simulations (LES) [118]. However, to the best of the authors' knowledge, there is little knowledge available in the literature about experimental spatial information on the mixing phenomena inside circular T- or Y- cross-sectional devices. Furthermore, unbalanced fluid flow rates have mainly been investigated in T- square cross-sectional micro-mixers at Reynolds numbers lower than 1400Roudgar et al. [126], Wong et al. [107], and Confined Imping Jet reactors [127].

The present work aims at filling these gaps. Specifically, the pure dilution of non-reacting species (blue and yellow food dyes) and the chemical reaction of two-coloured reacting species (i.e., sodium hydroxide, NaOH, and hydrochloric acid, HCl, in the presence of an indicator) were experimentally and numerically investigated in two 3 mm hydraulic diameter square and circular cross-sectional T-mixers. A digital image analysis technique was adopted. The pure dilution of non-reacting species in the mixers under unbalanced fluid flow rates condition was assessed for a blue colour fluid flow rate ratio of 2 and 3 with respect to that of the yellow one at Reynolds number of ~ 4000. In the study, instantaneous quantities were considered to better quantify mixing in these devices, which is mainly evaluated based on statistical time

average information. Specifically, the time standard deviation of the mixture fraction along the mixing channel was assessed to thoroughly describe mixing.

The RANS $k-\varepsilon$ model was accurately tuned to well describe turbulence in the devices. Macro- and micro-mixing was described by tracking the mixture fraction and its variance. Macro-mixing occurs at the bulk level via dispersion. It evolves from the characteristic length of a system down to the Kolmogorov scale. Conversely, micro-mixing occurs at the molecular level via shearing or diffusion from the Kolmogorov scale to the Batchelor one. The mixture fraction accounts for a non-reactive scalar transport (i.e., pure species dilution) whereas its variance is related to the reactive scalar transport (i.e., reacting ions, OH-, consumed along the mixing channel coordinate).

To improve the $k-\varepsilon$ model simulations, a new tuning approach was performed involving fitting the parameters in the ε equation according to the theory provided in Pope [128]. In this perspective, $k-\varepsilon$ based models can be tuned to artificially increase the (i) turbulent transport or (ii) the turbulent mixing. In the first case, hydrodynamics constants are varied such as the parameters. In the second case, the turbulent Schmidt number is typically reduced. Note that, the variation of the turbulent Schmidt number does not affect the turbulent transport, but only the scalar transport. Kok and van der Wal [109] reported that the $k-\varepsilon$ model underestimated turbulence in T-junctions. A better prediction of turbulent mixing was obtained when the turbulent Schmidt number (commonly 0.8–0.9) was made to decrease down to 0.2. Similar findings were also reported by Frank et al. [108], who identified a considerable turbulence underestimation in T-junctions by using the $k-\varepsilon$ model. However, Walker et al. [59] observed inaccurate prediction of velocity distributions, although the large difference between the experimental and numerical turbulent dispersion was reduced by decreasing the turbulent Schmidt number. A much more satisfactory experimental and numerical data agreement, in terms of velocity profiles and turbulent dispersion, was achieved by increasing the C_μ parameters, thus increasing the turbulent transport.

In the present work, in addition, in the variance equation, also the C_ϕ parameter was tuned [72]. The tuned undemanding $k-\varepsilon$ model can considerably reduce computational time and costs, compared to more computationally intensive techniques such as DNS [40], LES [118] and unsteady RANS [129]. This can be advantageous in parametric studies that require the characterization of different T-mixer geometries

under several operating conditions, as in the study of the precipitation process of hydroxides in these devices.

3.1 Material and Methods

Experimental setup

The investigation focused on two scenarios: the non-reactive dilution of colourant species, represented by blue and yellow food dyes, and the chemical interaction between dual-hued reactive compounds (i.e., sodium hydroxide, NaOH, hydrochloric acid, HCl). This investigation occurred within the confines of millimetre-scale T-shaped mixers, distinguished by their cross-sectional profiles - either square or circular. For the square configuration, the apparatus was carved into a sheet of plexiglass, complemented by a superimposed lid secured by screws. Conversely, the circular mixer found its form through precise drilling into a solid block. The selection of plexiglass as the fabrication material stemmed from its refractive index (1.49), an approximation to that of glass (1.52). Additionally, to minimize optical distortions, Plexiglas plates, measuring 2 cm in thickness, were employed, with the square mixer utilizing two slabs of 1 cm each. The T-shaped mixers were composed of dual inlet branches oriented horizontally, converging at a focal juncture. Subsequent fluid motion transpired along a central conduit, denoted as the "mixing channel." Key dimensions of these mixers comprised (i) a hydraulic diameter, D_{h}, measuring 3 mm, (ii) inlet branches - 25 times the hydraulic diameter for the square variant and 15 times for the circular one - and (iii) the mixing channel - 50 times the hydraulic diameter for the square design and 30 times for the circular configuration. Refer to Figure 3.1 for visual representations of the mixer geometries.

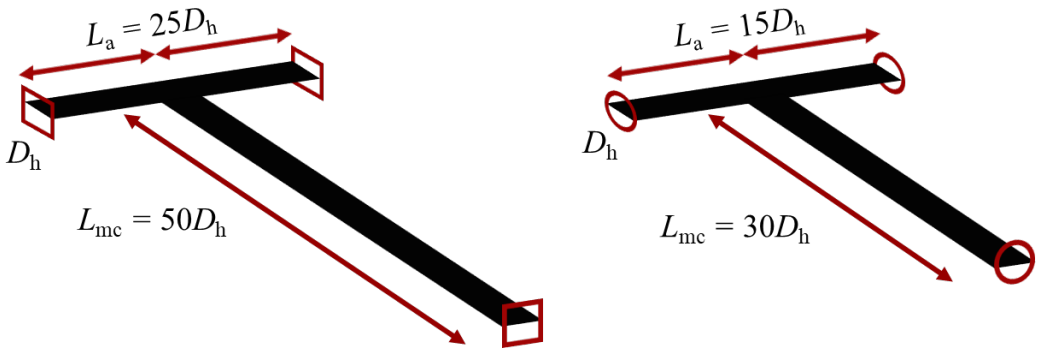

Figure 3.1 Drawings of the square (left) and circular (right) cross-sectional T-shaped mixers

An experimental rig was designed and assembled for this study. To elaborate, the setup encompassed the following components:

- Two distinct weir contraptions were meticulously fabricated to manage solutions, thereby mitigating any potential influence stemming from fluid flow rate fluctuations, which could potentially arise from the utilization of pumps [130]
- The illumination of the mixers was achieved through the application of four halogen bulbs with a temperature of 4000 K. These bulbs served to provide a consistent backlighting effect for the mixers
- For the purpose of capturing images, a Nikon D3300 digital camera was employed, boasting a 24.2-megapixel CCD sensor and a 35 mm F1.8 lens. This camera served as a tool for acquiring visual data.

The entire setup was situated within a controlled dark environment, thus effectively minimizing the impact of external sources of light. A visual representation of the experimental arrangement is depicted in Figure 2.

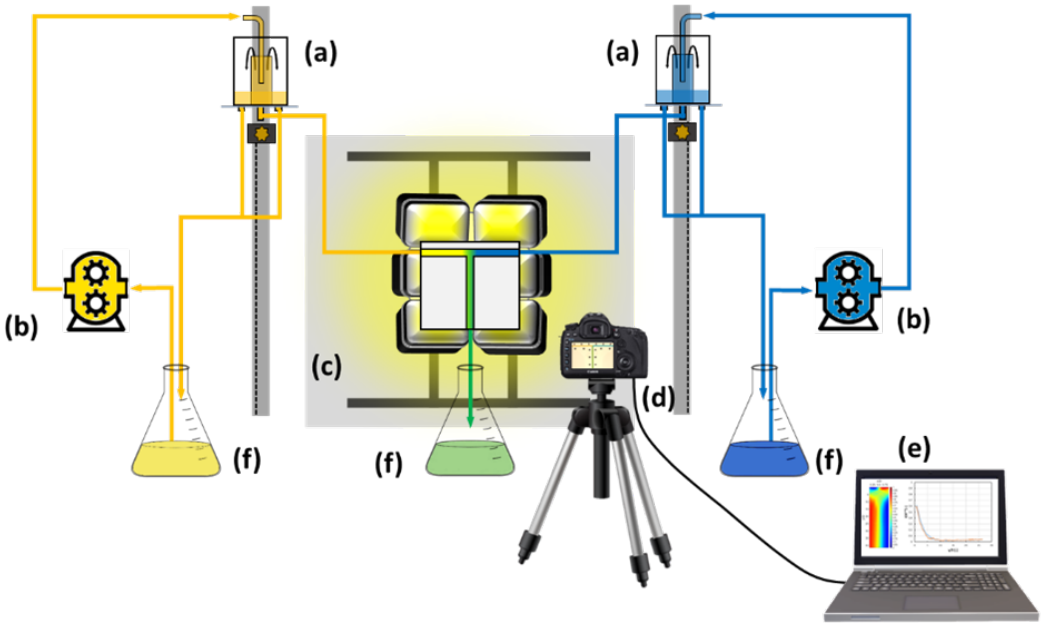

Figure 3.2 Drawing of the experimental setup

The research focused on investigating both macro-mixing and micro-mixing phenomena. The macro-mixing aspect involved studying the dilution process using non-reacting blue and yellow food dyes. In parallel, the micro-mixing phenomenon was explored by observing the neutralization reaction between NaOH and HCl solutions, facilitated by a pH indicator. To create the food dye solutions, 5.79 g of a yellow E102 food-grade dye (with 75% sodium sulfate) and 1.79 g of a blue E131 food-grade dye (containing 97% sodium sulfate) were dissolved in 1 liter of demineralized water. For the neutralization tests, 1 g of Alizarin Yellow R sodium salt pH indicator from Thermo Fisher (Kandel, GmbH) was dissolved in another liter of demineralized water. Next, 7 mL of the Alizarin solution was mixed separately with 500 mL portions of both the HCl and NaOH solutions. The Alizarin yellow R pH indicator undergoes a color change from yellow to deep orange within the pH range of 10 to 12, respectively. This range was particularly suitable for observing the precipitation process of hydroxide compounds. The HCl solution was obtained by diluting a concentrated 37% fuming HCl solution (EMSURE®), while the NaOH solution was created by dissolving NaOH pellets (Honeywell FlukaTM, with an assay exceeding 98%). The concentrations were adjusted to 0.010 M for HCl and 0.011 M for NaOH, and their compositions were verified through titration. Experiments were conducted within square and circular cross-sectional T-mixers at Reynolds numbers

of approximately 3900, 5350, and 6600. The Reynolds numbers for these tests were determined within the mixing channel using the following formula:

$$Re = \frac{\rho |\mathbf{u}| D_{\mathrm{h}}}{\mu} \tag{3.1}$$

Unbalanced fluid flow rates were examined exclusively in instances involving the pure dilution of non-reacting food dyes. The fluid flow rate of the blue dye was set at 2 and 3 times the rate of the yellow dye. To ensure meaningful comparisons, all the experiments involving Unbalanced flow rates were carried out under similar Reynolds numbers, approximately 3900. All the tested conditions, both for the square (#S) and circular (#C) cross-sectional T-mixers, are comprehensively outlined in Table 3.1 and Table 3.2, respectively. Both tables show, respectively, the condition number studied, the phenomenon considered (D for dilution, N for neutralization, and D/N for both), the average flow rate processed, the average velocity, and the Reynolds number in the mixing channel.

Table 3.1 Investigated cases in the square cross-sectional T-mixer

Case	Investigated phenomenon	Average Flow Rate, [ml/min]	Average Velocity, [m/s]	*Re*
#S1	D	700	1.30	3900
#S2	D / N	960	1.78	5350
#S3	D	1185	2.19	6660
#S4	D (1:2)	720	1.33	4000
#S5	D (1:3)	670	1.24	3700

Table 3.2 Investigated cases in the circular cross-sectional T-mixer

Case	Investigated phenomenon	Average Flow Rate, [ml/min]	Average Velocity, [m/s]	*Re*
#C1	D	560	1.32	4000
#C2	D / N	750	1.77	5300
#C3	D	930	2.19	6600
#C4	D (1:2)	580	1.37	4100
#C5	D (1:3)	520	1.24	3700

Performance parameters

In the context of the food dye dilution process, the mixture fraction of the blue dye, denoted as φ, is monitored as it evolves over both time (across multiple images) and along the dimensions of the mixing channel, encompassing both its length and width. As such, φ emerges as a variable that is inherently dependent on both spatial coordinates and time. The range of variation for φ spans from 0, which corresponds to the pure yellow colour, to 1, signifying the pure blue colour. For a given point in the mixing channel characterized by specific length (y) and width (x) coordinates, an averaged mixture fraction $\bar{\varphi}(x,y)$ can be computed. This averaged value represents the mean of φ taken over the ensemble of acquired images:

$$\bar{\varphi}(x,y) = \frac{\sum_{i=1}^{N_\mathrm{p}} \varphi(x,y,t_i)}{N_\mathrm{p}} \tag{3.2}$$

Here, i is the i^{th} processed picture and N_p is the total number of processed pictures. The field $\bar{\varphi}(x,y)$ can further undergo an additional averaging procedure across the width (x-coordinate) of the T-mixers. This averaging is performed for a fixed y-coordinate, resulting in a profile that varies as a function of y:

$$\hat{\bar{\varphi}}(y) = \frac{\sum_{i=1}^{N_{\mathrm{x-pixel}}} \bar{\varphi}(x_i,y)}{N_{\mathrm{x-pixel}}} \tag{3.3}$$

Here, $N_{\mathrm{x-pixel}}$ represents the total number of pixels along the x-coordinate, namely 57 and 41 for the square and circular cross-sectional mixers. $\hat{\bar{\varphi}}(y)$ is equal to 0.5 if equal flow rates for both solutions are employed; or 0.667 and 0.75 if the blue mixture fraction flow rate is 2 or 3 times that of the yellow colour, respectively. The degree of homogenization, namely the mixing efficiency in the mixers, between blue and yellow solutions can be quantified by adopting different performance parameters presented in the literature. Among the others, the segregation index I_s [40, 121] is defined as follows:

$$I_\mathrm{s} = \frac{\sigma_\mathrm{y}}{\sigma_{\max}} \tag{3.4}$$

σ_y is the mean square spatial deviation of the time average blue mixture fraction at a certain channel length y:

$$\sigma_y = \sqrt{\frac{\left[\sum_{x=1}^{N_{x-pixel}} \left(\bar{\varphi}(x,y) - \hat{\bar{\varphi}}(y)\right)^2\right]}{N_{x-pixel}}} \tag{3.5}$$

σ_{max} is the mean square spatial deviation occurring for segregated solutions:

$$\sqrt{\hat{\bar{\varphi}}\left(1-\hat{\bar{\varphi}}\right)} \tag{3.6}$$

I_s is equal to 0 (1) if solutions are perfectly mixed (completely segregated). Luo et al. [117] argued that when I_s becomes lower than 0.1, a good mixing degree, namely 90 % of the mixing uniformity, is attained and the mixing time can be calculated as:

$$\tau_{90} = L_{90}/u \tag{3.7}$$

Here, L_{90} is the distance from the impinging zone to the channel mixing length at which I_s becomes 0.1. Roelands et al. [131] arbitrarily defined the mixing time in T-mixers, t_r, as:

$$t_r = 12D_h/u \tag{3.8}$$

The degree of homogenization can be also studied considering the time standard deviation, $\sigma_{x,y}^{time}$, of the mixture fraction at a certain location x, y in the mixing channel:

$$\sigma_{x,y}^{time} = \sqrt{\frac{\left[\sum_{x=1}^{N} \left(\varphi(x,y,t_i) - \bar{\varphi}(x,y)\right)^2\right]}{N}} \tag{3.9}$$

A null time standard deviation indicates that the same mixture fraction value is attained at a certain location in the channel at all times. If the local time average mixture fraction value is also equal to that of the perfect mixed solutions $\left(\hat{\bar{\varphi}}(y)\right)$, then a total homogenization of two species is accomplished. To visualize the evolution of the time standard deviation along the mixing channel, in the result section, $\sigma_{x,y}^{time}$ was averaged over the channel width at a certain channel length y, thus yielding:

$$\hat{\sigma}_{x,y}^{time} = \sqrt{\frac{\left[\sum_{x=1}^{N_{x-pixel}} \left(\sigma_{x,y}^{time}\right)^2\right]}{N_{x-pixel}}} \tag{3.10}$$

3.2 Modelling and simulations

The multi-scale nature of turbulence represents a challenge in its modelling, specially when chemical reactions are involved. Reactions only occur when reactants are mixed at the smallest scale (i.e., Batchelor scale, micro-mixing phenomena). In the past years, different approaches have been proposed to account for the interaction between mixing and reactions [68, 69]. The approach introduced by Marchisio and Fox [53] and Baldyga et al. [70] for fast irreversible reactions was followed.

Flow field and turbulence equations

The flow field of a Newtonian, incompressible, fluid is described by the Navier-Stokes and the continuity equations (Eqs. (2.2), (2.1)). Then RANS $k-\varepsilon$ is a two-equation model that solves transport equations for the turbulent kinetic energy, k, and the turbulent kinetic energy dissipation rate, ε (Eqs. (2.4), (2.5)). Pope [128] identified a relation between P_ε and ε:

$$\frac{P_\varepsilon}{\varepsilon} = \frac{C_{\varepsilon 2} - 1}{C_{\varepsilon 1} - 1} \tag{3.11}$$

The $P_\varepsilon/\varepsilon$ is about 2.1 if default $C_{\varepsilon 1}$ and $C_{\varepsilon 2}$ values are adopted, namely 1.44 and 1.92. This ratio can differ in real systems [40]. To increase the reliability of RANS $k-\varepsilon$ model for T-mixers investigations, the $C_{\varepsilon 2}$ parameter was tuned against experimental data, thus increasing the turbulent transport in the devices. It is worth noticing that the same results can be obtained by reducing $C_{\varepsilon 1}$. For convenience, however, only the $C_{\varepsilon 2}$ parameter was made to vary.

Mixing equations

Macro-mixing in the devices can be described through the mixture fraction equation. The mixture fraction is the relative amount of two fluids in a known control volume. In other words, mixture fraction is 0 (or 1) when only A solution (or B) is present and 0.5 when both A and B solutions are equally present. The mixture fraction transport is described by Eq. (2.12). It is worth noticing that the mixture fraction transport is influenced only by the advection and diffusion terms. The diffusive term is responsible for gradients flattening, depending on turbulence conditions, and can

be tuned by varying either Sc_t or C_μ the latter affecting ν_t in Eq. (2.6) [59]. As far as micro-mixing is concerned, it is described through the variance of the mixture fraction transport equation (Eq. (2.14)).

Computational Fluid Dynamics details

CFD simulations were carried out using the open-source OpenFOAM (v8) software. The *twoLiquidMixingFoam* solver was adopted for food dye pure dilution analysis. The variance equation and a user-defined “reaction class" were added to the solver to describe neutralization phenomena. In this regard, an a priori look-up table with 121 nodes was calculated following the theory introduced by Marchisio and Fox [53] (see Appendix A.1). No-slip boundary conditions, scalable wall functions for turbulent properties and zero gradient for the mixture fraction and its variance were set at the walls of the mixers. Normal velocity values, zero gradient for pressure, and initial estimated k and ε values were set at the inlet regions. At the inlets, a null variance was also imposed (pure fluids), while 0 and 1 mixture fractions were set at the opposite inlets. Zero gradient was applied for all quantities at the outlet, with an exception for the pressure that was set to be 0. For the neutralization cases, 0.01 M and 0.011 M concentration values were set for HCl and NaOH concentrations at the inlets. 3 and 1.35 million volumes (>99.9 % hexahedral cells) grids were employed for the square and circular cross-sectional T-mixers. As a preliminary analysis, the flow field was solved by resorting to different turbulence models: $k-\varepsilon$, RNG $k-\varepsilon$, $k-\omega$, $k-\omega$ SST. Since the flow fields solved through the various models were similar, as well as the turbulent properties, the $k-\varepsilon$ model was chosen since it was the least computationally expensive. To conclude numerical average mixture fraction and OH^- concentration profiles were calculated as follows: (i) equispaced cross-sections were considered along the mixing channel length; (ii) at each cross-section, computed mixture fraction or OH^- values were averaged over the channel depth (z-direction in Figure 3.1, thus obtaining profiles along the channel width); (iii) the resulting values were further averaged over the channel width to provide a profile along the mixing channel length. The segregation index was then determined by adopting Eq. (3.4)

3.3 Results and discussion

Pure dilution in the square cross-sectional T-mixer: equal flow rates

RANS simulations are computationally undemanding, but they may require tuning the model parameters. Sc_t, C_μ and $C_{\varepsilon 2}$ were made to vary in the range of 0.1-1, 0.09-0.36 and 1.92-8.36, respectively. Model predictions were compared to experimental data collected for Case #S1. The default values for Sc_t, C_μ, and $C_{\varepsilon 2}$ are 1, 0.09 and 1.92, respectively.

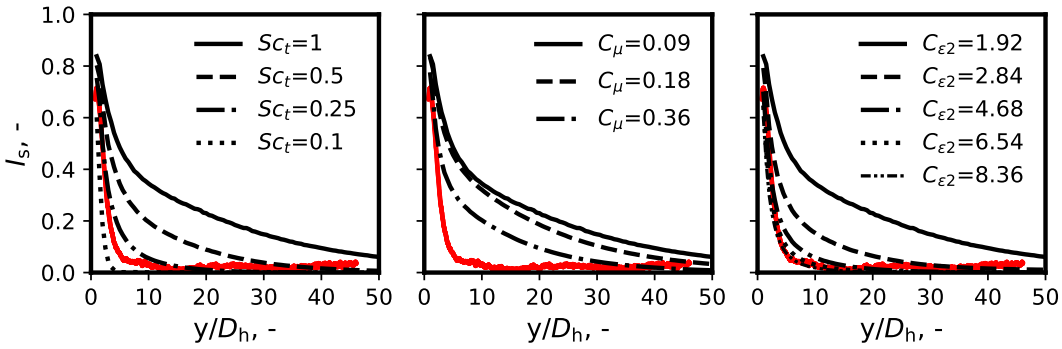

Figure 3.3 Model parameters variation: Sc_t (*left*), C_μ (*center*), $C_{\varepsilon 2}$ (right).

Figure 3.3 shows numerical segregation index profiles along the mixing channel length evaluated for (i) four different Sc_t of 1, 0.5, 0.25, 0.1 (Figure 3.3 - *left*); (ii) three C_μ parameter values of 0.09 (standard value), 0.18 and 0.36 (Figure 3.3 - *center*); and (iii) five $C_{\varepsilon 2}$ values of 1.92 (reference value), 2.84, 4.68, 6.54 and 8.36 (Figure 3.3 - *right*). In all cases, $C_{\varepsilon 1}$ was always kept equal to 1.44 (default value). As expected, the smaller the Sc_t number, the faster the macro-mixing (pure dilution phenomenon), see Figure 3.3 - *left*. A good match between numerical and experimental trends is observed for a Sc_t number of 0.25. Conversely, the model overestimates the experimental data for a Sc_t number of 0.1. Although the fitting is accurate for a Sc_t number of 0.25, values smaller than 0.7 are typically unusual [108, 109]. A better reactants homogenization is attained by increasing the C_μ value, Figure 3.3 - *center*. However, the model underestimates the mixing phenomenon in the device even adopting a C_μ value four times higher than the standard one, namely equal to 0.36. This result is due to the damping effect of the C_μ parameter. While Sc_t

directly influences only D_t (Eq. (2.13)), C_μ directly influences ν_t (Eq. (2.6)). This latter is used to calculate D_t and solve the transport equations of k and ε (Eqs. (2.4) and (2.5)). Figure 3.3 - *right* shows a very good agreement between numerical and experimental data only for $C_{\varepsilon 2}$ values higher than 6.54. This confirms that the $k-\varepsilon$ turbulence model with standard constants underestimates turbulent mixing within static mixers. All the following numerical simulations were then run setting C_ε equal to 6.54. The performances of the tuned $k-\varepsilon$ model were also tested by comparing the numerical and experimental segregation index profiles along the channel length for cases #S2 and #S3, as presented in Figure 3.4. An excellent agreement between numerical and experimental data was obtained.

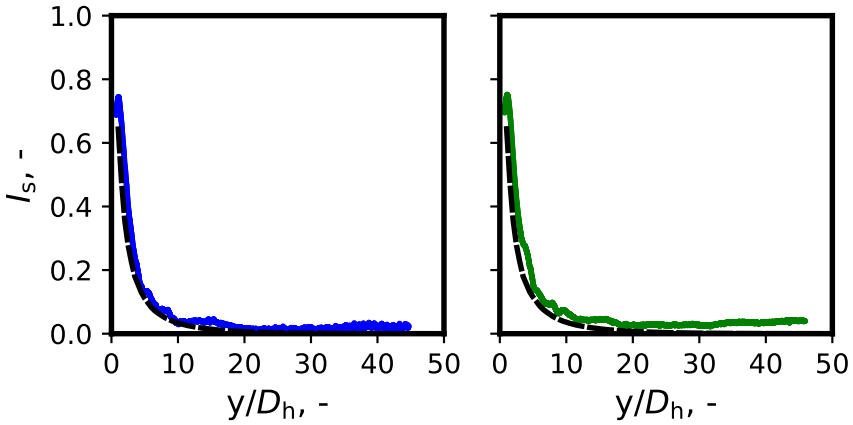

Figure 3.4 Model predictions: *Re* equal to 5350 (case #S2, *left*) and *Re* equal to 6660 (case #S3, *right*).

Pure dilution in the square cross-sectional T-mixer: unbalanced flow rates

In reaction engineering or precipitation, unbalanced flow rates can be desirable. Figure 3.5 reports experimental and numerical time average mixture fraction profiles along the channel width at normalized axial locations, y/D_h, of 1.5, 12 and 24 for case #S1 and for the unbalanced cases #S4 and #S5, see Table 3.1. Vertical bars refer to the experimental time standard deviation of the mixture fraction at a certain location in the mixing channel width. Cases #S1, #S4 and #S5 are characterized by Reynolds numbers of $\sim$ 3900, 4000 (blue food dye flow rate 2 times higher than the yellow one) and 3700 (blue food dye flow rate 3 times higher than the yellow one).

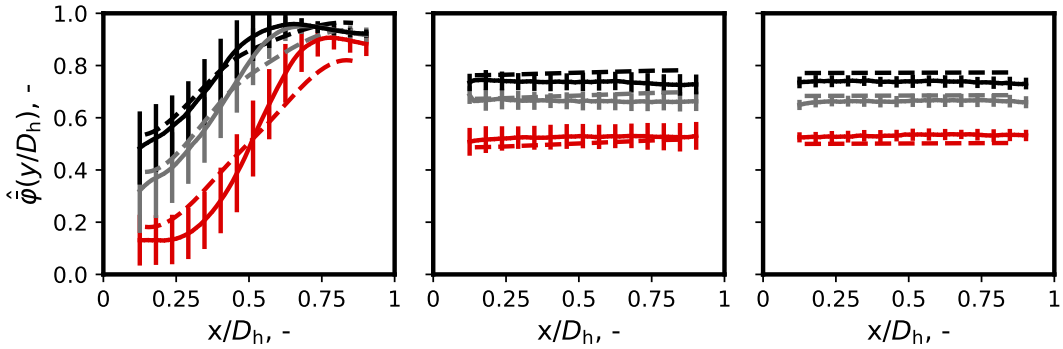

Figure 3.5 Experimental (solid lines) and numerical (dashed lines) time average mixture fraction profiles along the channel width at normalized axial locations, y/D_h, equal to 1.5 (*left*), 12 (*center*) and 24 (*right*) for cases #S1 and the unbalanced operating conditions #S4 and #S5. The vertical bars refer to the time standard deviation of the mixture fraction values.

Food dyes are segregated at $y/D_h \sim 1.5$, while a good degree of mixing is attained at $y/D_h \sim 12$. An even better homogenization degree is reached at $y/D_h \sim 24$. Mixture fraction values variation over time decrease from ~ 30 % to ~ 5 % from $y/D_h \sim 1.5$ to 24. The higher the blue dye flow rate (higher unbalanced condition), the higher the time average mixture fraction values in the left region of the mixer. This suggests that a faster mixing process already occurs in the impinging zone. Numerical predictions agree very well with experimental data. In addition, the experimental technique detects well the final expected mixture fraction values for the unbalanced cases under perfectly mixed solutions, namely 0.667 and 0.75 (Figures 3.5 *center* vs. *right*), proving the reliability of the technique. Segregation index profiles decrease faster in the unbalanced fluid flow rate cases. Segregation index values reach a value lower than 0.1 at a $y/D_h \sim$ 4.4 in the unbalanced cases, while a value $y/D_h \sim$ 5.7 is requested for the balanced flow rate case. The corresponding mixing times calculated through Eq. (3.7) are ~ 13, ~ 11 and ~ 10.8 ms for cases #S1, #S4 and #S5, respectively. Conversely, a similar mixing time of ~ 28 ms is estimated for all three cases via Eq. (3.8). Numerical segregation index profiles are in excellent agreement with experimental ones for these operative conditions. In the unbalanced flow rate conditions, the impinging region moves toward the inlet of the slowest solution. The higher the blue dye flow rate, the closer is the impinging region to the yellow dye entrance. This is in accordance with the same phenomenon observed by Fonte et al. [127] in confined imping jet mixers. Profiles of the time standard deviation of the mixture fraction decrease faster in unbalanced cases

indicating a faster homogenization of the solutions, in accordance with literature findings [107, 126].

Pure dilution in the circular cross-sectional T-mixer: equal flow rates

Figure 3.6 reports experimental (solid lines) and numerical (dashed lines) time average mixture fraction profiles for the pure dilution of food dyes, along the mixing channel width at normalized axial locations y/D_h of 1.5, 12 and 24 in the 3 mm diameter circular cross-sectional T-mixer (cases #C1, #C2 and #C3), see Table 3.2. Vertical bars refer to the time standard deviation of mixture fraction values. Numerical simulations were carried out by setting the $C_{\varepsilon 2}$ value equal to 6.54. For the sake of comparison, the segregation index computed employing the standard values of $k-\varepsilon$ model parameters is added in Figure 3.6.

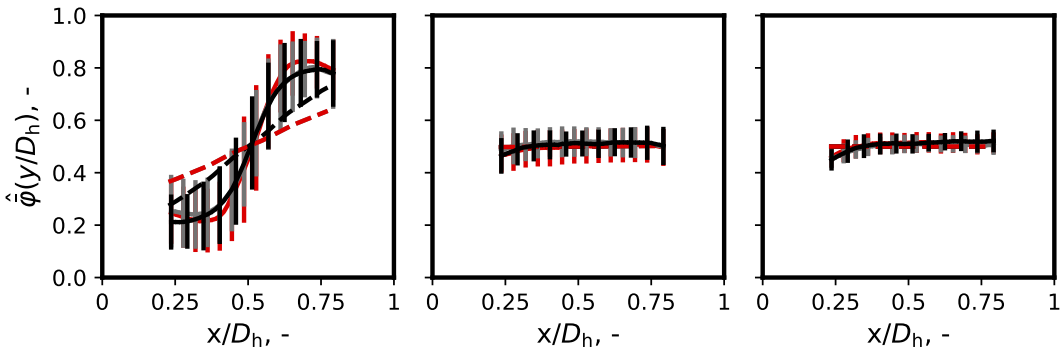

Figure 3.6 Experimental (solid lines) and numerical (dashed lines) time average mixture fraction profiles along the channel width at normalized axial locations, y/D_h, equal to 1.5 (*left*), 12 (*center*) and 24 (*right*) for cases #C1, #C2 and #C3, respectively. The vertical bars refer to the time standard deviation of the mixture fraction values.

As for the square cross-sectional T-mixer, solutions are considerably segregated at $y/D_h \sim 1.5$. Numerical segregation index profiles overestimate the mixing phenomena in the device, suggesting that a lower $C_{\varepsilon 2}$ would be more suitable for the simulation of the circular cross-sectional mixer. The homogenization further proceeds along the mixing channel length. Mixture fraction values time variation concerning their time average values are ∼20% at a y/D_h of 12, while they reduce to ∼5% at a y/D_h of 24. Segregation index profiles, Figure 3.6 - *bottom*, attain values lower than 0.1 at normalized axial locations of ∼5.9, ∼4.9 and ∼4.6, for

cases #C1, #C2 and #C3, respectively. The estimated experimental mixing times by adopting Eqs. (3.7) and (3.8) are ∼13, ∼8 and ∼6 ms, and ∼27, ∼20 and ∼16 ms, respectively. Mixing times are comparable, although slightly lower, than those obtained for the square cases, suggesting a better mixing efficiency provided by the circular mixer concerning the square one. Numerical segregation index profiles slightly overestimate mixing phenomena with respect to experimental data. However, the tuned model predicts considerably better the experimental data with respect to the standard model, see the black dotted-dashed line in Figure 3.6.

Pure dilution in the circular cross-sectional T-mixer: unbalanced flow rates

Numerical (dashed lines) and experimental (solid lines) time average mixture fraction profiles along the channel width at normalized axial locations, y/D_h of 1.5, 12 and 24, evaluated in the 3 mm diameter circular cross-sectional T-mixer for the case #C1 (Re=4000), and the unbalance cases #C4 (Re=4100) and #C5 (Re=3700), are reported in Figure 3.7. Vertical lines indicate the time standard deviation of the mixture fraction values. Figure 3.7 - *bottom* reports the numerical and experimental segregation index profile along the channel length. All numerical simulations were carried out using a $C_{\varepsilon 2}$ value equal to 6.54.

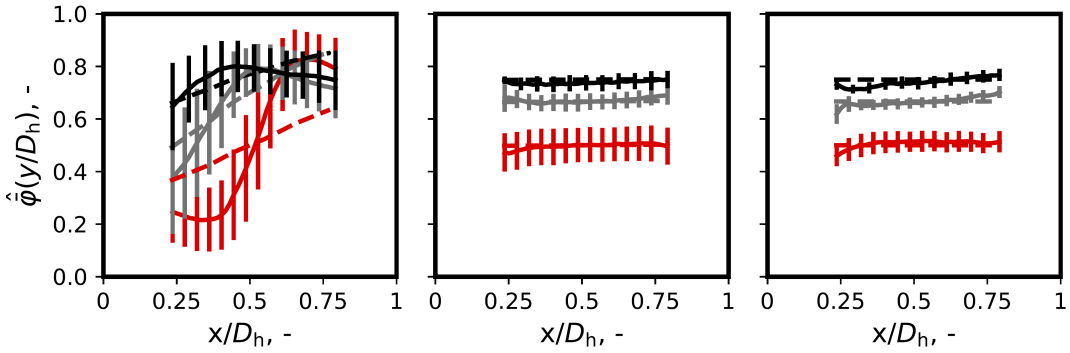

Figure 3.7 Experimental (solid lines) and numerical (dashed lines) time average mixture fraction profiles along the channel width at normalized axial locations, y/D_h, equal to 1.5 (*left*), 12 (*center*) and 24 (*right*) for cases #C1, #C4 and #C5, respectively. The vertical bars refer to the time standard deviation of the mixture fraction values.

A marked influence of the unbalanced flow rate condition can be observed. Specifically, the higher the flow rate of the blue food dye, the faster the dilution

process (less segregated profiles) at y/D_h, of 1.5, see Figure 3.7. In addition, the time standard deviation decreases faster at highly unbalanced conditions. Mixture fraction values vary less than 5% at y/D_h of 24. The mixing improvement also affects the segregation index, Figure 3.7 - *bottom*. The segregation index profiles are lower than 0.1 at normalized axial locations of ∼5.9, ∼2.8 and ∼1.44 in cases #C1, #C4 and #C5, respectively, showing a marked influence of the unbalanced flow rate condition on mixing performance in the device. The corresponding mixing times are ∼13, ∼6 and ∼4 ms by adopting Eq. (3.7). On the contrary, mixing times are always ∼28 ms in all cases using Eq. (3.8). Results highlight the limit of Eq. (3.8) in identifying the mixing times under different operating conditions. Mixing times from Eq. (3.7) are considerably lower than those observed in the square cross-sectional mixer, thus, again, marking the higher mixing efficiency of the circular mixer. Numerical predictions overestimate mixing in the device for case #C1, while they underestimate it for cases #C4 and #C5, confirming the higher mixing effectiveness attained in unbalanced conditions.

Neutralization phenomena in square and circular cross-sectional T-mixers

As discussed in the introduction, circular and square cross-sectional T-mixers are extensively employed in the precipitation field. In the following, the performance of the tuned $k-\varepsilon$ model was analysed for the description of reacting processes, namely the neutralization phenomena occurring between NaOH and HCl. Figures 3.8 and 3.9 show the numerical and experimental hydroxyl ions, OH^-, concentrations profiles in the square and circular cross-sectional T-mixers at Reynolds numbers of ∼5300 (cases #S2-N and #C2-N). OH^- profiles were evaluated along the mixing channel width at normalized axial locations of 1.5 (Figures 3.8 and 3.9 - *left*) and 12 (Figures 3.8 and 3.9 - *center*). OH^- profiles are also reported along the normalized mixing channel locations in Figures 3.8 and 3.9 - *right*.

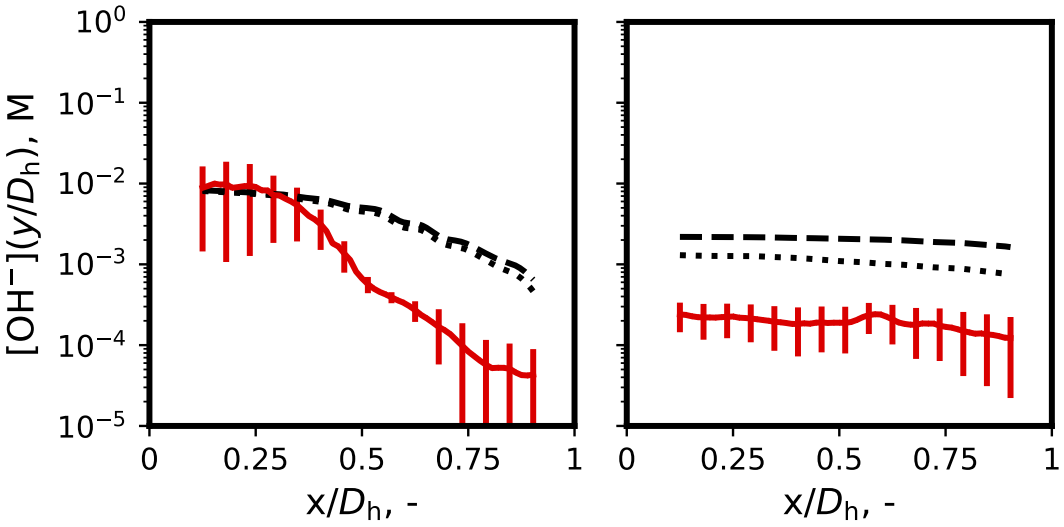

Figure 3.8 Experimental and numerical $\left[OH^-\right]$ concentration profiles along the channel width at y/D_h of 1.5 (*left*), 12 (*right*). Data refer to the investigation in the square cross-sectional T-mixer.

The standard $k-\varepsilon$ model considerably underestimates OH^- profiles. NaOH and HCl solutions are predicted to be completely segregated at a y/D_h of 1.5 and only a mild homogenization is shown at a y/D_h of 12. The tuned $k-\varepsilon$ model better describes the phenomenon in the reactor. Furthermore, by increasing the C_f parameter, even more accurate OH^- profile estimations can be obtained. Experimental data are lower than the expected final OH^- concentration. This can be attributed to (i) the logarithm law relation between pH values and OH^- concentrations that enlarges the experimental technique uncertainty when OH^- concentrations values are calculated; (ii) the experimental difficulties in preparing and obtaining precise solution concentrations and fluid flow rates. Slight flow rate imbalance or not exact concentration values can significantly influence the results.

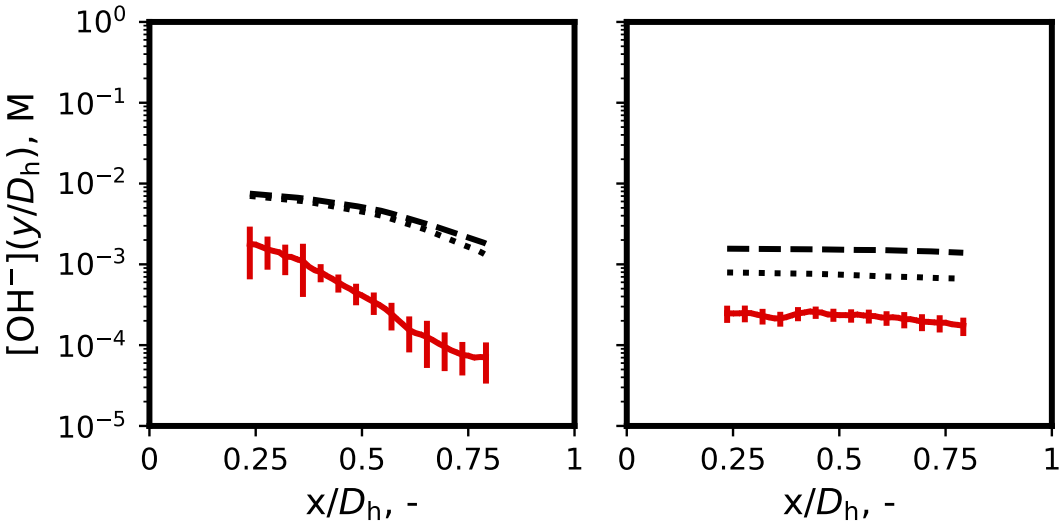

Figure 3.9 Experimental and numerical $\left[OH^-\right]$ concentration profiles along the channel width at y/D_h of 1.5 (*left*), 12 (*right*). Data refer to the investigation in the circular cross-sectional T-mixer.

Similar OH^- profile estimation is obtained also for the circular cross-shaped T-mixer, see Figure 3.9. The modified C_f model with a C_f parameter equal to 2 provides more accurate predictions concerning the standard $k-\varepsilon$ model. The modified $k-\varepsilon$ model can be then applied for fast and reliable simulations of reacting processes in T-mixers as in the case of the precipitation process of $Mg(OH)_2$ from brines [132].

3.4 Conclusions

In this study, mixing phenomena in two 3 mm hydraulic diameter T-mixers were analysed and compared. The T-mixers consisted of different cross-sectional geometries, with one featuring a square cross-section and the other possessing a circular cross-section. The aim was to assess the influence of the two geometrical designs on mixing performances. A colorimetric digital image analysis technique was adopted to capture the evolution of the pure dilution between two food dyes (blue and yellow) and the neutralization reaction between NaOH and HCl solutions. Phenomena were accurately predicted by RANS $k-\varepsilon$ simulations, after a model parameter tuning. Specifically, it was demonstrated that by increasing the $C_{\varepsilon 2}$ and C_f parameters from their standard values of 1.92 and 1 to 6.54 and 2, respectively, it was possible to effectively predict turbulence and reactive processes occurring within the T-mixers.

Consequently, the tuning of the model parameters enables the utilization of fast and less computationally demanding simulations, facilitating accurate investigations of T-mixers and their applications in reaction or precipitation processes. A slightly higher mixing degree was exhibited by the circular cross-sectional T-mixer. Mixing times, based on segregation index profiles, were ∼13±5%, ∼10.9±5% and ∼9±5% ms in the square mixer and ∼13±5%, ∼8±5% and ∼6±5% ms in the circular mixer, for Reynolds numbers of 3900, 5300, 6600, respectively. However, mixture fraction time variation suggested that longer mixing channel lengths are required to achieve a better homogenization degree between solutions, marking the need for both time statistical average and instantaneous quantities analysis to better quantify mixing in these devices. Mixing times were found to decrease when adopting unbalanced fluid flow conditions, especially in the circular cross-sectional T-mixer. In the square T mixer, mixing times slightly decreased from 13 ms (equal flow rate condition) to 11 ms (unbalanced fluid flow rate condition). Conversely, in the circular one, mixing times decrease up to three times for the balanced flow rate case. Results mark the reliability of adopting a low-cost, easy-to-use, yet accurate, experimental technique and the undemanding $k-\varepsilon$ model-based numerical simulations to accurately study mixing inside T-mixers. This can considerably reduce the cost and the computational effort of the study of such devices that would be requested by more accurate techniques, especially if different T-mixer geometries or several operating conditions must be investigated. Building upon this foundation of efficient mixing analysis, the next chapter introduces experimental tests designed specifically to investigate precipitation phenomena. These experiments will provide valuable insights into the dynamic processes governing precipitation, offering practical observations that complement theoretical models and computational simulations.

Chapter 4

Experimental Characterization of Suspensions

Some of the work described in this chapter has also been previously published in Battaglia et al. [11] (Experimental activities were done in collaboration with the University of Palermo and ETH - Zurich).

In this chapter, a comprehensive experimental study is presented on the $Mg(OH)_2$ precipitation from highly concentrated synthetic $MgCl_2$ solutions (Mg^{2+} 24 g/L). Three experimental rigs were employed. First, two circular cross-sectional T-shaped mixers, having a diameter of 2 mm (T_{2mm}) or 3 mm (T_{3mm}), were employed to tune and control the degree of reactant homogenization. Then, a Y-mixer followed by two diverging channels and a final coil of constant diameter. PSDs were accessed using the DLS technique, with ultrasound treatment and the addition of poly(acrylic acid, sodium salt) (PAA) as a dispersant. In addition, zeta potential measurements were conducted at different pH values to better investigate the tendency of particles to agglomerate.

4.1 Experimental setups

A schematic representation of the employed experimental setup is shown in Figure 4.1. $Mg(OH)_2$ precipitation was carried out employing two circular cross-sectional T-mixers with a diameter of 2 and 3 mm, and a Y-mixer followed by two diverging

channels and a final coil of constant diameter. The T-mixers were drilled in polymethyl methacrylate (PMMA) blocks and are constituted by two horizontal tracts (inlet channels) which merge into a vertical one (mixing channel). In both T-mixers, the inlet and mixing channels were of the same diameter (2 and 3 mm, respectively). The inlet channels were 10 times longer than the mixer diameter, i.e. 20 and 30 mm, while the vertical channels were twenty times longer than the mixer diameter, i.e. 40 and 60 mm, respectively. The two T-mixers were employed to investigate the effect of mixing performance in the reactors on the precipitated $Mg(OH)_2$ particles. In particular, it is expected that narrower channels offer better mixing performance with respect to larger ones [131]. Magnesium chloride ($MgCl_2$) and sodium hydroxide (NaOH) solutions were pumped using two gear pumps (Fluid-o-Tech® FG series) controlled by dedicated software developed on LabView 2015.

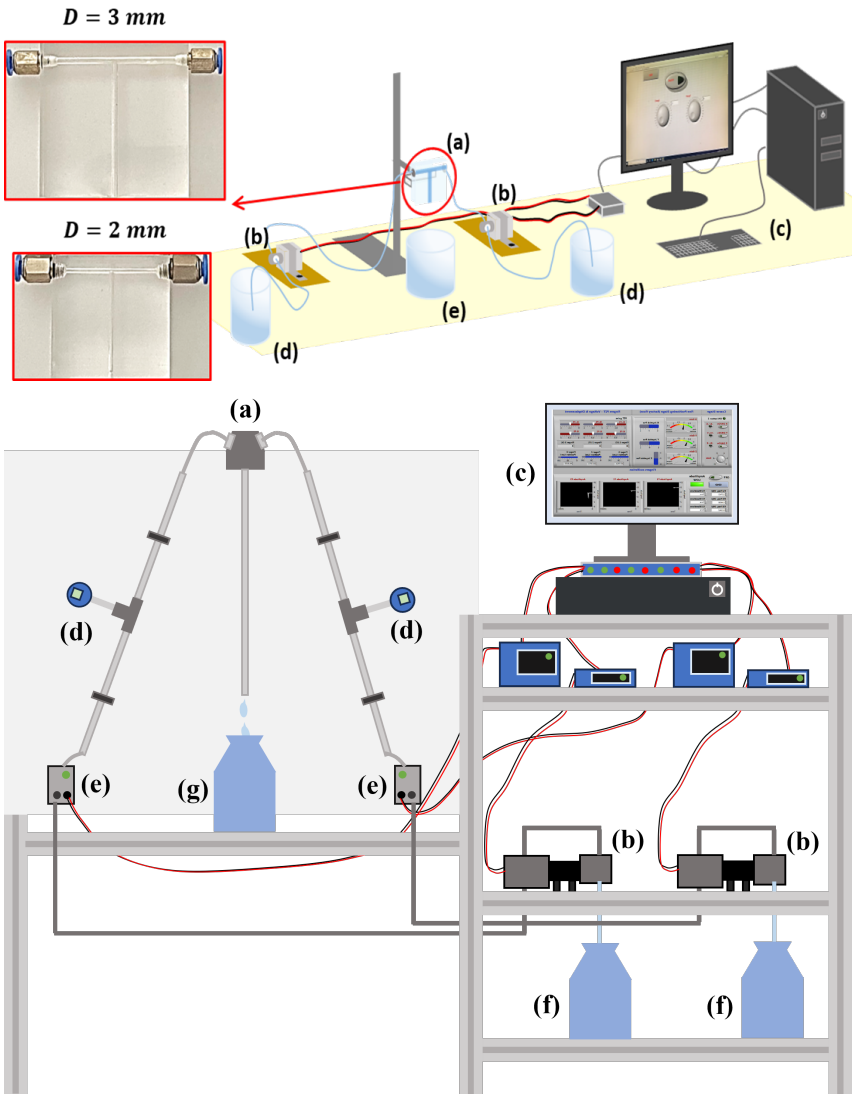

Figure 4.1 Experimental apparatuses used for the particle synthesis: T-mixer (*top*) and Y-mixer (*bottom*)

The Y-mixer setup, described by Orlewski and Mazzotti [41], consists of two arms with a diameter of 0.5 mm, a mixing channel diameter of 1 mm and a length of 3 mm. The angle between the two arms is 120°. Following the mixing channel, there are two consecutive diverging channels: the former of final diameter equal to 1.5 mm and a total length of 3.5 mm; the latter of final diameter equal to 4 mm and a total length equal to 5 mm. The setup ends with a constant diameter pipe. This fourth section was changed according to the reactant concentrations. For higher reactant concentrations (i.e., 0.125 up to 1 M), a shorter straight pipe of 40 cm was

used, whereas for lower reactant concentrations (down to 0.01 M), a coil of a total length of 10 m was used to ensure the completion of the reaction. The reactants were fed to each arm using two micro-gear pumps (mzr-11508X1, HNP Germany), assuring a pulsation-free flow. The setup was controlled using a LabView program. Two Coriolis mass flow meters (M15, Bronkhorst, The Netherlands) were used to send the set point signal to the pumps. $MgCl_2$ hexahydrate powder ($> 99.0\%$, Sigma-Aldrich) and NaOH pellets ($> 98.0\%$, Sigma-Aldrich, ACS reagent) were used to prepare the corresponding aqueous solutions at each concentration. The solutions were separately pumped through each arm and impinge in the mixing channel, where the precipitation of $Mg(OH)_2$ occurred. In Table 4.1, the operating conditions for the T- and Y- mixers are reported. The NaOH concentration obeys the stoichiometry of the reaction for all the operating conditions:

Table 4.1 Operating conditions adopted for the T- and Y-mixer

Dataset	Mixer	Operating conditions			
		Concentration $MgCl_2$ (M)	Flow rate (mL/min)	Residence time (ms)	Estimate mixing time (ms)
#1	T_{2mm}	0.125	2320	~ 3	2
		0.25	2320	~ 3	2
		0.5	2320	~ 3	2
		0.75	2320	~ 3	2
		1	2320	~ 3	2
#2	T_{2mm}	1	1602	~ 5	2.8
		1	773	~ 10	5.9
#3	T_{3mm}	1	2714	~ 9	5.6
#4	Y	0.01	835	$\sim 9 \cdot 10^3$	0.6
		0.025	835	$\sim 9 \cdot 10^3$	0.6
		0.05	835	$\sim 9 \cdot 10^3$	0.6
		0.125	835	$\sim 3.6 \cdot 10^2$	0.6
		0.5	835	$\sim 3.6 \cdot 10^2$	0.6
		1	835	$\sim 3.6 \cdot 10^2$	0.6

Eight tests were conducted in the T-mixers to allow three effects to be studied: (i) the effect of the concentration (dataset #1), (ii) the effect of the flow rate (dataset #2), and (iii) the effect of a change in T-mixer diameter (dataset #3). Concerning the effect of the concentration, the chosen flow rate was 1160 mL/min for each inlet solution to have a total flow rate of 2320 mL/min in the mixing channel, as shown in Table 4.1. For a mean fluid velocity of 12.3 m/s, corresponding to the aforementioned flow rate, the effect of the initial $MgCl_2$ and NaOH concentrations on the produced $Mg(OH)_2$ particles was investigated; $MgCl_2$ solutions ranged from 0.125M to 1M (to mimic the magnesium content of real brines) and stoichiometric NaOH solutions were used, as reported in Table 4.1. The effect of reactant concentrations on $Mg(OH)_2$ particle sizes formed in the mixing channel was investigated at a Reynolds number of 27251. The effect of the flow rate was studied by keeping the concentration constant and equal to the highest value ($MgCl_2$ 1 M, NaOH 2 M). Taking case 5 of dataset #1 as a reference, the flow rate was decreased by 30% for case 1 of dataset #2 and 67% for case 2 of the same dataset resulting in different mixing times (Table 4.1). Using the T_{3mm}-mixer, the effect of changing geometry was studied. In the case of the Y-mixer (dataset #4), the $MgCl_2$ concentration range investigated initially in dataset #1 was extended towards smaller concentration levels. A sample of the suspension exiting the mixing channel was collected, and the PSDs were measured using the DLS (Zetasizer Nano ZS, Malvern Instruments, UK) technique. For this, the following procedure was followed: (i) the suspension was diluted, if necessary, to ensure that the same solid mass of 0.3 g/L per unit suspension volume was reached, (ii) an anti-agglomeration agent (poly-acrylic acid, sodium salt) was added (4.9 g/kg) to suppress agglomeration and, in the end, (iii) the sample was left in an ultrasound bath (Elmasonic S 40 (H), Singen, Germany) for 5 min. The protocol makes it possible not only to neglect agglomeration but also to stabilize suspension by arresting possible changes in PSDs [132]. From the experimentally measured PSD, moments were calculated according to the following definition:

$$m_j = \int_0^\infty L^j f(L) \mathrm{d}L \tag{4.1}$$

where L is the particle size and $f(L)$ is the PSD. Correspondingly, the moment ratios d_{ij} are defined as:

$$\mathrm{d}_{ij} = \frac{m_i}{m_j} \tag{4.2}$$

Since these characteristic sizes (such as $d_{10}, d_{21}, d_{32}, d_{43}$) are calculated from integral properties (i.e., the moments of the PSD) tracing their evolution means tracing the evolution of the whole PSD. Therefore, although all characteristic sizes are monitored, we chose to focus the discussion only on d_{10} for the sake of discussion. This choice is also supported by the observation that the distributions that the DLS can provide are generally poorly poly-disperse. It means, therefore, that the characteristic sizes always exhibit the same qualitative trend, and the absolute value of the dimensions increases as the monitored size increases (i.e., $d_{10} < d_{21} < d_{32} < d_{43}$).

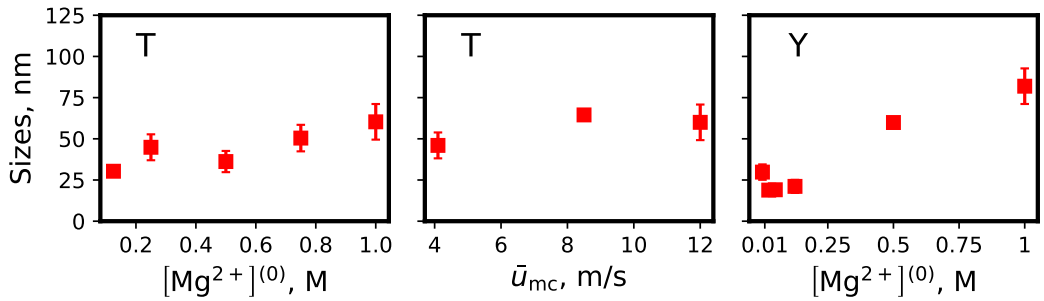

Figure 4.2 Experimental datasets: #1 (*left*), #2 (*center*), #4 (*right*)

The measured d_{10} shows an increase in particle size as the initial reactant concentration is increased (dataset #1). An approximately linear trend is observed. Figure 4.2 - *center* shows that for a mean velocity (i.e., flow rate) range in the mixing channel between 4 and 12 m/s, no significant changes in the mean particle size are detected as well as for the change in the geometry. Finally, the Y-mixer showed an increasing monotonic trend in terms of d_{10} in the same range of concentrations of dataset #1 whereas a minimum was detected at lower concentrations. Experiments at lower concentrations in the T-mixer were also carried out and showed good agreement with simulations. However, the results from these experiments are not reported in this study due to the presence of experimental uncertainty that is difficult to quantify. This uncertainty is primarily related to the impossibility of controlling where the end of the reaction occurs, particularly at low concentrations. In this scenario, there is a possibility of some unconsumed supersaturation remaining at the T-mixer outlet, which could lead to further particle evolution within the collection flask. While it is reasonable to assume that this variation is not significant, as the supersaturation at the outlet will have been consumed in large amounts and further gets diluted in the collection flask, it remains challenging to precisely estimate the uncertainty in

particle sizes. In contrast, the Y-mixer experiments benefited from the possibility of guaranteeing adequate residence times by extending the final section of the mixer. Unfortunately, a similar extension was not feasible in the T-mixer, making it difficult to determine conclusively whether the reaction was completed inside the T-mixer or within the collection flask.

4.2 Zeta potential measurements

To better understand the stability of $Mg(OH)_2$ colloids (the ability to stay in the colloidal form without particle agglomeration through flocculation [133]) and its implications on the obtained PSD, zeta potential measurements were conducted analysing $Mg(OH)_2$ suspensions produced: (i) after 2 h from the precipitation for case 1 - dataset #1 and case 2 - dataset #2 without PAA; (ii) after 1 month of ageing for suspensions of case 2 - dataset #2 without PAA; (iii) after 2 h from the precipitation for case 2 - dataset #2 with PAA. The 2 h samples were analysed using a Malvern® Zetasizer Nano ZSP (analysis conducted at the Advanced Technologies Network Center of the University of Palermo), while the 1 month samples were analysed using a Malvern® Zetasizer Nano ZS90 (analysis conducted at Politecnico di Torino). All samples were diluted to a $Mg(OH)_2$ concentration of 0.3 g/L and drops of 1 M NaOH solution were added to adjust the suspensions' pH to the desired one. It is worth mentioning that the value obtained for each measurement is the result of at least 12 repeated internal measurements of the Zetasizer, which eventually returns an average value with a standard deviation. Moreover, each experiment was repeated at least twice for reproducibility purposes. This allows us to estimate the error bars reported in the results, by statistically combining the dispersion between different trials (reproducibility error) and the measurement error, provided for each individual trial by the device employed (Malvern Zetasizer). The stability of $Mg(OH)_2$ suspensions was also investigated over time performing the analysis (i) after 2 h and (ii) after 1 month of ageing from the precipitation. Zeta-potential depends on the particle properties, the suspension conditions (e.g. pH), and the theoretical model applied, e.g. the Smoluchowski approximation employed here to derive Zeta-potential values from the electrophoretic mobility of particles [134].

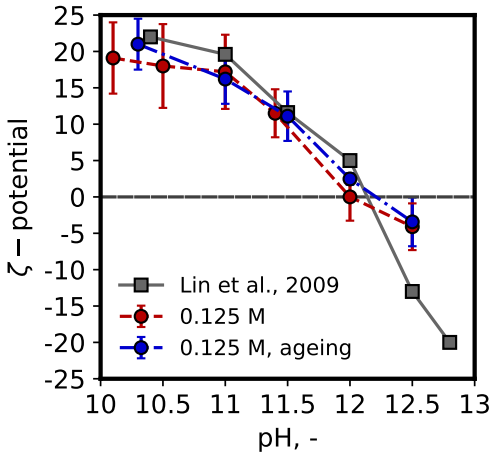

Figure 4.3 Zeta potential trend for two samples (not- and aged) compared with the literature trend

Figure 4.3 presents Zeta-potential values measured for case 2 of dataset #2 (see Table 4.1) downstream the precipitation (red dashed line) and after 1 month (blue dotted-dash line) from precipitation for suspension pH ranging from 10 to 13. The experimental data collected in this study was compared with those presented by Lin and Wang [135]. The latter authors employed an electro-acoustic technique, while the data reported here were obtained using Malvern® Zetasizers, which are based on the electrophoretic mobility technique, i.e. on measuring the limiting velocity of the particles in an electric field. At solution pH between 10 and 11, a good agreement is observed between Lin and Wang [135] data and Zeta-potential values. Aged samples showed an even better agreement with the measurements of Lin and Wang [135]. Specifically, Zeta-potential values measured without ageing were found to vary from $\sim$19 mV to $\sim$18 mV as pH values varied from 10 to 11, while Zeta-potential values reported by Lin and Wang [135] and those measured for the aged samples varied from $\sim$22 mV to $\sim$20 mV. Some difficulties were encountered for measurements in high pH suspensions due to their high conductivity values so pH values higher than 12.5 could not be investigated. Lin and Wang [135], however, reported Zeta-potential values of $\sim$-15 mV at pH $\sim$12.5 and $\sim$-20 mV at pH$\sim$13. The isoelectric point (the point of zero Zeta-potential, where colloids have the largest tendency to agglomerate) of $Mg(OH)_2$ particles is detected at a pH value of $\sim$12 for both samples, in good agreement with Lin and Wang [135] and with values reported in literature [136–138]. Zeta-potential values measured for samples with and without ageing show that $Mg(OH)_2$ suspensions are characterized by the same stability characteristics over

time and similar Zeta potential values. Therefore, no influence on the Zeta potential value can be observed at different mixing conditions. Figure 4.3 shows that the Zeta-potential of the Mg(OH)2 particles lies in the range of $\pm$30 mV, which represents a zeta potential region where particles are not stable and tend to agglomerate rather than staying apart [134]. Specifically, in the absence of PAA, $Mg(OH)_2$ particles agglomerate due to their low zeta potential values. On the other hand, the presence of PAA stabilizes the $Mg(OH)_2$ suspension [133, 139]. Specifically, the addition of the PAA causes an increase of the Zeta-potential that reaches values of 35–40, in absolute value, away from the $\pm$30 mV unstable Zeta-potential region, which is the expected effect of PAA surrounding the particles and modifying their Zeta-potential and agglomeration tendency. The thermodynamically stable coiled structure of PA-can entrap $Mg(OH)_2$ nanoparticles preventing their agglomeration [133].

4.3 SEM analysis

To investigate whether and how particles' morphology can be affected by precipitation conditions and post-treatment handling, $Mg(OH)_2$ particles morphology was analysed via Scanning Electron Microscopy (SEM FEI Quanta 200 FEG). Morphologies were compared for case 1 - dataset #1 and case 2 - dataset #2 after performing two different particle preparation processes aiming at removing non-$Mg(OH)_2$ salts from the sample:

- $Mg(OH)_2$ suspensions were filtered by using a Büchner system and a vacuum pump; the cake was washed to remove the reaction-produced NaCl that remained trapped in the wet cake, then dried for 24 h in an oven at 120 °C and finally crashed by mortar & pestle
- 7 mL of $Mg(OH)_2$ suspension was added to 700 mL distilled water in the HydroMU 2000 beaker; 30 drops of PAA were added and 5 min of ultrasound treatment was applied; a drop of the diluted suspension was then withdrawn close to the impeller, positioned on an SEM stub and dried in a vacuum vessel for 48 h.

Having explored the experimental procedures used for the production and characterization of globular $Mg(OH)_2$ nanoparticles, as evidenced by the SEM images in

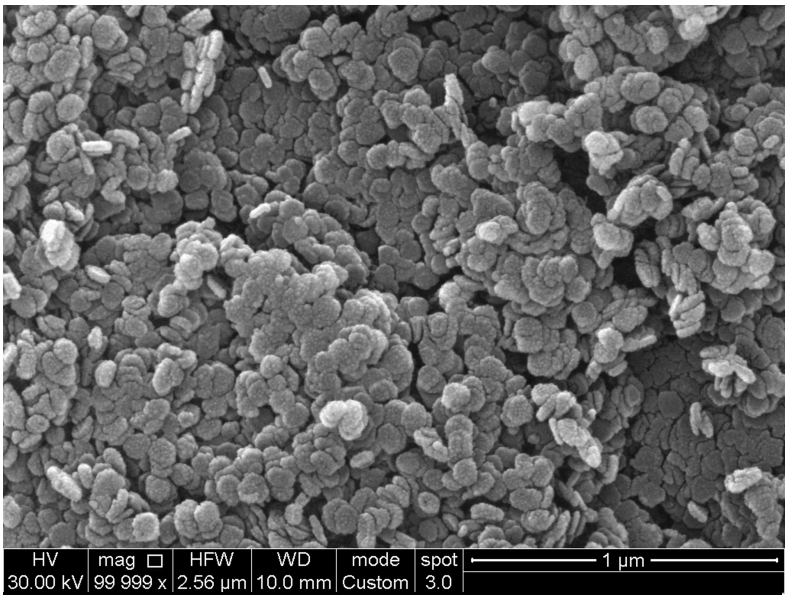

(a) T-mixer

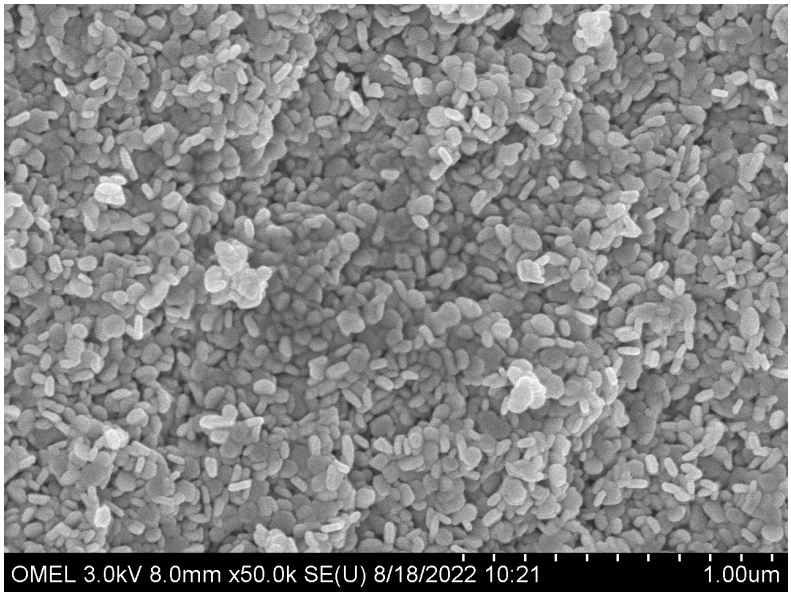

(b) Y-mixer

Figure 4.4 T- and Y- mixer SEM analysis

Figure 4.4, we now shift our focus to modelling strategies and methodology in the subsequent chapter. The detailed experimental insights gained from these procedures provide a solid foundation for developing effective modelling approaches aimed at understanding the behaviour and properties of such nanometric structures. In the upcoming chapter, we delve into the theoretical frameworks and computational methods employed to simulate and analyze the formation, stability, and interactions of $Mg(OH)_2$ nanoparticles. This transition allows us to bridge experimental observations with theoretical modelling, offering a comprehensive exploration of $Mg(OH)_2$ nanoparticles from both empirical and computational perspectives.

Chapter 5

Modelling Strategies and Methodology

Some of the work described in this chapter has also been previously published in Raponi et al. [132] and Raponi et al. [140].

In this chapter, we aim to develop a comprehensive model to infer kinetic parameters for primary nucleation, molecular growth, and bridge strength of aggregates. For the sake of clarity, throughout all sections, the following terminology will be used: (i) 'primary particles' to refer to single crystals formed by primary nucleation and enlarged by growth (ii) aggregation to refer to the formation of primary particles clusters (or secondary particles), where primary particles stick together forming stable bridges due to supersaturation depletion (iii) agglomeration to refer to the formation of groups of primary particles and their clusters, which come close each other and hold that configuration due to weak interaction forces.

5.1 Computational Modelling

A simplified mono-dimensional model (1D) has been developed and implemented. In this model, several aspects are integrated to accurately reproduce the real physical behaviour presented by the experimental evidence: (i) chemical reaction, (ii) solution non-ideality (activity coefficients), (iii) particle size evolution, and (iv) micro-mixing. The 1D model aims to describe static mixers (T_{2mm}, T_{3mm} and Y), assumed to behave

like a Plug Flow Reactor (PFR), but still incorporating information concerning the turbulent fields to account for micro-mixing. It is then employed to determine the $Mg(OH)_2$ precipitation kinetics. In Figure 5.1 the flow chart describing the code implementing the model is presented.

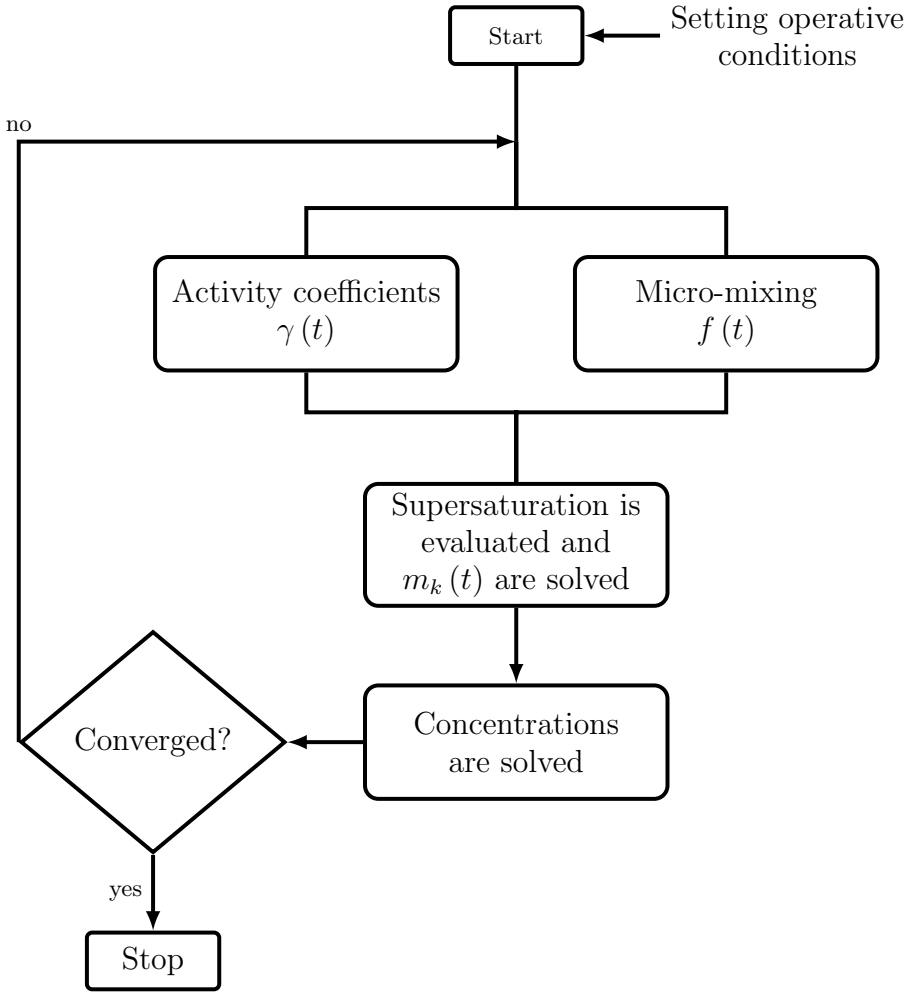

Figure 5.1 Model flowchart

Initially, ion concentrations, Mg^{2+} and OH^- are set equal to the experimental values at the inlet streams (see Table 4.1). The moments of the PSD, of order ranging from 0 to 2N-1 (where N is the number of nodes used in the QMOM [102]), are set equal to zero because no precipitated solid is present at the inlets. Given these initial conditions, the algorithm evaluates the activity coefficients to be used in the supersaturation expression and, in parallel, the truly available concentration of Mg^{+2} and OH^- which can precipitate due to the chemical reaction between $MgCl_2$ and

NaOH. Therefore, supersaturation is evaluated. This variable within the model is one of the most important because it represents the driving force, of all the phenomena involved, namely primary nucleation, molecular growth, and aggregation. As mentioned, the PBM is solved in terms of the moments of the PSD by using the QMOM. Once the PBM is solved for the current time step, moments (and their rates) are calculated and used to calculate the precipitated amount of ions from the solution in the solid lattice. Calculations proceed until the simulation length (input data) is reached. The mono-dimensional model is implemented in MatLab® and the ODE integration algorithm used is *ode15s* (*ode45* was also used to check whether the same solution was obtained). This latter was chosen for numerical stability reasons, being the problem stiff. As mixing and reaction times are fast, many physical quantities (such as the particle number, for instance) increase rapidly by several orders of magnitude in a very short time. It is important to emphasize that the mono-dimensional framework is used to identify precipitation kinetics upon comparison with experimental PSDs through a multivariate constrained optimization. One can therefore understand the need to use a fast-running model that can provide a rapid response, as many function evaluations might be necessary. In addition to this fundamental study, the choice of an easy-to-tune model is reinforced by the final application: the design of a prototype for magnesium hydroxide precipitation at the pilot scale. Therefore, the model can be employed to infer precipitation kinetics. Once the order of magnitude is known, a higher dimensional model (e.g., 3D model) can be used to assess the influence of operating conditions (e.g., concentration, flow rate) and process parameters (e.g., reaction volume) on the PSDs. At the industrial level, specific granulometric characteristics are required depending on the field of application. Having a simplified, computationally cheap tool for numerical investigations allows one to change the input parameters until the desired commercial target is obtained. Once the influence of the parameters on the PSDs has been assessed, a computationally less cheap but physically more complex model can be used for a fine-tuning study. This more complex model can be based for example on the idea of solving the PBM (with QMOM) directly within the CFD code. With the latter, the influence of flow field gradients (e.g., radial dispersion) can be studied. Once the turbulence is solved, this model can be used in two steps: (i) to assess the mixing of the reactants and thus solve the supersaturation field and (ii) to solve PBM. Performing these two steps consequentially will optimize computing resources. The supersaturation distribution makes it possible to assess, for example,

whether radial dispersion is pronounced. If it were, the 1D model could be used for a first qualitative study but it would certainly lead to a quantitative error and the more detailed model should be employed. Moreover, the associated computational costs are reported. The used computational power refers to a CPU clock frequency of 2300 MHz with 65 Gb RAM. The 1D model is run on a single core whereas the more complex model is on multi-cores. The 1D model has an execution time of a few seconds, whereas the supersaturation solution for the more complex solver requires about 9500 times as much (i.e., about 8 h). The solution of the PBM within the CFD code reaches some days of computing.

Computational Fluid Dynamics Integration

Since many of the phenomena involved are related to both the turbulent energy dissipation rate (TDR), ε, and the turbulent kinetic energy (TKE), k, an accurate description of these quantities is required. Various valid approaches can be used to obtain ε values, such as calculating them using experimental pressure drops (if known) or through CFD simulations. Table 5.1 provides both the boundary conditions used for the CFD simulation settings and the initial conditions for all the solved fields.

Table 5.1 Boundary Conditions and Initial Conditions

	Inlet	**Outlet**	**Walls**	**Initial Conditions**
TKE, k	$\frac{3}{2}\left(Iu_{\text{mag}}\right)$	Neumann condition	Scalable wall-function	$\frac{3}{2}\left(Iu_{\text{mag}}\right)$
TDR, ε	$\frac{C_\mu^{0.75}k^{1.5}}{L_{\text{s}}}$	Neumann condition	Scalable wall-function	$\frac{C_\mu^{0.75}k^{1.5}}{L_{\text{s}}}$
Turbulent viscosity	$C_\mu\frac{k^2}{\varepsilon}$	Neumann condition	Scalable wall-function	0
Velocity (m/s)	$u_{\text{mag}}^{(\text{inl})}$	Neumann condition	No slip	$(0,0,0)$

Where the Neumann condition refers to the gradient of the solved property equal to zero, no-slip refers to the velocity equality between fluid and wall, and

the wall functions for the near-wall treatment can be found in the literature [141]. Simulations were run in OpenFOAM exploiting the *twoLiquidMixingFoam* solver within the RANS approach, computed exploiting the 'PIMPLE' coupling algorithm. Scalable wall functions (already implemented in OpenFOAM) were used for the near-wall treatment, as suggested in the literature [128]. A grid convergence study was performed, resulting in a final grid of $\sim$ 130000 cells.

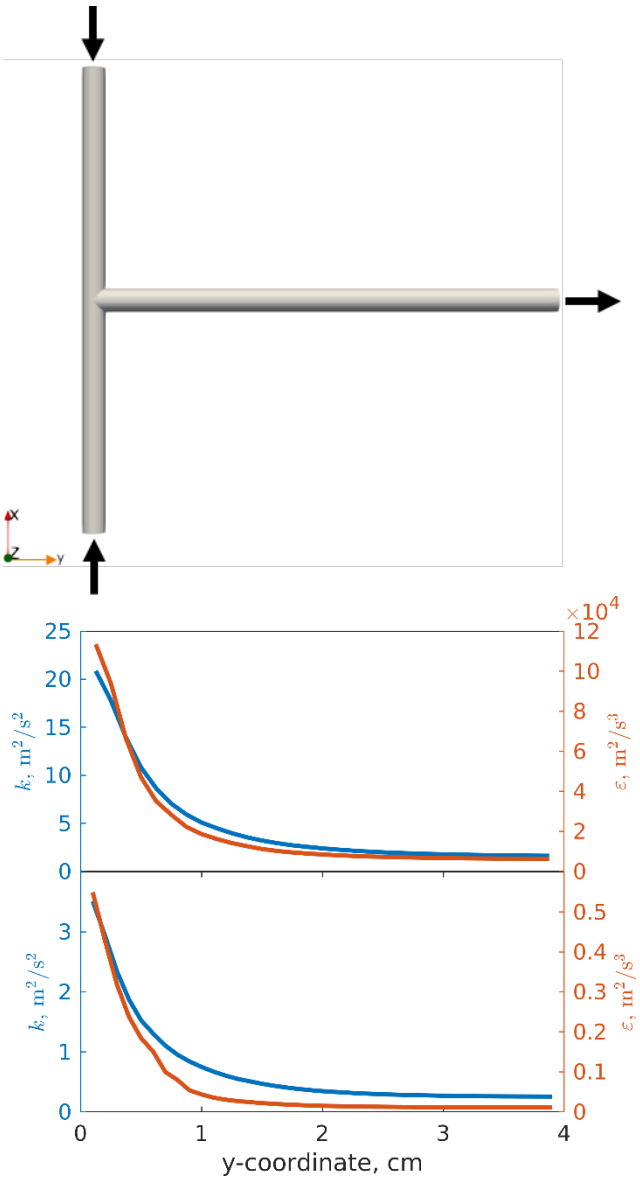

Figure 5.2 T-mixer geometry and spatial profiles

As a result, spatial profiles for the properties of interest were extracted from CFD simulations and employed in the 1D model, as shown in Figure 5.2. The trend reported is in accordance with the known literature. T-mixers develop massive turbulence as described both through experimental tests [142] and DNS [40]. NaOH and $MgCl_2$ solutions (with slightly different solution densities and viscosity within the CFD simulations) come from the two inlets impinging along a plane where most of the turbulent kinetic energy is transported for convection and dissipated. Keep going along the y-coordinate, namely approaching the outlet, since most of the fluid energy is dissipated, these profiles tend to an asymptotic value. Analogous behaviour was found for the other geometry (Y-mixer) with similar operating conditions [41]. Figure 5.2 reports the evolution of turbulent profiles for the flow rate of dataset #1 and case 2 of dataset #2. It should be noted that the flow rate of case 2 of dataset #2 is one-third of the flow rate of dataset #1. Turbulent properties, however, scale one order of magnitude. An analogous trend can be found when the T- and Y-mixer turbulent profiles are compared as shown in Figure 5.3.

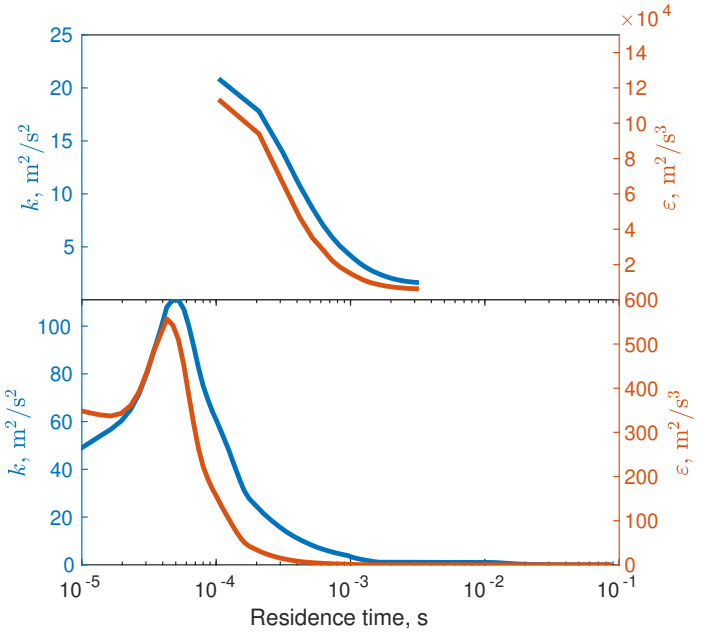

Figure 5.3 The averaged $k-\varepsilon$ profiles extracted from CFD simulations are shown for the T-mixer setup (top) and the Y-mixer setup (bottom).

The turbulent properties in the T-mixer are one order of magnitude lower than those in the Y-mixer. Indeed, this justifies that the dissipation of variance is slower in the T-mixer than in the Y-mixer. Note that the flow and turbulent fields affect both the molecular processes (i.e., nucleation and growth) as well as the secondary process (i.e., aggregation) considered here. Thus, by comparing different systems, one can investigate the effect of the fluid flow and compare the T-mixer with the Y-mixer.

Micro-mixing and Chemical reaction

Our study employs a micro-mixing model to account for the molecular-scale mixing of ions required for the formation of $Mg(OH)_2$. In very fast processes, micro-mixing can become the rate-determining step. As reported in Appendix B.2, accurate predictions of both the trend and experimental data values cannot be achieved without accounting for the micro-mixing. When the micro-mixing model is turned off, predictions for the mean particle sizes are significantly inaccurate and unphysical. Therefore, neglecting micro-mixing would result in an inaccurate description of the experimental data. Micro-mixing is described via the variance of a non-reacting scalar, the mixture fraction, obeying the following ordinary differential equation:

$$\frac{\mathrm{d}\left(\bar{u}\bar{\alpha}'^2\right)}{\mathrm{d}y} = -\frac{C_\phi}{2}\frac{\varepsilon(y)}{k(y)}\bar{\alpha}'^2 \tag{5.1}$$

where y is the axial coordinate of the T-mixers and $\bar{u}$ is the average fluid velocity in the axial direction, C_ϕ was set equal to 2 as reported by Marchisio and Fox [53].

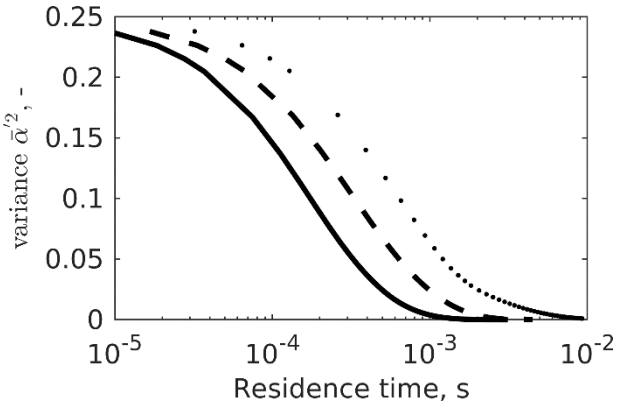

Figure 5.4 Variance evolution was obtained using the turbulent dissipation rate and kinetic energy from CFD simulations as a function of the residence time (s) for three flow rates (case 5 of dataset #1 and cases of dataset #2). The solid line refers to case 5 of dataset #1, the dashed line refers to case 1 of dataset #2 and the dotted line refers to case 2 of dataset #2

The profiles in Figure 5.4 are obtained by solving Eq. (5.1) by using the turbulent profiles extracted from CFD simulations to estimate the mixing time proportional to the $k-\varepsilon$ ratio. However, an empirical value for the mixing time, such as the one reported in Table 4.1, could also be used. In that case, a similar result would have been obtained. The variance evolution, besides the goal for what is used, has important physical implications that can be analyzed; it tells how fast two reactants can reach the Batchelor (or purely diffusive) scale and, therefore, react. Hence, it is assumed that in the T-mixers the solution starts with a perfectly micro-segregated condition $\left(\bar{\alpha}'^2 = 0.25\right)$ for which ions are perfectly macro-mixed $(\bar{\alpha} = 0.5)$ but cannot precipitate (neither nucleate nor grow) because not available at the molecular level. To compare variance profiles at different flow rates (Figure 5.4), the generic y-coordinate within the mixing channel was divided by the velocity corresponding to the investigated flow rate (Table 4.1) to obtain the profiles as a function of the residence time. All the variance profiles suggest that ions available for the precipitation are micro-mixed within a short period and this is in accordance with the T-mixers theory [40]. One can note that the time at which variance nulls (Figure 5.4) is equal to the one experimentally estimated (Table 4.1). The more the flow rate decreases, the more turbulence decreases (Figure 5.2). Therefore, reagents take longer to micro-mix resulting in longer mixing times. The variance decay is used together with the presumed beta probability density function (β-PDF) approach [53] to evaluate the actual ions concentration available for building up supersaturation, un-

der the assumption of an infinitely fast chemical reaction. Additionally, a comparison between the T- and Y-mixer variance evolution is reported in Figure 5.5:

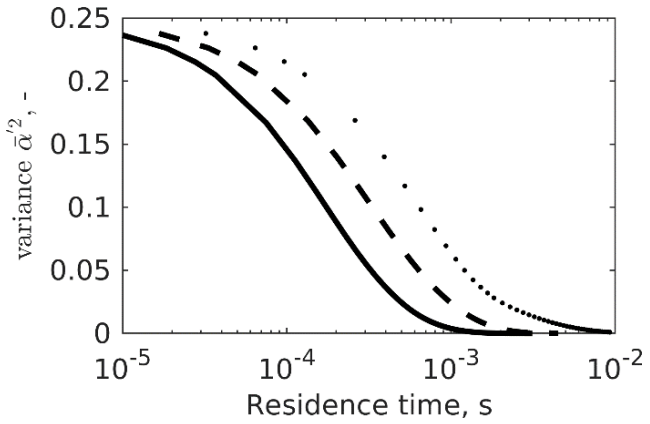

Figure 5.5 Mixture fraction variance evolution as a function of the residence time for the T- and Y- mixers setups obtained solving Eq. (5.1). Dashed line refers to the T-mixer and solid line refers to the Y-mixer.

In Figure 5.5, the mixture fraction variance evolution is shown for the T- and Y- mixers, and a characteristic time for its dissipation can be identified. One can see that in the Y-mixer, the mixing efficiency is higher than in the T-mixer. In fact, Battaglia et al. [11] empirically estimated that for the T-mixer (referring to a velocity in the mixing channel of 12.3 m/s), the characteristic mixing time was about 2 ms (using the expression provided by Schikarski et al. [40], namely Eq. (6) in their paper) which is one order of magnitude higher than that of the Y-mixer (assuming 10^{-4} s to be the time when variance becomes practically zero).

Supersaturation and Activity Coefficient

The computational model accounts for (i) primary nucleation (homogeneous and heterogeneous), (ii) molecular growth, and (iii) aggregation (hydro-dynamic and Brownian). In this regard, a PBE was solved considering all these phenomena, as source terms in the evolution equations for the moments of the PSD. Kinetics parameters related to the source terms were tuned to fit experimentally measured PSDs. The driving force in the precipitation processes is represented by the excess of ions in the liquid compared to the thermodynamic solubility $\left(k_{\mathrm{sp}}\right)$ of its solid. Therefore, a dimensionless variable, the supersaturation ratio, or shortly supersaturation, is used

to quantify this driving force throughout the process. For magnesium hydroxide, according to Yuan et al. [33], supersaturation can be defined as:

$$S = \frac{\gamma_{\pm}^{3}\left(\bar{c}_{Mg^{2+}}\bar{c}_{OH^{-}}^{2}\right)}{k_{sp}} - 1 \tag{5.2}$$

$$k_{sp} = a_{Mg^{2+},eq}\, a_{OH^{-},eq}^{2} \tag{5.3}$$

Here $\bar{c}_{Mg^{2+}}$ and $\bar{c}_{OH^{-}}$ are computed through the β-PDF approach. It is important to note that these two concentrations are different from the total Mg^{2+} and OH^{-} concentrations that enter the system. These two concentrations are a fraction of the total concentrations entering the system. This fraction initially increases as the system evolves toward a perfect micro-mixing condition and then decreases due to precipitation. $\gamma_{\pm}$ is the ions activity coefficient [143]. Details of the coefficients and equations used for the activity coefficient model are given in Appendix B.1

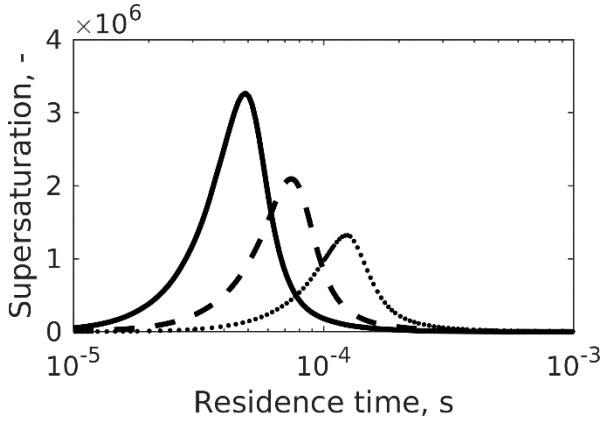

Figure 5.6 The supersaturation profile reconstructed from the ion concentrations calculated through the model for different flow rates as a function of the residence time (s) for three flow rates (case 5 of dataset #1 and cases of dataset #2). The solid line refers to case 5 of dataset #1, the dashed line refers to case 1 of dataset #2 and the dotted line refers to case 2 of dataset #2

The trend underlines that competitive phenomena occur. At the beginning of the process, supersaturation starts increasing due to ions' molecular contact (micro-segregation decreases due to high turbulence), and the driving force for precipitation increases. Since supersaturation increases, nucleation and molecular growth occur, resulting in the formation of the precipitate with consequent ions depletion from the liquid phase. The flow rate effect, already introduced with variance profiles,

is reinforced by explaining the influence on the supersaturation (Figure 5.6). By changing the flow rate and consequently the turbulence, mixing gets worse and the times within which supersaturation occurs increase (profiles shift to the right, as well as variance). In addition, the maximum local supersaturation value decreases (from solid to dotted line) as the flow rate decreases. Worse mixing produces a lower concentration of reactants available at the molecular scale to react. Lastly, it is necessary to underline the importance of activity coefficients, whose usage is needed to correct the effectively "active" concentration of ions in solution. When ion concentration increases, mobility resistance of ions themselves can arise. Counter-ions can form a cloud around co-ions which leads to a shield effect able to reduce their mobility and electrostatic interaction. To consider this effect and to correct analytical concentrations, Bromley activity coefficients for multi-component solutions were used [143]. Bromley's theory is semi-empirical, based on ions' electrostatic interactions, and ions were considered: Mg^{+2}-OH^{-}, Mg^{+2}-Cl^{-}, Na^{+}-OH^{-}, Na^{+}-Cl^{-}. Bromley's theory neglects co-ions interactions which may be relevant in some cases. However, since this theory was developed using concentrated seawater as a test solution, Bromley's theory can be used for magnesium hydroxide. This model was implemented for the multi-component solution because parameters are available in the literature and each of the presented operative conditions is below 6 M in terms of ionic strength (upper validity limit for Bromley's theory).

5.2 Kinetics Parameters Identification and Optimization

Primary nucleation (both homogeneous and heterogeneous) was described with the Volmer-Weber expression (Eq. (2.37)). The molecular growth rate was described through a power-law expression (Eq. (2.38)). The aggregation rate includes both the Brownian and turbulent contribution (Eqs. (2.45), (2.47)). Moreover, since not all impacts lead to aggregation, Smoluchoski's collisions theory has been corrected [89] using an aggregation efficiency or sticking probability (Eq. (2.44)). The aggregation efficiency is greater than zero (i.e., two particles can aggregate) only if the cementation time is of the same order of magnitude as the interaction time or lower. In other words, two particles could stick together only if the time required for the stable bridge to be formed is at most the one between two rupture events. A key

point to consider is the sensitivity of aggregation to the values of the TDR, ε [112]. This is because the turbulent contribution to the aggregation rate is directly related to the ε value (Eq. (2.47)). Additionally, ε is used to calculate both the interaction time (Eq. (2.52)) and the cementing time (Eq. (2.53)), and the ratio of these values allows the aggregation efficiency to be determined. A sensitivity analysis for constant ε values is provided in Appendix B.3 and it proves that it is important to carefully evaluate the ε value when modelling the aggregation process. The above equations are solved in the PBM using the QMOM [102, 103] approach:

$$\frac{\mathrm{d}\left(\bar{u}m_j\right)}{\mathrm{d}y} = J_k L_c^k + k\sum_{i=1}^{N} G L_i^{k-1} w_i + \frac{1}{2}\sum_{i=1}^{N} w_i \sum_{j=1}^{N} w_j \beta_{agg}(L_i^3 + L_j^3)^{\frac{k}{3}} - \sum_{i=1}^{N} w_i L_i^k \sum_{j=1}^{N} w_j \tag{5.4}$$

Here, L_c is the critical size (1 nm) of a stable nucleus, whereas $\bar{B}_j$ and $\bar{D}_j$ model the birth and the death term linked to a net aggregation rate. In the present work, 3 quadrature nodes (or, consequently, 6 moments) were used. Ultimately, the PBM is closed by resorting to a mass balance for ions that, upon reacting, disappear from the liquid phase to form the solid:

$$\frac{\mathrm{d}\left[\mathrm{Mg}^{2+}\right]}{\mathrm{d}y} = -\frac{\rho_\mathrm{c} k_\mathrm{v}}{\mathrm{M_p}} \frac{\mathrm{d}m_3}{\mathrm{d}y} \tag{5.5}$$

$$\frac{\mathrm{d}\left[\mathrm{OH}^{-}\right]}{\mathrm{d}y} = -2\frac{\rho_\mathrm{c} k_\mathrm{v}}{\mathrm{M_p}} \frac{\mathrm{d}m_3}{\mathrm{d}y} \tag{5.6}$$

Here, ρ_c, and $\mathrm{M_c}$ are the density and molecular weight of the solid $\left(2.34\ \mathrm{g/cm^3}\right.$ and $\left.58.32\ \mathrm{g/mol}\right)$ respectively, and k_v is the shape factor $(\pi/6$ for spheres$)$. The PBM is implemented in MatLab and the equations system (namely, Eqs. (5.4), (5.5), (5.6)) is solved using the 'ode15s' algorithm. There are a total of eight model parameters to estimate: four stemming from the nucleation rate equation J (A_1, A_2, B_1, B_2), two from the growth rate equation G (k_g, g), and two, C_1 and A_p, from the aggregation rate equation. The estimation of these model parameters is crucial for accurately representing particle dynamics. The optimization routine aims at estimating kinetics parameters for the precipitation process identifying the best fitting between model predictions and collected experimental data. In this regard, a multivariate optimization was performed. Initially, the dataset was split for tuning and validating the model. Concerning Table 4.1, dataset #1 was used for model tuning, and cases from dataset #2 for validation. Each experimental test led to a

PSD from which four moment ratios were computed. Therefore, the model tuning, which involved 8 unknown parameters, ended up with 20 experimental values (i.e., $d_{10}, d_{21}, d_{32}, d_{43}$) to be used in the optimization. A target function, exploiting the built model, was used through the *fmincon* MatLab function in which the global error had to be minimized. The error can be formulated as follows:

$$e = \sum_i \sum_j \sqrt{\left(\frac{d_j^{\text{sim}} - d_j^{\text{exp}}}{d_j^{\text{exp}}} \right)_i^2} \tag{5.7}$$

Eq. (5.7) minimizes for each of the five concentrations (index i) the four characteristic sizes (index j). Since unphysical sets could arise from optimization, proper parameters range, within the *fmincon* MatLab function, were imposed:

Table 5.2 Parameter constraints and Units

	A_1	A_2	B_1	B_2	k_{g}	g	C_1	A_{p}
Lower bound (lb)	10^{19}	10^{10}	200	10	10^{-15}	1	0	10^0
Upper bound (ub)	10^{29}	10^{18}	400	10^2	10^{-9}	2	1	10^7
Units	$\frac{\text{particle no.}}{\text{m}^3\text{s}^1}$				$\frac{\text{m}}{\text{s}}$			$\frac{\text{N}}{\text{m}^2}$

The parameter ranges can be established through references to the scientific literature [81]. For instance, in the case of poorly soluble compounds such as $Mg(OH)_2$ or barium sulfate ($BaSO_4$) [144], the literature presents clear guidelines. Karpiński and Bałdyga [145] reported for these systems a solution particle density $\left(\text{particle no. m}^{-3}\right)$ ranging from 10^{17} to 10^{22} from which the lower and upper bounds for parameter A_1 can be derived accordingly. In line with CNT, A_1 and A_2 can vary by several orders of magnitude. Once the range for A_1 is chosen, the range for A_2 follows. The range values of B_1 and B_2, on the other hand, can be chosen knowing some physical properties of the system such as the interfacial tension [31]. The growth rate, whose intensity is modulated by k_{g}, cannot be higher than it would be in the diffusion-controlled regime and g varies between 1 and 2 depending on the mechanism by which the particles grow (diffusion- or surface integration-controlled respectively) [41]. Ultimately, C_1 corrects any deviation from ideality (namely

$C_1 = 0$) up to a correction of one order of magnitude (namely $C_1 = 1$)[72, 132], while A_p range is tabulated [81].

Equations Summary

In this paragraph, a summary of the presented equations is reported for a PFR system.

Transport Equation for $\bar{\alpha}$:

$$\frac{\mathrm{d}\bar{\alpha}}{\mathrm{d}t} = 0$$

Transport Equation for $\overline{\alpha'^2}$:

$$\frac{\mathrm{d}\overline{\alpha'^2}}{\mathrm{d}t} = -C_f \frac{C_\phi}{2} \frac{\varepsilon}{k} \overline{\alpha'^2}$$

Transport Equation for m_k:

$$\frac{\mathrm{d}\bar{m}_k}{\mathrm{d}t} = JL_\mathrm{c}^k + kGm_{k-1} + \overline{B}_k - \overline{D}_k$$

Transport Equation for $\bar{c}_i$ (reacting ions):

$$\frac{\mathrm{d}\bar{c}_i}{\mathrm{d}t} = -\frac{\nu_i \rho_\mathrm{p} k_\mathrm{v}}{M_\mathrm{p}} \frac{\mathrm{d}m_3}{\mathrm{d}t}$$

5.3 Results and Discussion

Since constrained optimization algorithms generally exploit methods for the local minimum research, different attempts were necessary to land in a local minimum, which could be considered the global one for the actual multi-objective function. The best parameters fitting is reported:

Parameter	A_1	A_2	B_1	B_2	k_g	g	C_1	A_p
Set #1	10^{26}	10^{14}	301	30	10^{-10}	1	0.86	5.9

Table 5.3 Kinetic parameters set

Examining the different rates makes it possible to further assess whether the obtained parameters are physically realistic, as well as the estimation of the confidence interval (see Appendix B.5). These kinetic parameters play a crucial role in determining the change in the total particle number (zeroth-order moment). In Figure 5.7, the calculated values of d_{10} (black solid line) are plotted together with the experimental data (red squares) obtained in the T-mixer, thus showing quite a good agreement between the two. It is worth noting that the simulations were extended to include initial $MgCl_2$ concentration levels lower than in the experiments, showing that the particle size decreases when the concentration is decreased. In conclusion, the overall trend of d_{10} is that it increases monotonically with the initial $MgCl_2$ concentration.

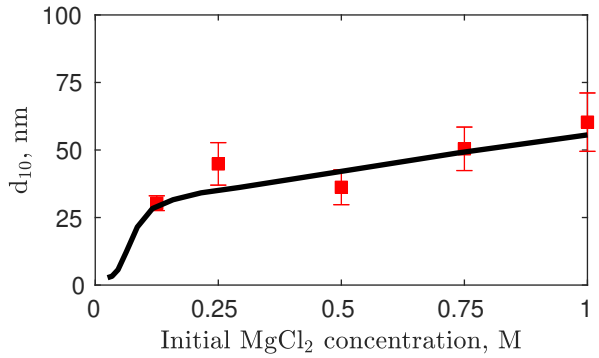

Figure 5.7 Experimental data (d_{10}) collected using the T-mixer for different initial concentrations of MgCl2 (red squares). The inferred parameters are used to fit the data and extrapolate the sizes trend for lower initial MgCl2 concentrations (black solid line).

Y-mixer model validation

We utilized the parameters obtained from the T-mixer to predict the values of d_{10} for the $Mg(OH)_2$ particles obtained in the Y-mixer. While the structure of the PBM remained identical, it was essential to consider the significant differences in flow

dynamics and turbulent fields between the two mixers (see Appendix B.7). We incorporated the k and ε profiles obtained through CFD simulations specific for the Y-mixer to account for these variations.

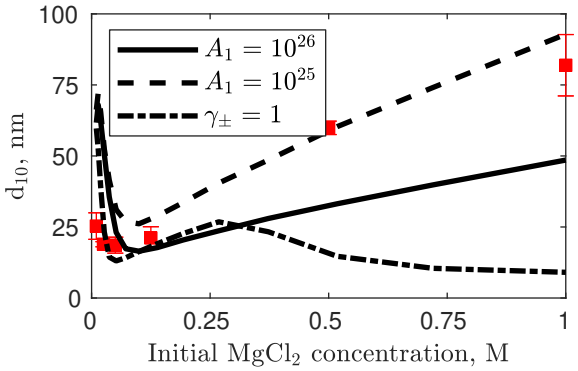

Figure 5.8 Experimental data (d_{10}) collected using the Y-mixer for different initial concentrations of $MgCl_2$ (red squares). Simulation results are shown with three black curves. PBM without modification (solid line), PBM with modified $A_1 = 10^{26}$ particle no $\left(m^{-3}s^{-1}\right)$ (dashed lined), PBM with constant $\gamma_{\pm} = 1$ (dash-dotted line).

In Figure 5.8, the dependence of d_{10} on the initial concentration of $MgCl_2$ is shown for the case of the Y-mixer. The experimental data, red boxes, are plotted together with three curves calculated by using the model. The first curve (solid line) corresponds to the trend predicted by the model keeping the same set of kinetic parameters obtained for the T-mixer, while considering the fluid dynamics characterizing the new Y-mixer system. The second curve (dashed line) represents the trend that would occur if the parameter A_1 were reduced by one order of magnitude. The third curve (dash-dotted line) shows the behavior that would be observed if the activity coefficient had a value of one regardless of the operating conditions.

5.4 Modelling insights

After proving its accuracy, we can utilize the model to better understand the underlying phenomena. Particular attention will be paid to the minimum in d_{10} when varying the initial $MgCl_2$ concentration, experimentally observed in the Y-mixer (Figure 5.8). To this aim, the evolution of the relevant properties of the systems as

a function of the residence time will be analyzed in detail for three concentrations: one on the left of the minimum (i.e., 0.025 M), one at the minimum (i.e., 0.1 M, as obtained through simulations) and one on its right (i.e., 1 M). The zeroth-order moment, m_0, was chosen among all physical quantities to explain the phenomena observed. Indeed, if only molecular processes (i.e., nucleation and growth) are considered, the zeroth-order moment exhibits a sigmoidal shape: it starts from zero (for non-seeded systems) and reaches the upper asymptotic value due to nucleation (growth does not change m_0). Therefore, the zeroth-order moment reaches a plateau for a system where aggregation does not occur. When aggregation is considered, as soon as particles collide and stick together, the zeroth-order moment decreases.

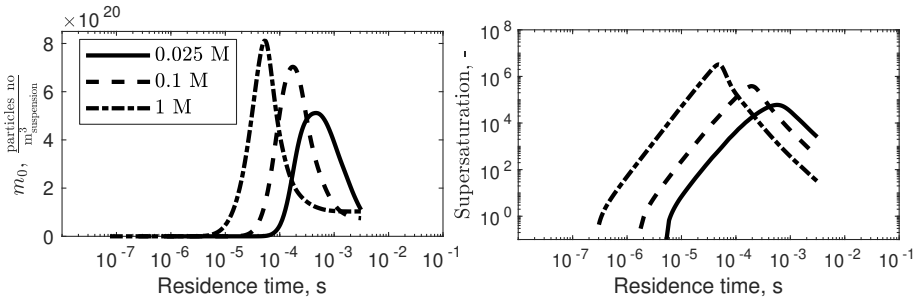

Figure 5.9 m_0 (*left*) and supersaturation (*right*) profiles plotted as a function of the T-mixer residence time for three different initial $MgCl_2$ concentrations.

Let us first examine the observations from the T-mixer configuration. Figure 5.9-*left* reports the evolution of the zeroth-order moment along the mixing channel, i.e., in terms of residence time; it showcases the combined impact of nucleation, growth, and aggregation for the T-mixer. The final residence time in the T-mixer corresponds to the duration required for the fluid to flow through the mixing channel, which, as mentioned, could not be adequately extended. The results obtained from the T-mixer reveal a distinct trend. As depicted in Figure 5.9-*right*, supersaturation gradually builds up, triggering nucleation and subsequent particle growth. Consequently, the zeroth-order moment (m_0) initially exhibits an upward trend, due to the formation of particles. However, particle aggregation eventually decreases the value of m_0. Notably, lower initial $MgCl_2$ concentrations result in lower maximum supersaturation levels, thereby delaying nucleation's inception and leading to fewer particles.

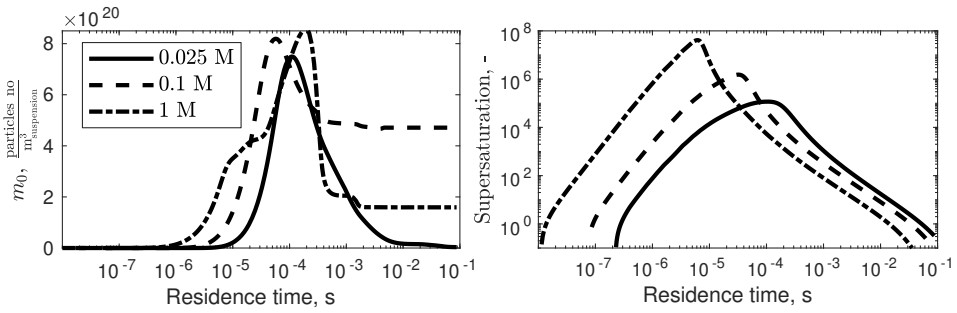

Figure 5.10 m_0 (*left*) and supersaturation (*right*) profiles plotted as a function of the Y-mixer residence time for three different initial $MgCl_2$ concentrations.

Next, let us consider the Y-mixer configuration. The final coil length in the Y-mixer (hence the residence time) was varied based on the concentrations employed in the corresponding experiments (Table 4.1). Specifically, to ensure the completion of the reaction as the concentration range was extended towards smaller concentrations, the final coil length in the Y-mixer was increased accordingly. In Figure 5.10, the reported residence time corresponds to the duration required to achieve complete conversion of the reactants in the least concentrated solution, although the total simulation time is always equal to the residence time at a given operating condition (see Table 4.1). It is worth noticing that this residence time suffices for all other cases, as the driving force amplifies with an increase in the initial $MgCl_2$ concentration. For the Y-mixer (Figure 5.10-*left*), a distinct monotonic trend similar to that observed in the T-mixer configuration is not evident, even though the supersaturation profiles for both setups (Figures 5.9-*right* and 5.10-*right*) exhibit similar trends. One plausible explanation for this trend in the Y-mixer is based on the selectivity of supersaturation. In our investigation, we have explored how the depletion of supersaturation occurs as a direct result of changing the concentration of $MgCl_2$. It is worth recognizing that the dominant mechanism by which supersaturation is depleted varies for different operating conditions. This is further elaborated with the help of Figure 5.11, which shows the relationship between the nucleation rate (J) and the molecular growth rate (G) at different levels of supersaturation.

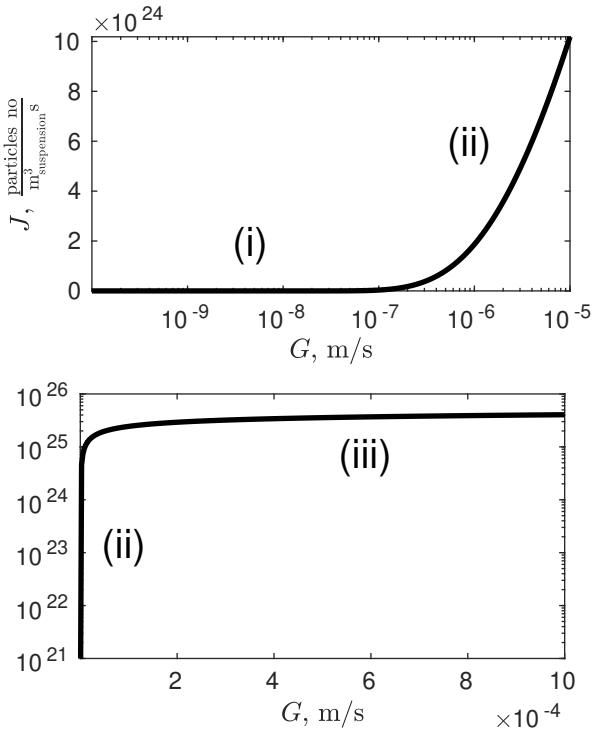

Figure 5.11 Primary nucleation rate as a function of the molecular growth rate for $Mg(OH)_2$. Three regions are identified: (i) the metastable region (S from 0 to $\sim 10^3$), (ii) a nucleation-dominant region (S from $\sim 10^3$ to $\sim 10^5$), and (iii) a growth-dominant region at higher supersaturation levels (S from $\sim 10^5$ onward).

In Figure 5.11 J is plotted against G for increasing supersaturation levels. Due to the highly non-linear nucleation rate the plot is divided into two parts: on the left J is plotted versus G for lower supersaturation levels, whereas on the right the same quantities are plotted for higher supersaturation levels. It is important to notice that Figure 5.11 is based on the kinetics of the specific compound under study (Eq. (2.37) and (2.38)). Three distinct regions can be observed: (i) a metastable region where the nucleation rate variation with the growth rate ($\mathrm{d}J/\mathrm{d}G$) is almost zero, (ii) a second region where $\mathrm{d}J/\mathrm{d}G \to \infty$ (indicating a significant increase in the nucleation rate), and (iii) a third region exhibiting a similar trend of the metastable one but at much higher rates (as supersaturation approaches infinity). This behavior, observed in both crystallization and precipitation processes, was explained by Kubota and co-workers [146, 144] and supports the concept of supersaturation selectivity. Particle growth is favored over nucleation in the metastable region (i). Understanding this concept helps explain the behavior in region (iii), where the nucleation rate is hindered by the

growth of existing particles, resulting in fewer particles that grow larger. Conversely, in region (ii), the nucleation rate increases significantly, depleting supersaturation to form more particles that grow slower. It is worth noticing that the metastable region (i) is hardly accessible in precipitation processes, due to the high supersaturation levels generated even at low concentrations. Therefore, considering regions (ii) and (iii) allows for a better explanation of the trends observed in m_0 at different concentrations (Figure 5.10 *left*) and it helps explain the presence of the minimum in the d_{10} trend (Figure 4.2 - *right*). To assess the influence of each phenomenon, we numerically decoupled molecular processes and secondary processes. We begin by considering a hypothetical scenario where only molecular processes are enabled, and only subsequently, the contribution of aggregation is introduced.

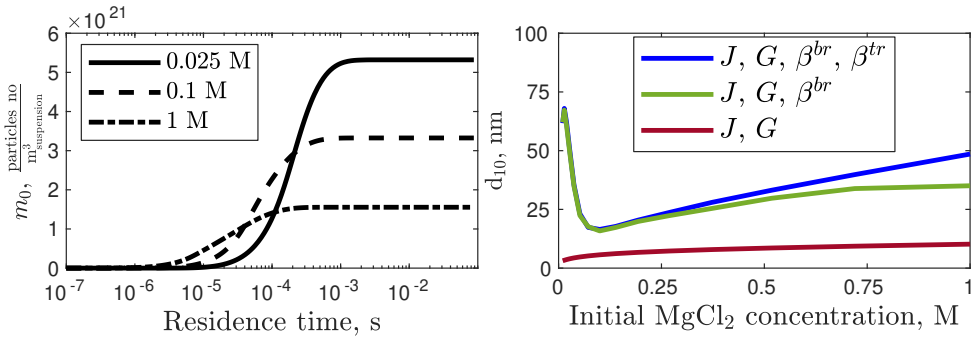

Figure 5.12 m_0 evolution in the Y-mixer considering only molecular processes (*left*); d_{10} trends as a function of the initial $MgCl_2$ concentration (*right*).

The *left* panel of Figure 5.12 focuses on the m_0 evolution for three concentrations as a function of the residence time when solely molecular processes are considered. The *right* panel of Figure 5.12, instead, shows three trends of the d_{10} as a function of the initial concentration of $MgCl_2$. The blue line represents the d_{10} trend when all processes are accounted for. The green line represents the d_{10} trend when nucleation, growth, and Brownian aggregation are considered. Lastly, the red line represents the d_{10} trend when only nucleation and growth processes are considered. For the sake of clarity, let us call 'primary particles' the particles that would potentially occur if aggregation could be prevented (red line), while 'particles' are those that actually result considering aggregation as well (green and blue lines). Moreover, it is worth noticing that molecular and secondary processes do not occur in series but in parallel. Therefore, decoupling the phenomena is merely a numerical expedient through which the discussion can be facilitated. It is evident from the *right* panel that

when only nucleation and growth are considered (Figure 5.12-*right*, red line), the d_{10} exhibits a monotonically increasing trend with increasing initial $MgCl_2$ concentration. This observation is consistent with the findings in Figure 5.11. Specifically, as the concentration increases, the system moves towards the region (iii), indicating that growth is favored over nucleation. Hence, the number of 'primary particles' decreases (Figure 5.12-*left*), implying that the collision frequency decreases and so does the 'particles' size. As it can be seen by comparing the blue and green lines in Figure 5.12-*right*, the Brownian contribution alone in Eq (2.44) produces the minimum, due to the interplay between the collision frequency, β_{coll}, and the aggregation efficiency, ψ, (Eq. (2.44)). Indeed, as the concentration increases, the cementation time (Eq. (2.53)) decreases since it is inversely proportional to G. The interaction time (Eq. (2.52)) is constant since the flow rate is the same (and consequently so are the flow field and the turbulence fields). A decrease in the cementation time, for the same interaction time, results, on average, in an increase in the aggregation efficiency. Therefore, the minimum observed in Figure 5.8 for the Y-mixer is a consequence of the opposite trends of the collision frequency and aggregation efficiency with the initial $MgCl_2$ concentration. It is worth noting that the aggregation efficiency (Eq. (2.51)) depends on fluid dynamics, local supersaturation, and particle sizes and, due to the highly intricate dependencies among these factors, a detailed analysis cannot be performed independently (see Appendix B.6). Moreover, the contribution of turbulent aggregation to d_{10} is negligible except for high initial $MgCl_2$ concentrations, as depicted in (Figure 5.10-*right*) by comparing the blue and green lines. This could be due to the faster desupersaturation process, resulting in a broader particle size distribution where the bigger 'particles' undergo turbulent aggregation, resulting in an increase of

5.5 Improvements in the aggregation kernel

Let us now investigate the role of the correction factor, 10^{C_1}, contained in Eq. (2.49). As mentioned this correction accounts for deviations from the simplification hypotheses under which the aggregation kernels are derived, notably a sufficiently low total particle concentration. By using an empirical approach it is therefore reasonable to link this correction to the total mass of the precipitated solid, proportional to the

third-order moment of the PSD:

$$10^{C_1} = 10^{C_1' m_3(t)} \tag{5.8}$$

The third-order moment, m_3, is calculated accounting for the increasing mass of the precipitated solid. This modification enables us to track the history of solid generation throughout the process at each operating condition. At the beginning of the precipitation process, there is minimal precipitated solid ($m_3 \to 0$) and $10^{C_1' m_3 \to 0}$ approximates 1. As the precipitation process unfolds, the amount of the precipitated solid increases, and consequently, m_3 rises, leading to an increase in $10^{C_1' m_3}$. Additionally, while m_3 starts at zero for all operating conditions, its final value significantly differs with varying initial concentrations of the reactants. This means that $10^{C_1' m_3}$ not only increases with the precipitation process advance but also scales proportionally with the initial concentration of the reactants introduced into the reactor, implying a heightened contribution from aggregation. This modification thus reinforces the already existing correlation between the number of particles and the collision frequency for which the collision frequency increases as the number of particles increases. The choice of the third-order moment is deliberate, as it remains independent of the aggregation source term itself. It is noteworthy that this change in the kernel does not increase the number of parameters. A new parameter identification was therefore conducted on this modified model by using the T-mixer experimental data (Figure 5.13 *left*), with subsequent validation and comparison of simulation predictions against experiments conducted on the Y-mixer (Figure 5.13 *right*).

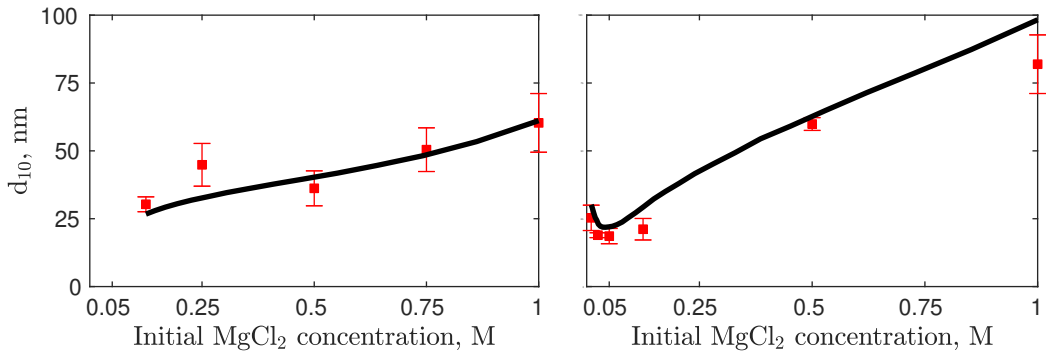

Figure 5.13 Numerical simulations run for the T- (*left*) and Y- (*right*) mixer accounting for the new correction factor shown in Eq. (5.8). The numerical results (solid line) are plotted together with the experimental data (red squares).

One can see that the experimental T-mixer trend is better represented because the model can assure a change in the second derivative (i.e., initially concave and then convex) for the d_{10} as a function of the initial reactant concentration instead of a linear trend. The enhanced predictive capabilities of the model are evident also for the Y-mixer configuration.

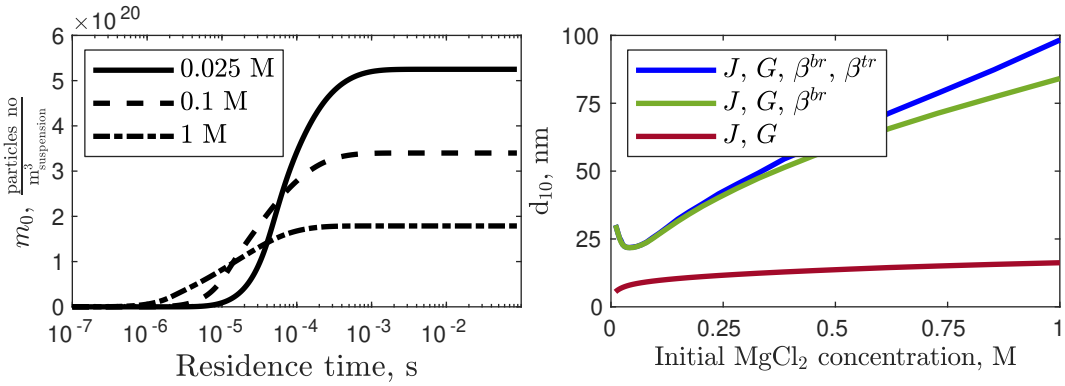

Figure 5.14 m_0 evolution in the Y-mixer considering only molecular processes (*left*); d_{10} trends as a function of the initial $MgCl_2$ concentration (*right*). Simulations are run using Eq. (5.8)

It should also be noted in Figure 5.14 that the introduction of this new correction factor only affects the accuracy of the predictions but not the interaction between the various processes. The comparison between Figure 5.12 and Figure 5.14 shows that the trend of m_0 and d_{10} remains unchanged qualitatively but changes quantitatively. It follows that the model can adequately describe the (intricate) interaction of the phenomena involved and that the introduction of the new correction factor better approximates the particle collision mechanism. The parameters set found through this second optimization is reported in Table 5.4 and can be compared with the initial parameters set (see Appendix B.5). As it is seen most of the identified parameters do not change significantly and only the correction factor is tuned accordingly.

Parameter	A_1	A_2	B_1	B_2	k_g	g	C_1'	A_p
Set #2	$10^{25.8}$	$10^{13.9}$	301	34	$10^{-10.4}$	1.45	29.39	6.37

Table 5.4 Model parameters for aggregation kernel as a function of m_3 (#2).

To summarize, using the new functional form for the correction factor multiplying the aggregation rate, as expressed by Eq. (5.8), leads to a significant improvement in the numerical predictions for both the T-mixer and the Y-mixer. Indeed, set #2 can describe both datasets (Figure 5.13) simply by considering the change of fluid dynamics from the T- to the Y-mixer without further change.

5.6 Conclusions

This chapter focuses on the numerical predictions of $Mg(OH)_2$ precipitation when quite different systems (T- and Y- mixer) are involved. A mono-dimensional model was used to model the $Mg(OH)_2$ precipitation in both T- and Y- mixers. Using an identical set of kinetic parameters, we carefully considered the different fluid dynamics and turbulence features that characterized the two configurations by conducting CFD simulations. The numerical framework demonstrated its capability to accurately predict and describe the precipitation phenomena when transitioning from a T- to a Y-mixer. The model was tuned for a T-mixer system and its prediction capability was assessed when a Y-mixer with two divergent channels and a final coil system was used, by only numerically accounting for the new hydrodynamics with no further adjustments. Furthermore, we provided a comprehensive physical interpretation of the dominant precipitation phenomena. Finally, a novel semi-empirical correction factor based on the third-order moment of the particle size distribution, m_3, was proposed for the aggregation rate. This last correction factor has provided the best quantitative trend compared with the experimental values. It is worth underlining that the ultimate purpose of this novel predictive model (and framework), which has been tuned and validated in this work, will be used for the design of a crystallizer prototype aimed at controlling the granulometry of Magnesium Hydroxide precipitates [147]. Building upon these computational foundations, the subsequent chapter introduces an innovative methodological approach to address classical optimization challenges. This novel approach leverages deep learning techniques to overcome limitations in multi-variate optimization, offering promising avenues for refining and enhancing design processes in complex engineering systems. By seamlessly transitioning from predictive modelling to advanced optimization strategies, we continue to explore cutting-edge methodologies aimed at pushing the boundaries of precision and efficiency in materials engineering and process design.

Chapter 6

Deep Learning Novel Approach for Multi-Objective Optimization

Some of the work described in this chapter has also been previously published in Raponi and Marchisio [148].

6.1 Introduction

A novel machine-learning approach for optimization is presented in this chapter. In line with numerous chemical engineering processes [121, 149, 150], the precipitation kinetics set can be identified by comparison between the PBM outcomes and experimental data through an optimization algorithm as presented in the previous Chapter (see Section 5.2). The effectiveness of optimization algorithms has grown over the years, driven by the increasing computational power available. These advancements are particularly significant in various engineering domains, including process engineering, where researchers frequently encounter large-scale multi-objective problems (LSMOPs) [151]. LSMOPs are typically characterized by extensive search spaces where classical optimization algorithms, such as the conjugate gradient (CG), might not be able to fully explore. An alternative approach involves modifying the CG method by tailoring the line search [152, 153]. While these modified methods are more robust and reliable, they may still be inefficient for multi-objective optimizations [154], where the optimized solution strongly depends on the first-attempt value. A viable alternative that has found widespread use in recent years is the employ-

ment of heuristic [155] and meta-heuristic methods[156]. Heuristic optimization is a technique that aims to find the optimal solution to a problem in a search space too large to explore by classical methods [157]. Meta-heuristic optimization is a higher-level procedure that aims to find, select, and calibrate a heuristic algorithm that can provide the optimal solution for a specific LSMOP [158]. The former includes Particle Swarm Optimization (PSO) [159], while the latter includes Crow Search Optimization (CSO) [160]. These methods offer significant improvements over classical optimization but may require a high number of iterations for precise solutions. A promising compromise between accuracy and computational time involves leveraging artificial intelligence [161]. Hybrid models that integrate first principles models with experimental data through artificial intelligence have shown effectiveness in recent studies[162]. These models combine mechanistic equations that describe physical phenomena with experimental evidence to create a comprehensive understanding of the system. In this chapter, the PBM is employed along with three experimental datasets (one for PBM fitting and two for validation) presented in Section 4.1. The PBM describes particle size evolution due to primary nucleation (homogeneous and heterogeneous), molecular growth, and irreversible aggregation resulting from cementation between particles. The PBM is solved through the Quadrature Method of Moments (QMOM) [102, 103]. It generates numerical data for training a deep-learning fully connected neural network (NN), which is guided by experimental data to identify unknown PBM parameters.

6.2 Parameters Identification

Figure 6.1 presents the flowchart of the PBM framework, with a focus on inputs and outputs.

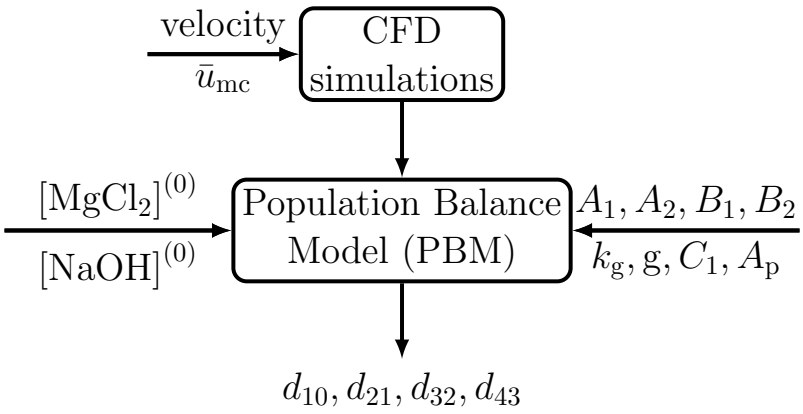

Figure 6.1 Model flowchart

Initially, CFD simulations are conducted for a specified flow rate in the mixing channel, corresponding to a velocity $\bar{u}_{\mathrm{mc}}$, and turbulent fields ($k-\varepsilon$) are integrated into the PBM. Operating conditions, including $MgCl_2$ and NaOH concentrations, are set. Different sizes (d_{10}, d_{21}, d_{32}, d_{43}) are obtained as PBM output depending on the kinetics parameter set. Parameter identification through optimization loops is the initial step in fine-tuning model parameters for process description. In this case, it is applied to determine the parameters that describe the precipitation of $Mg(OH)_2$. Generally, the traditional optimization loop can be represented as shown in Figure 6.2:

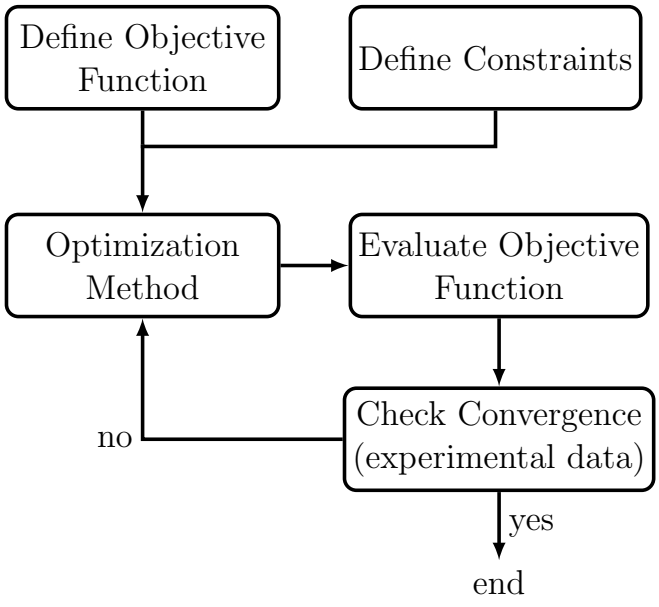

Figure 6.2 Traditional optimization loop scheme

The traditional optimization loop aims to optimize the model's outputs by comparison with experimental data. The PBM, for instance, takes as inputs the kinetics parameters. These latter are identified by comparing the PBM outputs with experimental sizes at various operating conditions. Let $\overrightarrow{\varphi}$ be the vector representing the eight unknown parameters $\left(\overrightarrow{\varphi} = \varphi\left(A_1, A_2, B_1, B_2, k_g, g, C_1, A_\mathrm{p}\right)\right)$, and $\overrightarrow{d}$ be the vector containing the model's outputs $\left(\overrightarrow{d} = d\left(d_{10}, d_{21}, d_{32}, d_{43}\right)\right)$, namely the four characteristic sizes. After implementing the model and identifying the parameters to be tuned, physical limits are defined for each parameter (see Table 5.2). The core of the optimization loop is the optimization algorithm. Various algorithms are available, depending on the task and problem size, namely the number of parameters to be identified. Once the optimization algorithm is chosen, it is initialized with a first-attempt value $\left(\overrightarrow{\varphi}^{\mathrm{I}}\text{, either random or user} - \text{defined}\right)$. The PBM uses this value to calculate a first-attempt output $\left(\overrightarrow{d}^{\mathrm{I}}\right)$, which is compared with experimental data. The goodness of the PBM output is quantified through an error that settles the distance from the experimental values. Since the first-attempt values often return the wrong solution, the optimization algorithm iteratively adjusts the input parameters until the model and experimental data (ideally) align. However, there are limitations to traditional optimization methods, despite their robustness. Firstly, the choice of the initial first-attempt value can heavily influence the optimization process, particularly when expert guidance is lacking. Algorithms like the CG method are susceptible to this limitation. An alternative approach to address this issue is to assume a population of first-attempt values, as in the case of the PSO. Yet, this increases computational costs as the PBM must be evaluated for a larger number of points. The second limitation pertains to the definition of the error, which is user-dependent. Moreover, traditional optimization algorithms can lead to a local minimum, necessitating a large number of runs to explore the entire search space. Lastly, these algorithms require simplified models (e.g., mono-dimensional) that can quickly return outputs when they are called.

Deep learning aided optimization: the Mirror Model In this paragraph, we introduce a novel methodology for multi-objective optimization that leverages NNs. This innovative approach addresses the limitations discussed earlier and substantially reduces computational costs. The initial step involves creating a suitable numerical dataset using the PBM, which takes eight kinetics parameters ($\overrightarrow{\varphi}$) and the concentration of Mg^{2+} as inputs (Figure 6.1). For the simulations, kinetics parameter

values $\left(\overrightarrow{\varphi}^{(i)}\right)$ were randomly selected within their physical variability range, as outlined in Table 5.2. Thus, a large search space could be covered. Since it was used for fitting, the five concentrations from experimental dataset #1 were used in the simulations. The primary objective of the NN is to replace the whole optimization loop by creating a surrogate optimization algorithm capable of identifying precipitation kinetics (NN outputs) starting from experimental sizes (NN inputs). This NN, which mirrors the PBM inputs and outputs, is referred to as the 'mirror model' and represents a data-driven optimization algorithm. Therefore, the mirror model was trained using the four characteristic sizes at an initial Mg^{2+} concentration (five inputs) from simulations run with kinetics parameters that now serve as the mirror model outputs (eight outputs). The mirror model is schematically represented in Figure 6.3.

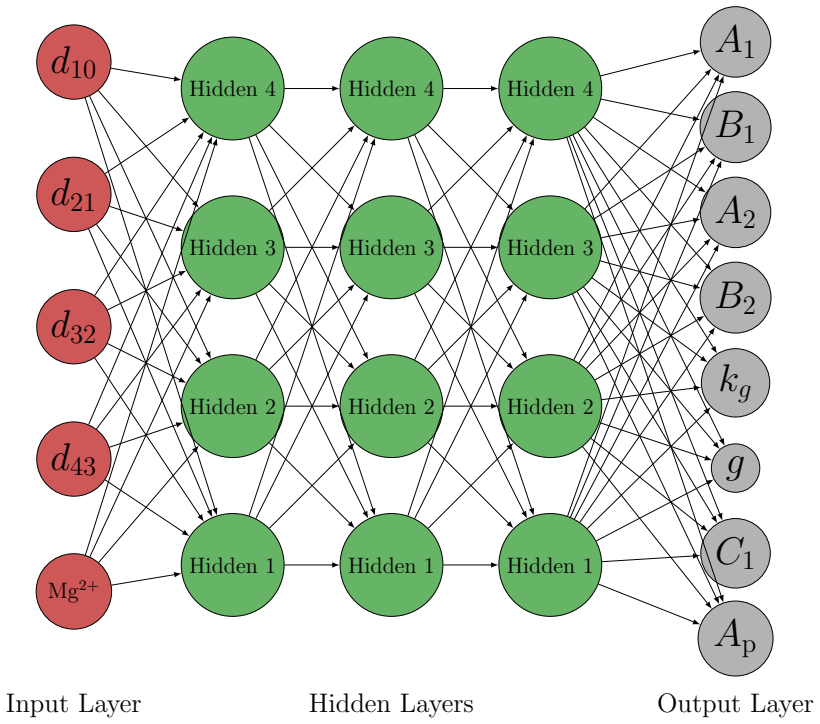

Figure 6.3 Schematic representation of the mirror model focusing on inputs and outputs

Through a preliminary study, we aimed to determine the size of the numerical dataset for effective generalization of patterns between characteristic sizes and kinetic parameter sets within the mirror model. We explored four dataset sizes (100, 200, 300, and 400 simulations) and found that 200 simulations were sufficient. Among these, 160 simulations were allocated for mirror model training, and the remaining

40 were used for testing. For each dataset size, we tested four architectures: (i) 32 - 32, (ii) 32 - 64 - 32, (iii) 64 - 128 - 64, and (iv) 64 - 128 - 128 - 64. Following these architectural evaluations, we investigated the impact of learning rate variation by considering two orders of magnitude (from 10^{-5} to 10^{-3}). The selected mirror model architecture consisted of three hidden layers with 64, 128, and 64 neurons, using a learning rate of 10^{-4}. To prevent overfitting, the 'early-stopping' method was employed. Details are available in the Appendix B.8.

6.3 Results and discussion

The mirror model serves as a valuable tool for identifying kinetics parameters. It operates as a data-driven model, leveraging experimental data. To illustrate its utility, let's assume to provide the four experimental characteristic sizes at a concentration of 0.125 M (corresponding to the first experimental condition in dataset #1, as detailed in Table 4.1) as inputs to the trained mirror model. In response, the mirror model will generate a kinetic parameter set as output. By repeating this process for the following four concentrations in dataset #1 (i.e., 0.25, 0.5, 0.75, and 1 M), four additional $\overrightarrow{\varphi}$ predictions are obtained. The five vectors $\overrightarrow{\varphi}$ obtained using the data-driven mirror model are ideally expected to be identical since the precipitation kinetics are solely related to the compound ($Mg(OH)_2$). However, in practice, achieving a perfect identity is challenging due to various sources of error both experimental and model-related. The first category includes errors, which relate to (i) the device used for characterization, (ii) the method used for quenching to stabilize the suspension, and (iii) the time elapsed between particle synthesis and their stabilization. The second category encompasses model-related errors, which consist of (i) intrinsic numerical errors, (ii) assumptions and simplifications made during the modelling process, and (iii) stochasticity introduced during the neural network training. Considering these factors, it becomes evident that the five parameter vectors $\overrightarrow{\varphi}$ obtained using the data-driven mirror model will not be identical but will exhibit slight variations influenced by the error magnitudes. Nevertheless, this novel methodology provides a way to quantify this deviation. It can be accomplished by calculating, for each parameter, the mean of the five predictions and their standard deviation. The average values, denoted concisely as $\overrightarrow{\bar{\varphi}}$, serve as a measure to evaluate the overall average performance of the PBM. On the other hand, the confidence interval for precipitation

kinetics, proportional to the standard deviation for each parameter $\overrightarrow{\bar{\varphi}'^2}$, is employed to quantify the uncertainty associated with the PBM trend. Let's assume, therefore, to run a statistically significant number of PBM simulations for each concentration (see 'supporting information'). These PBM simulations have inputs in the form of vectors $\overrightarrow{\varphi}$ chosen as follows: a random vector that falls within the range between $\overrightarrow{\varphi} - \overrightarrow{\bar{\varphi}'^2}$ and $\overrightarrow{\varphi} + \overrightarrow{\bar{\varphi}'^2}$ is selected. This procedure allows for quantifying, through the PBM, the average trend and the confidence interval as the operating conditions vary. The kinetics set and its confidence interval are, then, tested for datasets #2 and #3 as shown in Figure 6.4:

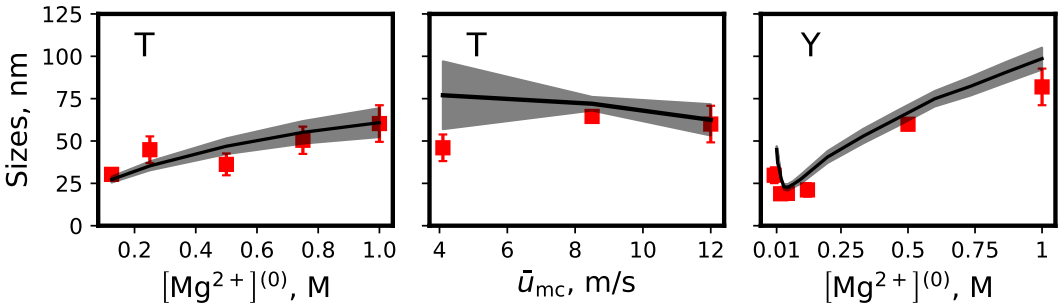

Figure 6.4 PBM outcomes vs experimental datasets. Dataset #1 (*left*) is used for fitting, datasets #2 (*center*) and #3 (*right*) are used for validation

While we have previously discussed average trends, the proposed methodology allows for a more detailed analysis. To begin, we briefly outline the interpretation of average trends. Comparing the PBM outcomes for dataset #1 (Figure 6.4-*left*), we observe that in the T-mixer there is a monotonically increasing trend in particle size as the concentration increases. On the other hand, when we analyze the PBM trend with dataset #2 (Figure 6.4-*center*), we find no significant changes in particle sizes with decreasing flow rate within the mixing channel (or equivalently, as $\bar{u}_{mc}$ decreases). Finally, when the system transitions from a simple T-mixer to a more complex Y-mixer with diverging channels and a final pipe, the PBM continues to accurately predict the particle size trend, including the minimum (Figure 6.4-*right*). This shifting from the T- to the Y-mixer is accounted for in the PBM by running additional CFD simulations to characterize the new flow and turbulent fields (see Figure 6.1, 'CFD simulations' box). It is worth emphasising that the PBM consistently and correctly predicted particle size trends under entirely different conditions, even though these conditions were not originally part of the fitting stage. Moreover, this new methodology enables a quantitative assessment of the

deviation in particle size, represented as a confidence interval. As the concentration increases, the confidence interval expands for both datasets #1 and #3. The rising concentration amplifies the significance of turbulence-related contributions (e.g., turbulent aggregation), making the sizes more prone to variations. Conversely, for dataset #2, the confidence interval widens as the flow rate decreases. When velocity decreases, the uncertainty associated with the RANS turbulent model increases when transitioning from a fully developed turbulent regime to a regime with reduced turbulence [59]. Furthermore, although certain combinations of kinetics parameters have successfully replicated dataset #2 experimental trend, particularly at the lower end of the confidence interval (Figure 6.4-*center*), these results should be carefully considered. It's important to acknowledge the potential influence of quenching times on the measurements, which may have led to slight deviations from what is typically reported in the literature. Generally, as the flow rate decreases or, equivalently, as mixing time increases, one can anticipate larger particle sizes [11], which aligns with the upper end of the confidence interval. In the end, it's important to emphasize the potential applications of the mirror model. Since no assumptions were made about the model, the numerical dataset could consist of modelling approaches more complex than the one employed here. For example, instead of decoupling the flow and turbulent fields, by using a simplified PBE, as done in this work, the model could be based on three-dimensional fully-coupled CFD-PBM simulations. As a result, the proposed methodology allows for precise adjustments, if required, for any model, regardless of its complexity. Notably, this flexibility is not available with CG and PSO.

Key Performance Indicators This section compares the performance of two conventional optimization methods, CG and PSO, with the mirror model. Although CG and PSO are components within the optimization loop as illustrated in Figure 6.2 ('Optimization Method' box), both methods are referred to as if they represent the entire optimization loop. The analysis focuses on two Key Performance Indicators (KPIs): (i) the number of times the PBM is called and (ii) the time required to reach a solution. The mirror model generates a kinetic parameter set for each operating condition, specifically the five concentrations of dataset #1 in the fitting dataset. In contrast, classical optimization methods optimize all operating conditions in the fitting dataset simultaneously. Consequently, each optimization cycle yields only one kinetic parameter set. To conduct a thorough comparative performance analysis,

classical optimization methods were executed five times. The resulting five kinetic parameter sets allowed for the calculation of the mean values and their standard deviation for the parameters. Considering the substantial variations in the ranges of each parameter, often spanning orders of magnitude, a radar plot (Figure 6.5) has been included for visualization. In this plot, each parameter range was normalized between zero and one using the respective minimum and maximum values detailed in Table 5.2.

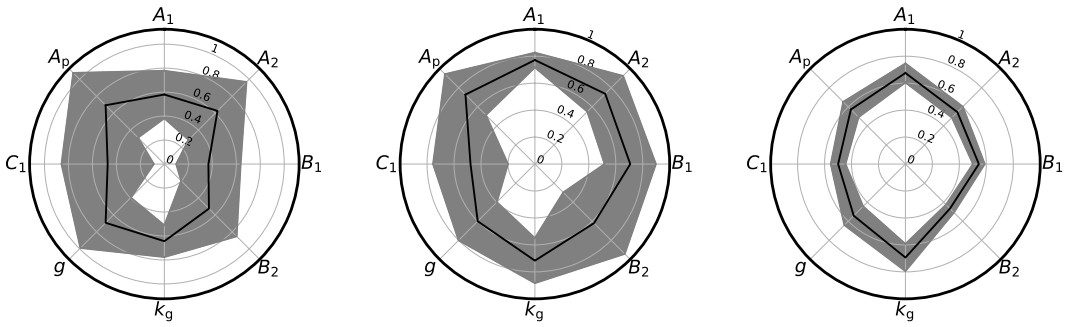

(a) CG (b) PSO (c) NN

Figure 6.5 $\overrightarrow{\varphi}$ and confidence interval

The data in Figure 6.5-*left* indicates that five optimization cycles are insufficient for CG to generate reliable kinetic parameters with a small standard deviation. This outcome is due to the practice of initializing CG with a completely random initial guess in each cycle. This measure was implemented to ensure that user experience did not influence the optimization process and subsequent performance comparison. PSO, instead, is acknowledged for its robustness in overcoming the initial guess limitations of CG, consistently yielding more reliable results. As highlighted in Figure 6.5-*center*, PSO provides an average kinetic parameter set closer to the one offered by the mirror model (Figure 6.5-*right*) and with a smaller standard deviation than the one provided by CG. However, it proves to be more computationally consuming, particularly when dealing with large optimization problems, as depicted in Figure 6.6.

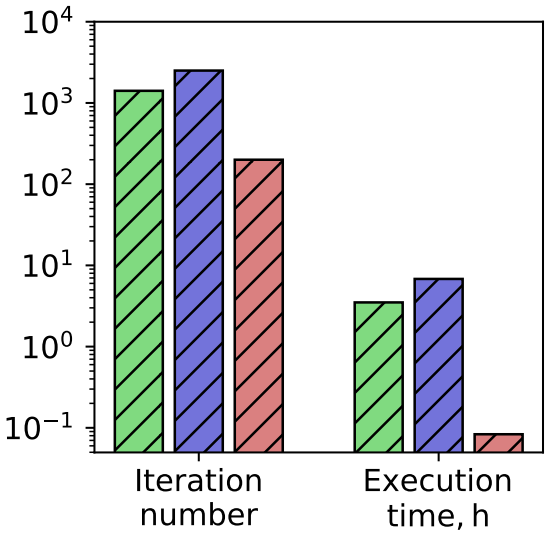

Figure 6.6 KPIs for CG (*green*), PSO (*blue*) and NN (*red*)

On the left of Figure 6.6, the iteration number indicates the number of times the PBM is called. On the right, the cumulative execution time is reported. For CG and PSO, both the iteration number and the execution time represent the total, which is the sum of all five cycles. For the mirror model, the iteration number corresponds to the size of the numerical dataset, which includes 200 simulations (*red* bar on the left). The execution time, instead, covers the dataset generation time, approximately 3 minutes, and the training time, roughly 5 minutes (*red* bar on the right). The contrast between the CG-PSO and the mirror model is striking. CG and PSO respectively make roughly 2000 PBM calls (depicted by the *green-blue* bars on the left), a stark contrast to the mirror model's 200 PBM calls. However, the real standout is evident in the execution time. The mirror model accomplishes its tasks in under 10 minutes, whereas CG and PSO demand nearly 4 hours (*green-blue* vs *red* bars on the right). Additionally, it's important to note that CG and PSO would still need more cycles to narrow down the confidence interval, and expert knowledge would remain invaluable in such cases. Classical methods can get trapped in minima that meet the stopping criteria locally but may not be the optimal solution. Eventually, the kinetics parameters set found through the mirror model is reported in Table 6.1:

Parameter	A_1	A_2	B_1	B_2	k_g	g	C_1	A_p
Set #3	$10^{25.45}$	$10^{15.4}$	301	57	$10^{-11.15}$	1.5	0.79	5.3

Table 6.1 Kinetic parameters set

6.4 Conclusion

In this chapter, an innovative deep learning-based approach for multi-objective optimization is presented, with a primary focus on characterizing $Mg(OH)_2$ precipitation kinetics using experimental data. This research leveraged three distinct datasets: one for PBM fitting and two for PBM validation. The first dataset explored the influence of increasing initial Mg^{2+} concentrations on particle sizes within a T-mixer. In contrast, the second dataset delved into the effects of reduced flow rates in the same system. The third dataset examined the impact of increasing initial Mg^{2+} concentrations on particle sizes in a more complex system, featuring a Y-mixer, two divergent channels, and a final pipe. The presented methodology exploited a mono-dimensional PBM. This model takes kinetics parameters and concentration as inputs, yielding four characteristic sizes as outputs. The PBM was harnessed to generate a numerical dataset, which was used to train an NN which mirrored the PBM inputs and outputs (consequently called the 'mirror model'). The mirror model took characteristic sizes and Mg^{2+} concentrations as inputs and returned kinetics parameters as outputs. The mirror model played a crucial role in predicting kinetics parameters from experimental sizes from the first dataset. These predictions were used to compute an average set and standard deviation. Surprisingly, the PBM proved highly adept at describing changes in flow rates and substantial reductions in Mg^{2+} concentrations within the new Y-mixer system, even when these conditions were unprecedented. To further evaluate the mirror model's performance, we assessed two KPIs: (i) the iteration number and (ii) the execution time. These KPIs were then compared with those provided by two widely used algorithms, CG and PSO. The outcome of this comparison underscores the enormous potential of the mirror model, with KPIs consistently at least an order of magnitude lower than those of CG and PSO. It should be, finally, emphasized that the synergy between first principal models and experimental data-driven optimization can be exploited for the tuning of more sophisticated models when, for example, experimental data are deficient, time-consuming, or expensive to obtain. In this regard, a 3D model for optimizing the precipitation of magnesium hydroxide is shown in the next chapter.

Chapter 7

Towards the optimization of a pilot-scale prototype

7.1 Introduction

Magnesium hydroxide precipitation is a complex process influenced by multiple factors. Throughout this thesis, 3D modelling techniques are leveraged to calibrate a precipitation model, aiming to enhance our understanding of the intricate dynamics governing the synthesis of magnesium hydroxide particles. The calibrated model is a powerful tool for designing and optimising a prototype precipitation system. This final chapter aims to demonstrate the efficacy of the tuned 3D precipitation model in guiding the development of a prototype for magnesium hydroxide precipitation.

A brief overview of the workflow used for parametric identification is as follows: simulation runs using the CFD-PBM model with the 3D geometry were initiated. These simulations served as the foundation for training a neural network, acting as a surrogate for the 3D model. The surrogate model, in turn, was employed to generate a numerical dataset used to train the mirror model for kinetic parameter identification, aligning with experimental data. The calibration process became feasible through experiments conducted in the T-mixer, allowing the calibrated model to be applied for the optimization of the prototype. This integrated approach, leveraging both computational simulations and experimental data, facilitated a comprehensive understanding of the system dynamics and parameters, culminating in an effective calibration and subsequent optimization of the pilot-scale prototype.

7.2 Materials and Methods

In the last few years, ResourSEAs and the University of Palermo have designed and built a pilot-scale prototype for magnesium hydroxide precipitation from different kinds of brines [29, 147]. The resulting prototype is now patented by ResourSEAs S.r.l [163]. At first, however, the design process was led by trial and error rather than a specific tool for the maximization of the sought effect. This research endeavours have addressed the imperative need to fill this gap, standing as a testament to the practical applications of modelling tools. This chapter unfolds as a journey into the analytical insights that have steered the optimization of the prototype. While respecting the constraints imposed by the patent, this chapter delves into the analysis that will eventually inform the prototype's optimization, offering a comprehensive understanding of the considerations and decisions that can underpin this innovative solution enhancement. Through this exploration, this thesis aims to bridge the theoretical foundations with tangible outcomes. The reactor is tubular with multiple feeds and can be modelled as a Multi-Feed Plug Flow Reactor (MF-PFR). A schematic representation of the MF-PFR is presented in Figure 7.1

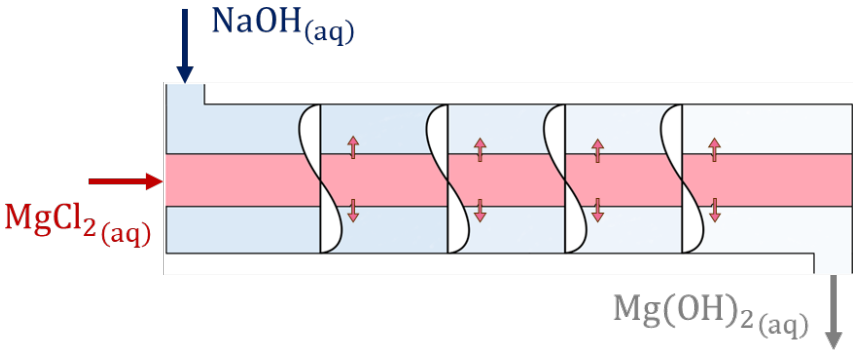

Figure 7.1 Multi-Feed Plug Flow Reactor sketch

As evident from Figure 7.1, the reactor comprises an external circular crown for the alkaline solution feed, while the saline solution is introduced through the internal tube. The two sections are connected through a series of nozzles, compelling the internally fed fluid to pass through them, as the only outlet from the reactor is located on the external circular crown. Additionally, within the reactor, there are fixed impellers designed to induce a rotational motion, thereby enhancing mixing conditions before the injection zones of the second fluid. For the sake of confiden-

tiality, all patent-covered parameters are reported in dimensionless form, including the reactor's dimensions in Figure 7.2

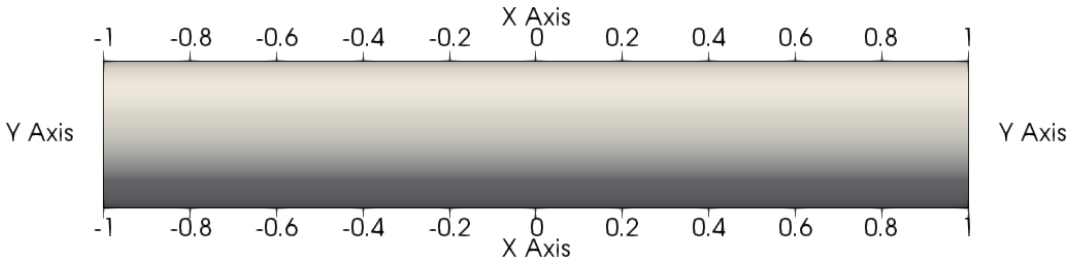

(a) MF-PFR longitudinal (xy) view

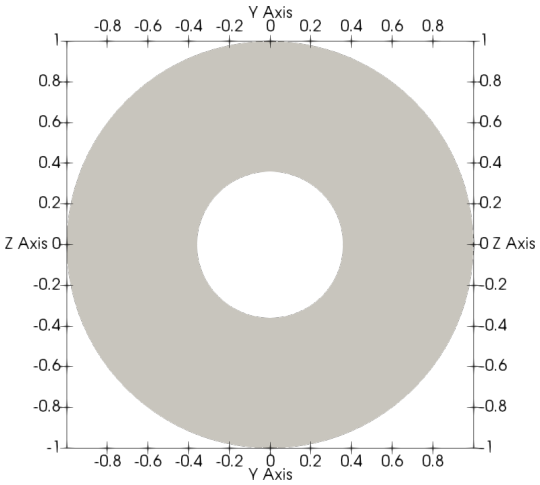

(b) MF-PFR sectional (yz) view

Figure 7.2 MF-PFR sectional and longitudinal views

Selecting the turbulence model

As demonstrated, precipitation phenomena are closely tied to mixing processes, hence the fluid dynamics of the system. Given the high *Re* number, different choices of turbulence models can lead to significant variations in fluid dynamics and, consequently, precipitation. In the absence of experimental data to determine the most suitable turbulence model, LES simulations were conducted, offering higher accuracy

compared to RANS models among which the choice was to be made. Consideration was given to two-equation RANS models to cover a wide range of situations for accurately simulating the system's critical aspects. The selected RANS models included the standard $k-\varepsilon$, $k-\varepsilon$ RNG, and $k-\omega$ SST. Among the LES models, two were applied: the Smagorinsky model, a zero-equation model, and the k-equation model, a one-equation model. The comparison was based on the developed fluid dynamic characteristics, with a detailed analysis of the velocity field around the blades. In particular, the vortex size in the rear zone of the blades was compared. Another comparison aspect focused on the difference in turbulent kinetic energy fields. A quantitative comparison was conducted by calculating the error associated with each cell, defining the error as:

$$er_1 = \frac{|k_{\mathrm{RANS}} - k_{\mathrm{LES}}|}{\max\left(k_{\mathrm{RANS}}, k_{\mathrm{LES}}\right)} \tag{7.1}$$

Regarding the execution of LES simulations, to promote rapid convergence and greater stability, they were initialized with the solution obtained using the standard $k-\varepsilon$ model. The simulations were run for a sufficiently long time to achieve a solution statistically independent of initial conditions (10 residence times). However, since LES simulations capture fluctuations not described by RANS models, a time averaging of the solution was necessary for comparison. The averaging continued until the mean value became time-independent (5 residence times), indicating no significant variations. A second simulation was conducted using the $k-\omega$ SST model as an initial guess to verify whether the hypothesis of independence from initial conditions was confirmed. The grid used for these simulations was chosen to resolve at least 80% of the turbulent kinetic energy. To determine the characteristic size of the first grid to use, the minimum size was calculated according to equation 7.2:

$$\max\left(\Delta\right) = \frac{1}{5}\min\left(l_0\right) \tag{7.2}$$

Here, l_0 is obtained from the RANS simulations and represents the integral length scale defined as:

$$l_0 = \left(\frac{k^{3/2}}{\varepsilon}\right)^{1/4} = \frac{\mathrm{k}^{\frac{1}{2}}}{\omega\, C_{\mu}^{\frac{1}{4}}} \tag{7.3}$$

As described in Section 2.1, LES simulations are characterized by explicitly solving part of the flow field and modelling the remaining part. To evaluate the turbulent

kinetic energy of both contributions, it was necessary to assess them separately (Figure 7.3).

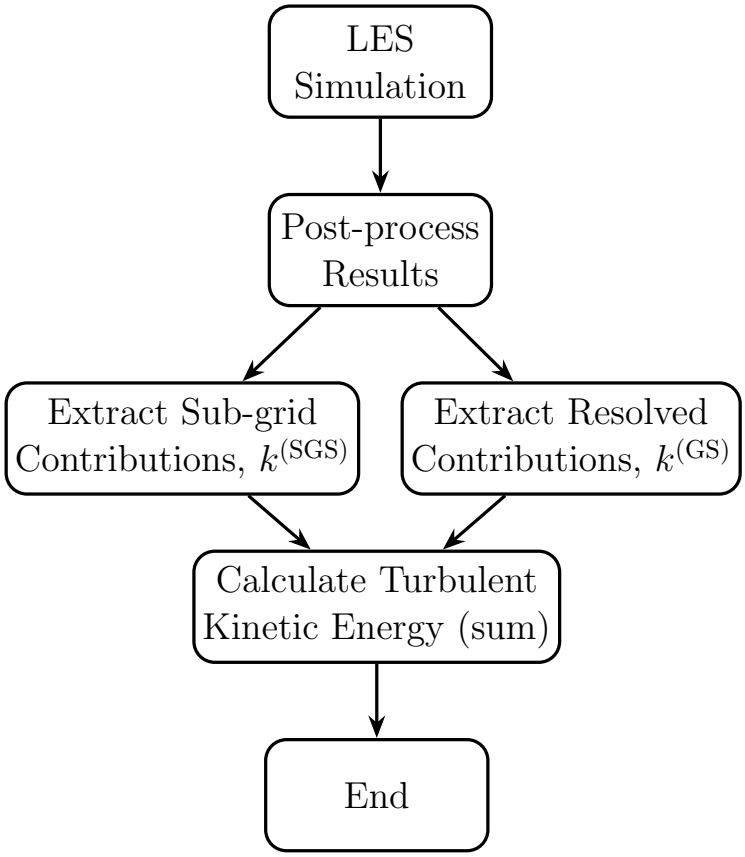

Figure 7.3 Flowchart for turbulent kinetic energy calculation in LES simulations

Indeed, it was necessary to compute the time-averaged velocity to derive the fluctuating velocity of the resolved part of the flow field based on the difference with its instantaneous values. Subsequently, the $k^{(GS)}$ was calculated as the mean of the squares of the fluctuating velocities.

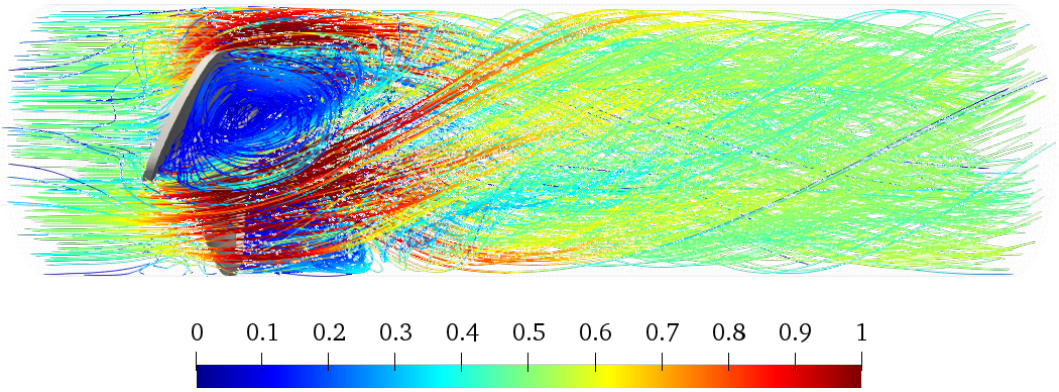

Figure 7.4 Average flow field obtained through LES simulations

Analyzing the flow field depicted in Figure 7.4, it becomes evident that the presence of the vortex following the blade plays a critical role. This vortex represents a portion of the fluid with high residence times. Examining the dimensions of the vortex, it is immediately evident that the $k-\varepsilon$ standard model deviates widely from the solution of all the other models. In the case of the $k-\varepsilon$ standard model, the vortex does not extend far beyond the impeller, whereas all the other models lead to the generation of vortices extending approximately 0.2 (dimensionless x-length). This result is of considerable interest due to the proximity of the vortex to the feeding zone. As a quantitative analysis, the distribution functions of the error on the k field were evaluated. The distribution function was defined as follows:

$$f_i(\varphi) = \frac{1}{\varphi_{i+1} - \varphi_i} \frac{\sum_j V_j}{V_{tot}} \tag{7.4}$$

$$\sum_i [f_i(\varphi)(\varphi_{i+1} - \varphi_i)] = 1 \tag{7.5}$$

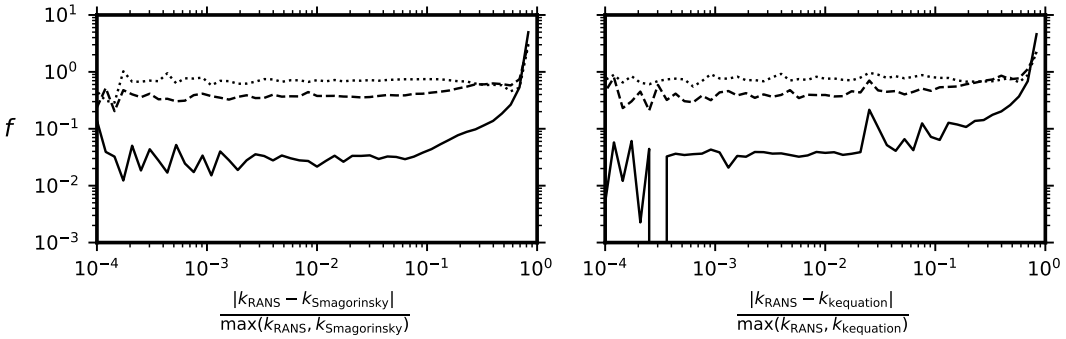

Figure 7.5 Error distribution function comparing Smagorinsky with RANS simulations (*left*) and k-eq with RANS (*right*). $k-\varepsilon$ (solid line), $k-\varepsilon$ RNG (dotted line) and $k-\omega$ SST (dashed line)

Figure 7.5 compares the error distribution functions for the three RANS models and the Smagorinsky one (*left*) and for the three RANS models and the k-Eq one (*right*). The result shows a significant overestimation of k when applying the $k-\varepsilon$ standard model. This leads to an average error approaching almost four orders of magnitude compared to the Smagorinsky model. However, it is important to note that the Smagorinsky model exhibits differences of several orders of magnitude lower than all the studied models, including the LES k-Eq model. This discrepancy occurs only in the reactor region preceding the impellers, a location not reached by the reactants and having little influence on the flow field on the opposite side of the impellers. The reason for this difference can be attributed to the fact that before the blades there is no vortex formation. This results in a solution with small percentages of explicitly resolved solutions (i.e., less intense turbulence), highlighting the impact between the zero-equations model (Smagorinsky) and the one-equation one (k-Eq). As shown in Figure 7.5, the $k-\varepsilon$ RNG and $k-\omega$ SST models present large areas where the turbulence kinetic energy has values of similar magnitude compared with the LES simulations. Therefore, based on the flow fields and turbulent kinetic energy, the $k-\varepsilon$ standard model yields a solution that greatly deviates from the other models, which, instead, agree with each other. A comparison was made between the $k-\omega$ SST and the $k-\varepsilon$ RNG turbulence models, through the error:

$$er_2 = \frac{|k_{k-\varepsilon \text{ RNG}} - k_{k-\omega \text{ SST}}|}{k_{k-\omega \text{ SST}}} \tag{7.6}$$

Here, $k_{k-\varepsilon\ RNG}$ and $k_{k-\omega\ SST}$ represent the turbulent kinetic energy values returned from the $k-\varepsilon$ RNG and $k-\omega$ SST models, respectively. The distribution function for the error computed according to Eq. 7.6 is shown in Figure 7.6:

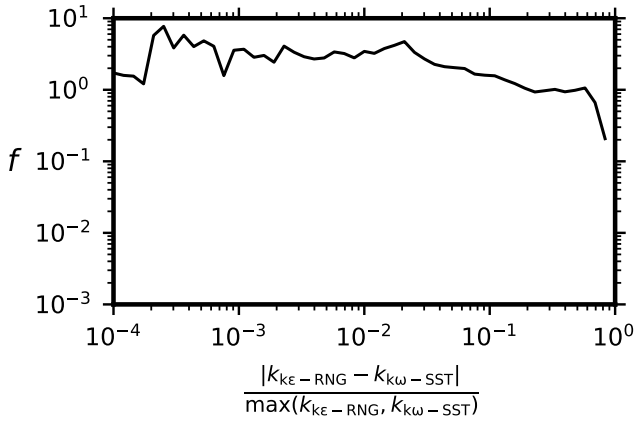

Figure 7.6 Error distribution function comparing the $k-\varepsilon$ RNG and $k-\omega$ SST models

By examining the distribution function, it can be affirmed that the turbulence models predict similar values. The average error is 0.3. In conclusion, the $k-\varepsilon$ standard model was excluded for the reasons mentioned earlier and the $k-\omega$ SST model was selected. Similar to the $k-\omega$ SST model, the $k-\varepsilon$ RNG leads to a solution resembling those proposed by LES simulations. However, the $k-\omega$ SST was preferred on the $k-\varepsilon$ RNG as it requires lower computational times.

7.3 Results and Discussion

In this paragraph, the focus lies on simulations to explore the impact of both the reactant concentrations and the nozzle position and number on reactant mixing. The goal is to maximize prototype performance by optimizing swirling flow in the circular crown. For this purpose, the effect of fluid dynamics on reactant mixing has been analyzed, by primarily monitoring the supersaturation. Finally, the precipitation process has been examined to understand how the solid product is spatially distributed and the characteristic sizes of the formed $Mg(OH)_2$ particles.

Effect of the reactant concentrations

Initially, the effect of reactant concentration was studied. Three concentrations were considered for Mg^{2+} and three for OH^- resulting in a matrix of nine elements:

$[Mg^{2+}]^{(in)}$, M	$[OH^-]^{(in)}$, M		
	0.005	0.01	0.02
0.1	(a)	(b)	(c)
0.3	(d)	(e)	(f)
0.6	(g)	(h)	(i)

Table 7.1 The nine concentration combinations used in the simulations

The study was conducted with the same flow field and turbulent properties. This means that the mixture fraction and its variance are also the same for all operating conditions. Figure 7.7 shows the mixture fraction and its variance on the streamlines the particles would follow if they started from the two nozzles (the model assumes a one-way coupling approach).

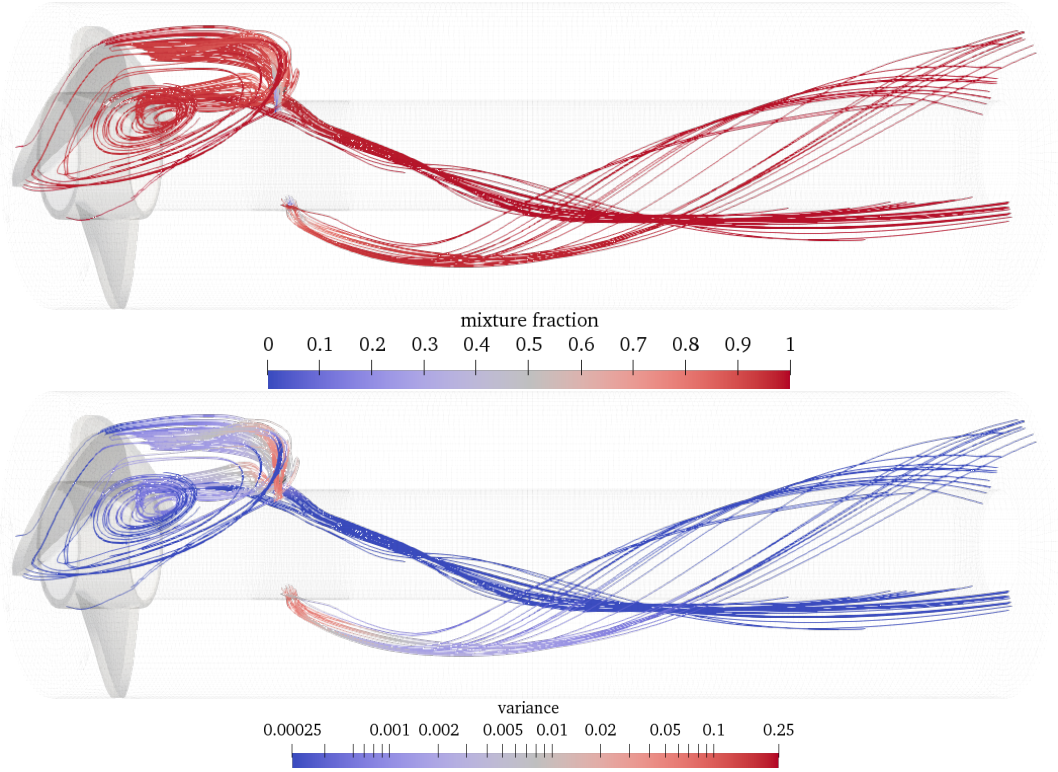

Figure 7.7 Mixture fraction (*top*) and its variance (*bottom*) for the configuration with the two nozzles

Figure 7.7 shows that all precipitation dynamics occur at the two nozzles. The Mg^{2+} jet entering the circular crown changes the mixing fraction locally (corresponding to light blue in Figure 7.7-*top*). Consequently, mixing at the macro-scale generates segregation at the micro-scale as indicated by the red lines at the nozzles in Figure 7.7-*bottom*. Although the flow field, mixture fraction and variance are the same for all the simulations, this does not mean working under the same mixing conditions. It should be recalled that supersaturation is calculated based on the magnesium hydroxide formed in the aqueous phase:

$$\bar{c}_{Mg^{2+}} = \min\left(\left[Mg^{2+}\right], \frac{\left[OH^{-}\right]}{2}\right) f\left(\bar{\alpha}, \bar{\alpha}'^{2}, \bar{\alpha}_{s}\right) \tag{7.7}$$

$$\alpha_s = \frac{2\left[Mg^{2+}\right]^{(in)}}{2\left[Mg^{2+}\right]^{(in)} + \left[OH^{-}\right]^{(in)}} \tag{7.8}$$

$$\tag{7.9}$$

Here, $f\left(\bar{\alpha}, \bar{\alpha}'^2, \bar{\alpha}_s\right)$ is a weight function that defines the contribution of mixing, $\left[Mg^{2+}\right]^{(in)}$ and $[OH^-]^{(in)}$ are the reactant concentrations entering the control volume and $\left[Mg^{2+}\right]$ and $[OH^-]$ are the concentrations in the fluid domain. It is worth noting that the weight function f (Eq. 7.8) is related to the stoichiometric mixture fraction $\bar{\alpha}_s$ (Eq. 7.9) through the concentrations. It follows that an increase in concentration always leads to an increase in the first term in Eq. 7.8 ($\min\left(\left[Mg^{2+}\right], 2\left[OH^-\right]\right)$), while the effect on the second term (f) is not unique but depends on the local value of $\bar{\alpha}$ with respect of $\bar{\alpha}_s$. The $\bar{\alpha}_s$ values for all nine simulations are reported:

$\left[Mg^{2+}\right]^{(in)}$, M	$[OH^-]^{(in)}$, M		
	0.005	0.01	0.02
0.1	0.976	0.952	0.909
0.3	0.992	0.984	0.968
0.6	0.996	0.992	0.984

Table 7.2 α_s values used in the simulations

Lastly, it is worth mentioning that, on average, the mixing fraction in the reactor is close to 1 (as the flow rate of $MgCl_2$ is low). Therefore, the farther the value of α_s is from 1 the worse the mixing is. The monitored variables, used for comparison, are the supersaturation, S, and the zeroth-order moment, m_0. Figure 7.8 shows the simulation results for the supersaturation whereas Figure 7.9 shows the simulation results for the m_0.

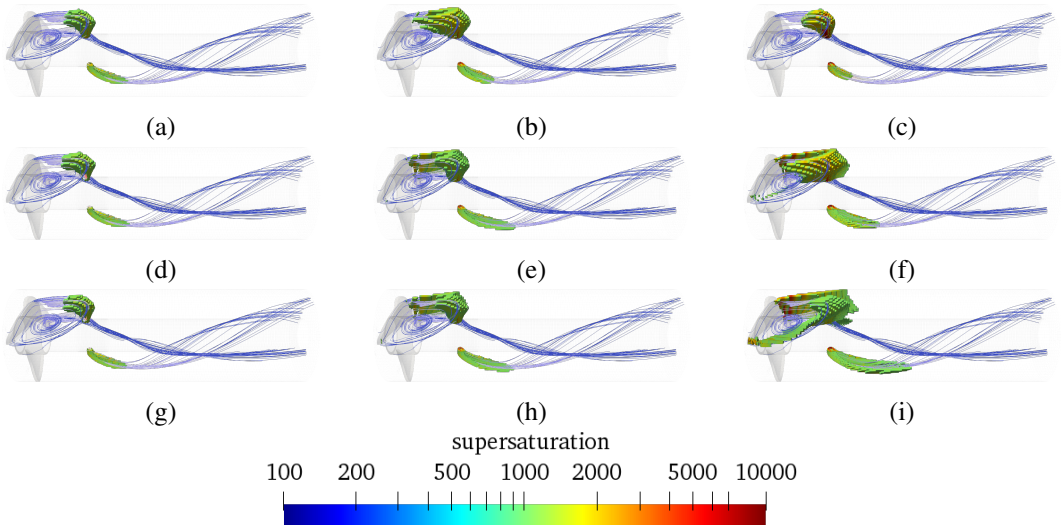

Figure 7.8 Supersaturation fields for nine combinations of reactant concentration

Figure 7.8 shows the supersaturation levels reached within the system. The areas represented correspond to cells with supersaturation values greater than 1000 (the legend has been adapted for the sake of visualization). It is evident from Eq. 7.8 that local supersaturation is controlled by the concentration of OH^-. When α_s varies little with increasing Mg^{2+} concentration (Table 7.2, first column), at the same OH^- concentration, the final supersaturation profile also slightly varies (cases 7.8a, 7.8d, 7.8g). The same happens when the second column in the Table 7.2 is considered (cases 7.8b, 7.8e, 7.8h). However, if one row in Table 7.2 is considered, the variation is much more significant. Let's take the first line as an example. The value of $\bar{\alpha}_s$ decreases along the line, thus implying a worsening of mixing. Instead, OH^- concentration increases, leading to higher supersaturation values. Since the first row has the most pronounced decrease in the value of $\bar{\alpha}_s$, these two effects compete with each other. It is seen that between cases 7.8a and 7.8b, the supersaturation increases both in value and volume. Indeed, in these two cases, the increase (doubling) in OH^- concentration has a much greater effect than the decrease in $\bar{\alpha}_s$ (almost negligible). When, however, the OH^- concentration is further increased (doubled again), but the $\bar{\alpha}_s$ decreases more significantly, the supersaturation volume decreases as shown in cases 7.8b and 7.8c. In this case, mixing becomes controlling. Finally, the simulation matrix was constructed in such a way that a fair comparison could be made between cases where mixing was identical. In this regard, the following two pairs in Table 7.2 can be considered: cases 7.8d and 7.8h and cases 7.8e and 7.8i. Both pairs

have the same value of $\bar{\alpha}_s$ (0.992 for the former and 0.984 for the latter). This means that f in Eq. 7.8 is the same and, therefore, the only effect studied is the increase in the concentration of both reactants. As one would expect, an increase in concentration results in an increase in supersaturation and the volume of fluid affected by precipitation. Therefore, it can be concluded that, unless extremely high supersaturation levels and precipitation volumes are needed (cases 7.8f and 7.8i), low OH^- concentrations can be preferred. By employing a smaller amount of reactant (therefore, smaller costs), almost the same supersaturation profiles are obtained. In addition, the m_0 is reported:

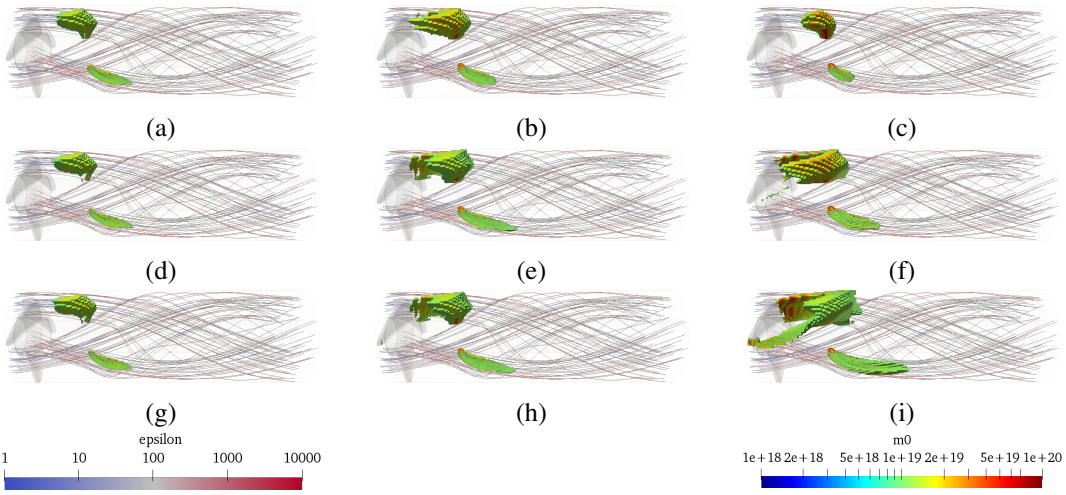

Figure 7.9 The ε field plotted on the streamlines and m_0 fields for nine combinations of reactant concentration

In Figure 7.9 the streamlines, on the other hand, represent the path a particle takes in the fluid, and the field reported on the streamlines is the epsilon field. The region in each subplot represents cells where m_0 has a value higher than 10^{19}. Similar considerations to those for supersaturation can be made for m_0. The qualitative discussion remains unchanged, while more quantitative changes between the different profiles can be appreciated.

Effect of the nozzle number and position

Since the system is characterized by an instantaneous reaction, the mixing of reactants plays a crucial role. Therefore, it is essential to consider the flow field developed in the reactive section of the prototype. Once the positions of interest for the analysis

were identified, simulations were conducted under identical operating conditions to compare results influenced solely by the effect of nozzle position. A total of six simulations were conducted at the same flow rate and concentrations. Three nozzles, respecting flow symmetry, were used. The mutual position of the three nozzles was not changed. In fact, for the same axial coordinate (x), the three nozzles were rotated so that two cases were considered. The first case (I) refers to the injection of Mg^{2+} into the low fluid velocity zones of the fluid. The second case (II) refers to the injection of Mg^{2+} into the high-velocity zones. These two conditions were repeated in three sections (different values of the x-coordinate) resulting in six simulations. Figure 7.10 shows the six different simulation setups reporting the velocity fields when the nozzles' rotation is varied and the epsilon field:

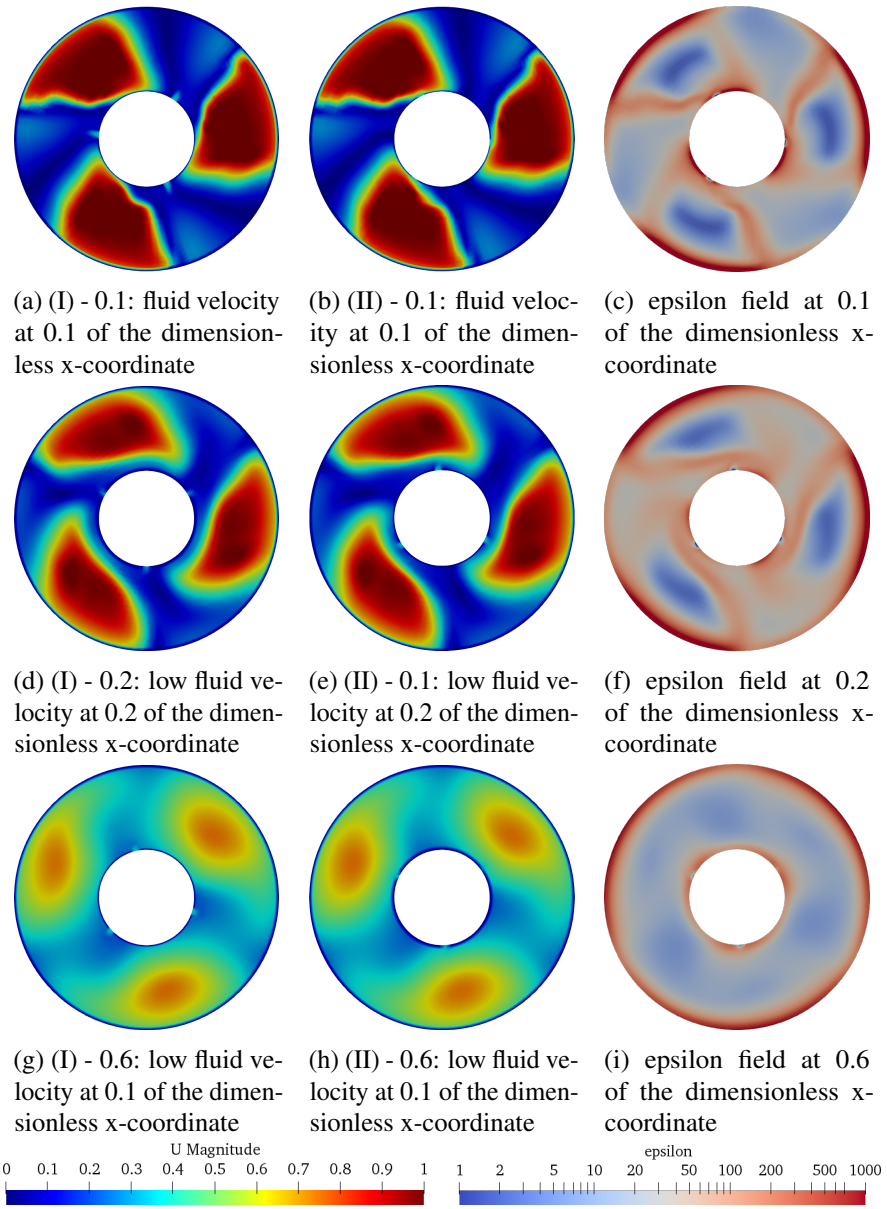

(a) (I) - 0.1: fluid velocity at 0.1 of the dimensionless x-coordinate

(b) (II) - 0.1: fluid velocity at 0.1 of the dimensionless x-coordinate

(c) epsilon field at 0.1 of the dimensionless x-coordinate

(d) (I) - 0.2: low fluid velocity at 0.2 of the dimensionless x-coordinate

(e) (II) - 0.1: low fluid velocity at 0.2 of the dimensionless x-coordinate

(f) epsilon field at 0.2 of the dimensionless x-coordinate

(g) (I) - 0.6: low fluid velocity at 0.1 of the dimensionless x-coordinate

(h) (II) - 0.6: low fluid velocity at 0.1 of the dimensionless x-coordinate

(i) epsilon field at 0.6 of the dimensionless x-coordinate

(j)

(k)

Figure 7.10 Hole Placement: Representation of the velocity magnitude in the feed sections in the proposed simulations

To ensure a fair comparison across all the proposed reactor configurations, simulations were conducted on a geometry comprising the examined block and a portion of the subsequent block, extending to the next feed.

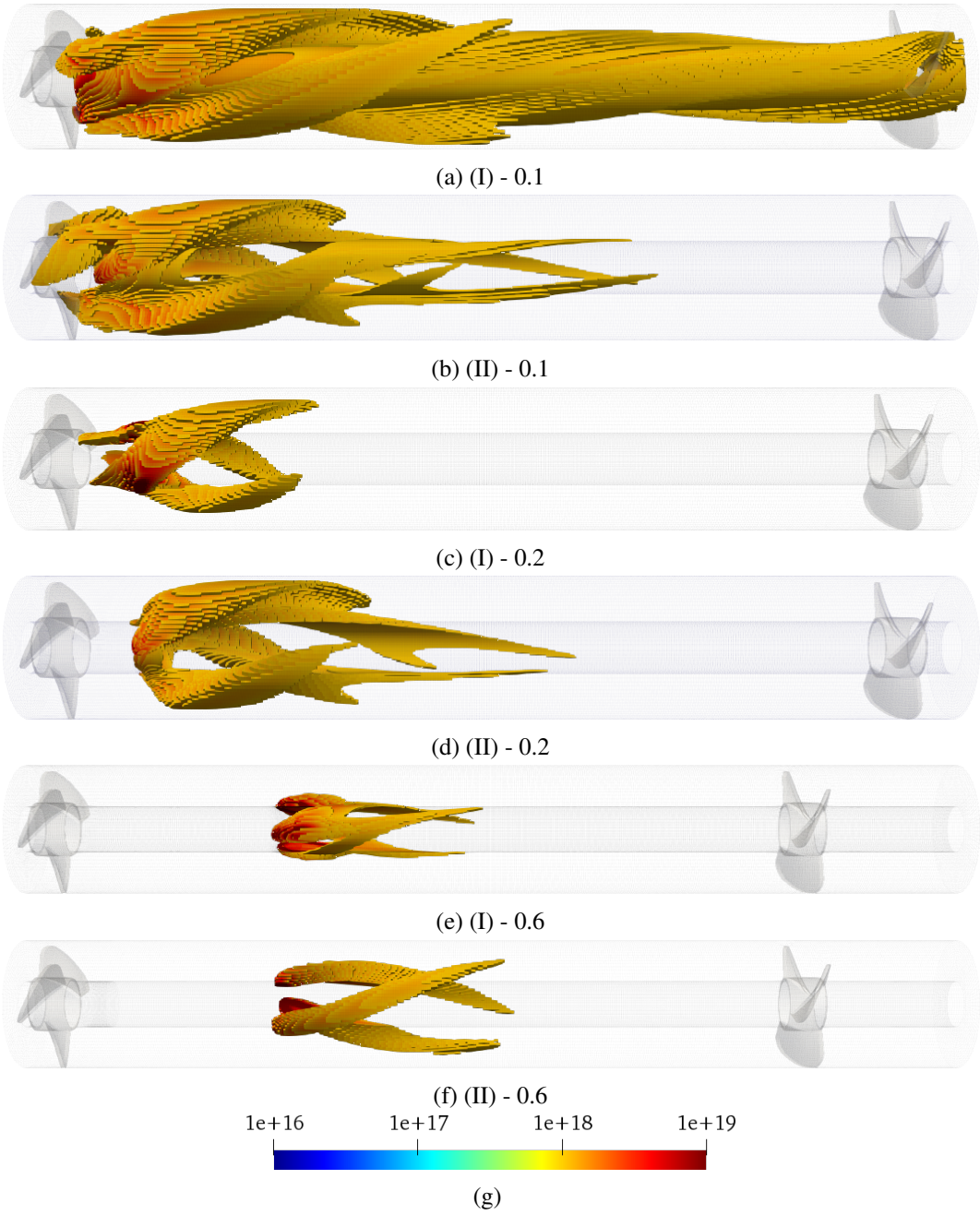

(a) (I) - 0.1

(b) (II) - 0.1

(c) (I) - 0.2

(d) (II) - 0.2

(e) (I) - 0.6

(f) (II) - 0.6

(g)

Figure 7.11 m_0 fields for the six simulations. The cells correspond to a region in which m_0 has values greater than 10^{18} particle no./m^3

Figures 7.10 and 7.11 provide interesting results. The rotation of the nozzles has a substantial impact in the two cases (Figures 7.11a and 7.11b) where the nozzles are located at a distance of 0.1 of the dimensionless coordinate. Figures 7.10a, 7.10b and 7.10c show that the turbulence is locally very different, resulting in two effects. The

former is an increase in macro- and micro-mixing and the latter is an increase in the aggregation contribution. At a length of 0.2 the dimensionless coordinate, the effect is already less intense as shown in Figures 7.11c, 7.11d. Figures 7.10d and 7.10e show that the vortex is no longer adjacent to the inner tube and, consequently, the local turbulence found in both cases is similar (Figure 7.10f). The main change in m_0 profiles depends on the vortex the three Mg^{2+} jets encounter. The scenario depicted in Figure 7.10d indicates that the vortex is not promptly encountered, resulting in a slight backward motion of the particles. In contrast, the situation illustrated in Figure 7.10e showcases an immediate interaction with the vortex. Finally, the effect of rotating the holes to a position equal to 0.6 (Figures 7.11e and 7.11f) of the dimensionless coordinate has practically no effect on the m_0. This is because the flow fields (Figures 7.10g and 7.10h) and, consequently, the turbulence (Figure 7.10i) have been dampened (and homogenised) by the fluid motion itself. Therefore, regardless of the rotation, the three nozzles see similar turbulence and the trend of m_0 is nearly the same.

7.4 Conclusions

This chapter focused on introducing a pilot-scale prototype and exploring the possibility of optimization using a previously calibrated 3D model. After presenting the geometry, the impact of various operational conditions on the products was investigated. The study began by examining the influence of reagent concentrations at constant flow rates. Subsequently, we assessed the effects of the number of needles, their rotation, and their positions within the control volume. The 3D model provided valuable insights. Interestingly, an increase in the concentration of OH^- did not directly increase supersaturation. If the concentration of OH^- rises significantly compared to that of Mg^{2+}, the stoichiometric mixing fraction decreases, limiting the prototype's performance due to mixing constraints. This implies the potential to operate at lower concentrations and, consequently, at reduced costs. Furthermore, the rotation of the needles and their distance from the blade also significantly influenced particle formation. This indicates that utilizing a 3D model can aid in optimizing the prototype based on specific product requirements. In summary, this chapter provides crucial insights into the operational parameters affecting the performance of the pilot-scale prototype. The use of a 3D model not only enhances our understanding

but also offers a pathway for optimizing the prototype to meet the desired product specifications.

Chapter 8

Conclusions

This research aimed to advance the understanding and application of magnesium recovery processes from brines and bitterns, particularly within the context of CRMs. A computational modelling framework was developed, focusing on the precipitation of magnesium hydroxide, aligning with circular economy principles as described in Chapter 1.

The initial phase involved the characterization of mixing dynamics in T-mixers with square and circular cross-sectional geometries, as reported in Chapter 3. Experimental data, coupled with CFD (RANS simulations) using the β-PDF approach, facilitated the tuning and validation of the flow field and turbulent properties, essential for subsequent accurate modelling of the precipitation process.

Following the validation of mixing characteristics, precipitation tests, presented in Chapter 4, were conducted under varied operating conditions and reactor configurations. The PSD data provided insights into the impact of initial magnesium concentration and flow rates, assessed using a T-mixer with a circular cross-section. Additionally, a Y-mixer configuration, followed by two diverging channels and a final pipe of constant diameter allowed to extend the investigation towards smaller concentrations, offering a comprehensive understanding of parameter sensitivity.

Parametric identification, a pivotal aspect of the research, employed two distinct approaches. Traditional algorithms such as Conjugate Gradient (CG) and Particle Swarm Optimization (PSO) were compared against an innovative methodology integrating deep-learning algorithms. This involved the development of an NN, referred to as the 'mirror model,' trained on a numerical dataset derived from the

PBM coupled with CFD simulations. Both the CFD-PBM and NN are introduced and detailed in Chapters 5 and 6. The mirror model demonstrated superior performance in predicting kinetics parameters, highlighting its potential for practical applications.

In Chapter 7, a three-dimensional one-way coupled CFD-PBM model was implemented for the optimization of a pilot-scale prototype for magnesium hydroxide precipitation. Collaboration between ResourSEAs and the University of Palermo resulted in a patented design, marking a significant contribution to practical applications in circular economy initiatives. The exploration of analytical insights guiding prototype optimization, while considering constraints imposed by the patent, provides valuable understanding for enhancing innovative solutions.

This research has navigated the interface between theoretical foundations and tangible outcomes. By emphasizing practical applications of modelling tools, this work contributes substantively to advancing magnesium hydroxide precipitation technologies within the broader framework of sustainable resource utilization. The optimized prototype, a product of collaborative efforts, stands as a testament to the efficacy of computational modelling in driving innovations aligned with circular economy principles. As this chapter concludes, it underscores the importance of ongoing exploration and collaboration in advancing sustainable solutions for critical material recovery.

Bibliography

[1] T. E. Graedel, Rachel Barr, Chelsea Chandler, Thomas Chase, Joanne Choi, Lee Christoffersen, Elizabeth Friedlander, Claire Henly, Christine Jun, Nedal T. Nassar, Daniel Schechner, Simon Warren, Man yu Yang, and Charles Zhu. Methodology of metal criticality determination. *Environmental Science & Technology*, 46:1063–1070, 1 2012. ISSN 0013-936X. doi: 10.1021/es203534z.

[2] T. E. Graedel, E. M. Harper, N. T. Nassar, Philip Nuss, and Barbara K. Reck. Criticality of metals and metalloids. *Proceedings of the National Academy of Sciences*, 112:4257–4262, 4 2015. ISSN 0027-8424. doi: 10.1073/pnas.1500415112.

[3] Katy Roelich, David A. Dawson, Phil Purnell, Christof Knoeri, Ruairi Revell, Jonathan Busch, and Julia K. Steinberger. Assessing the dynamic material criticality of infrastructure transitions: A case of low carbon electricity. *Applied Energy*, 123:378–386, 6 2014. ISSN 03062619. doi: 10.1016/j.apenergy.2014.01.052.

[4] Eva Barteková and René Kemp. National strategies for securing a stable supply of rare earths in different world regions. *Resources Policy*, 49:153–164, 9 2016. ISSN 03014207. doi: 10.1016/j.resourpol.2016.05.003.

[5] Ewa Lewicka, Katarzyna Guzik, and Krzysztof Galos. On the possibilities of critical raw materials production from the eu's primary sources. *Resources*, 10(5), 2021. doi: 10.3390/resources10050050.

[6] Marzena Smol, Paulina Marcinek, Joanna Duda, and Dominika Szołdrowska. Importance of sustainable mineral resource management in implementing the circular economy (ce) model and the european green deal strategy. *Resources*, 9:55, 5 2020. ISSN 2079-9276. doi: 10.3390/resources9050055.

[7] Gergely Tóth. Circular economy and its comparison with 14 other business sustainability movements. *Resources*, 8:159, 9 2019. ISSN 2079-9276. doi: 10.3390/resources8040159.

[8] Florinda Martins and Helio Castro. Significance ranking method applied to some eu critical raw materials in a circular economy – priorities for achieving

sustainability. *Procedia CIRP*, 84:1059–1062, 2019. ISSN 22128271. doi: 10.1016/j.procir.2019.04.281.

[9] Florinda F. Martins and Hélio Castro. Raw material depletion and scenario assessment in european union – a circular economy approach. *Energy Reports*, 6:417–422, 2 2020. ISSN 23524847. doi: 10.1016/j.egyr.2019.08.082.

[10] H.M. Saif, R.M. Huertas, S. Pawlowski, J.G. Crespo, and S. Velizarov. Development of highly selective composite polymeric membranes for li+/mg2+ separation. *Journal of Membrane Science*, 620:118891, 2 2021. ISSN 03767388. doi: 10.1016/j.memsci.2020.118891.

[11] G. Battaglia, S. Romano, A. Raponi, D. Marchisio, M. Ciofalo, A. Tamburini, A. Cipollina, and G. Micale. Analysis of particles size distributions in mg(oh)2 precipitation from highly concentrated mgcl2 solutions. *Powder Technology*, 398:117106, 2022. ISSN 0032-5910. doi: https://doi.org/10.1016/j.powtec.2021.117106.

[12] F. Vicari, S. Randazzo, J. López, M. Fernández de Labastida, V. Vallès, G. Micale, A. Tamburini, G. D'Alì Staiti, J.L. Cortina, and A. Cipollina. Mining minerals and critical raw materials from bittern: Understanding metal ions fate in saltwork ponds. *Science of The Total Environment*, 847:157544, 11 2022. ISSN 00489697. doi: 10.1016/j.scitotenv.2022.157544.

[13] V. Vallès, J. López, M. Fernández de Labastida, O. Gibert, A. Leskinen, R. T. Koivula, and J. L. Cortina. Polymeric and inorganic sorbents as a green option to recover critical raw materials at trace levels from sea saltwork bitterns. *Green Chemistry*, 25:700–719, 2023. ISSN 1463-9262. doi: 10.1039/D2GC02338E.

[14] V. Vallès, M. Fernández de Labastida, J. López, G. Battaglia, D. Winter, S. Randazzo, A. Cipollina, and J.L. Cortina. Sustainable recovery of critical elements from seawater saltworks bitterns by integration of high selective sorbents and reactive precipitation and crystallisation: Developing the probe of concept with on-site produced chemicals and energy. *Separation and Purification Technology*, 306:122622, 2 2023. ISSN 13835866. doi: 10.1016/j.seppur.2022.122622.

[15] Syed Abdullah Shah, Roberta Cucchiara, Fabrizio Vicari, Andrea Cipollina, Alessandro Tamburini, and Giorgio Micale. Energetic valorisation of saltworks bitterns via reverse electrodialysis: A laboratory experimental campaign. *Membranes*, 13:293, 2 2023. ISSN 2077-0375. doi: 10.3390/membranes13030293.

[16] Anish Koyamparambath, Jair Santillán-Saldivar, Benjamin McLellan, and Guido Sonnemann. Supply risk evolution of raw materials for batteries and fossil fuels for selected oecd countries (2000–2018). *Resources Policy*, 75:102465, 3 2022. ISSN 03014207. doi: 10.1016/j.resourpol.2021.102465.

[17] Agnieszka A. Pilarska, Łukasz Klapiszewski, and Teofil Jesionowski. Recent development in the synthesis, modification and application of mg(oh)2 and mgo: A review. *Powder Technology*, 319:373–407, 9 2017. ISSN 00325910. doi: 10.1016/j.powtec.2017.07.009.

[18] Giulia Balducci, Laura Bravo Diaz, and Duncan H. Gregory. Recent progress in the synthesis of nanostructured magnesium hydroxide. *CrystEngComm*, 19: 6067–6084, 2017. ISSN 1466-8033. doi: 10.1039/C7CE01570D.

[19] H. Y. Zahran, S. S. Shneouda, I. S. Yahia, and Farid El-Tantawy. Facile and rapid synthesis of nanoplates mg(oh)2 and mgo via microwave technique from metal source: structural, optical and dielectric properties. *Journal of Sol-Gel Science and Technology*, 86:104–111, 4 2018. ISSN 0928-0707. doi: 10.1007/s10971-018-4613-2.

[20] Wang Shu-Yu, He Wen-Zhi, Liu Chang, Li Guang-Ming, and Zhang Fei-Er. Characterizations and preparation of mg(oh)2 nanocrystals through ultrasonic–hydrothermal route. *Research on Chemical Intermediates*, 42:4135–4145, 5 2016. ISSN 0922-6168. doi: 10.1007/s11164-015-2264-2.

[21] A. Cipollina, M. Bevacqua, P. Dolcimascolo, A. Tamburini, A. Brucato, H. Glade, L. Buether, and G. Micale. Reactive crystallisation process for magnesium recovery from concentrated brines. *Desalination and Water Treatment*, 55:2377–2388, 8 2015. ISSN 19443986. doi: 10.1080/19443994.2014.947771.

[22] Jun Zheng and Wei Zhou. Solution-phase synthesis of magnesium hydroxide nanotubes. *Materials Letters*, 127:17–19, 7 2014. ISSN 0167577X. doi: 10.1016/j.matlet.2014.04.076.

[23] A. Alamdari, M. R. Rahimpour, N. Esfandiari, and E. Nourafkan. Kinetics of magnesium hydroxide precipitation from sea bittern. *Chemical Engineering and Processing: Process Intensification*, 47:215–221, 2 2008. ISSN 02552701. doi: 10.1016/j.cep.2007.02.012.

[24] Sadegh Yousefi, Behrooz Ghasemi, and Mohammad Tajally. Peg-assisted synthesis and formation mechanism of mg(oh)2 nanostructures using natural brine. *Applied Physics A*, 126:641, 8 2020. ISSN 0947-8396. doi: 10.1007/s00339-020-03814-w.

[25] Marian Turek and Witold Gnot. Precipitation of magnesium hydroxide from brine. *Industrial & Engineering Chemistry Research*, 34:244–250, 1 1995. ISSN 0888-5885. doi: 10.1021/ie00040a025.

[26] Jyh-Ping Hsu and Anca Nacu. Preparation of submicron-sized mg(oh)2 particles through precipitation. *Colloids and Surfaces A: Physicochemical and Engineering Aspects*, 262:220–231, 7 2005. ISSN 09277757. doi: 10.1016/j.colsurfa.2005.04.038.

[27] Debao Wang, Caixia Song, and Zhengshui Hu. Synthesis of mono-dispersed mg(oh) 2 nanoflakelets. *Journal of Dispersion Science and Technology*, 29: 1010–1012, 7 2008. ISSN 0193-2691. doi: 10.1080/01932690701810011.

[28] Daniele La Corte, Fabrizio Vassallo, Andrea Cipollina, Marian Turek, Alessandro Tamburini, and Giorgio Micale. A novel ionic exchange membrane crystallizer to recover magnesium hydroxide from seawater and industrial brines. *Membranes*, 10:303, 10 2020. ISSN 2077-0375. doi: 10.3390/membranes10110303.

[29] F. Vassallo, C. Morgante, G. Battaglia, D. La Corte, M. Micari, A. Cipollina, A. Tamburini, and G. Micale. A simulation tool for ion exchange membrane crystallization of magnesium hydroxide from waste brine. *Chemical Engineering Research and Design*, 173:193–205, 9 2021. ISSN 02638762. doi: 10.1016/j.cherd.2021.07.008.

[30] Carolina M F Santos, Ana F B Andrade, and Sonia D F Rocha. The effect of caustic magnesia natural impurities on magnesium oxide hydroxylation, 2017.

[31] S Bhandarkar, R Brown, and J Estrin. Studies in rapid precipitation of hydroxides of calcium and magnesium. *Journal of Crystal Growth*, 97:406–414, 1989. ISSN 00220248. doi: 10.1016/0022-0248(89)90222-4.

[32] D.J. Gunn and M.S. Murthy. Kinetics and mechanisms of precipitations. *Chemical Engineering Science*, 27:1293–1313, 6 1972. ISSN 00092509. doi: 10.1016/0009-2509(72)80105-2.

[33] Qiuhua Yuan, Zhengwu Lu, Peixin Zhang, Xiongbiao Luo, Xiangzhong Ren, and Teresa D. Golden. Study of the synthesis and crystallization kinetics of magnesium hydroxide. *Materials Chemistry and Physics*, 162:734–742, 7 2015. ISSN 02540584. doi: 10.1016/j.matchemphys.2015.06.048.

[34] Arne E. Nielsen and O. Söhnel. Interfacial tensions electrolyte crystal-aqueous solution, from nucleation data. *Journal of Crystal Growth*, 11:233–242, 12 1971. ISSN 00220248. doi: 10.1016/0022-0248(71)90090-X.

[35] A Packter. The rapid precipitation of magnesium hydroxide from aqueous solutions: Analysis of nucleation and crystal growth kinetics, final nucleus numbers and primary crystal sizes, 1985.

[36] Venktesh S. Shirure, Anand S. Pore, and Vishwas G. Pangarkar. Intensification of precipitation using narrow channel reactors: Magnesium hydroxide precipitation. *Industrial & Engineering Chemistry Research*, 44:5500–5507, 7 2005. ISSN 0888-5885. doi: 10.1021/ie049248d.

[37] Xingfu Song, Shuying Sun, Dengke Zhang, Jin Wang, and Jianguo Yu. Synthesis and characterization of magnesium hydroxide by batch reaction crystallization. *Frontiers of Chemical Science and Engineering*, 5:416–421, 12 2011. ISSN 2095-0179. doi: 10.1007/s11705-011-1125-9.

[38] Clifford Y. Tai, Chia-Te Tai, Ming-Hui Chang, and Hwai-Shen Liu. Synthesis of magnesium hydroxide and oxide nanoparticles using a spinning disk reactor. *Industrial & Engineering Chemistry Research*, 46:5536–5541, 8 2007. ISSN 0888-5885. doi: 10.1021/ie060869b.

[39] Hongyan Shen, Youzhi Liu, and Bin Song. Preparation and characterization of magnesium hydroxide nanoparticles in a novel impinging stream-rotating packed bed reactor. *Journal of Chemical Engineering of Japan*, 49:372–378, 2016. ISSN 0021-9592. doi: 10.1252/jcej.15we093.

[40] Tobias Schikarski, Holger Trzenschiok, Wolfgang Peukert, and Marc Avila. Inflow boundary conditions determine t-mixer efficiency. *Reaction Chemistry and Engineering*, 4:559–568, 3 2019. ISSN 20589883. doi: 10.1039/c8re00208h.

[41] Pawel M. Orlewski and Marco Mazzotti. Modeling of mixing-precipitation processes: Agglomeration. *Chemical Engineering and Technology*, 43:1029–1039, 6 2020. ISSN 15214125. doi: 10.1002/ceat.201900551.

[42] B.E. Launder and D.B. Spalding. The numerical computation of turbulent flows. *Computer Methods in Applied Mechanics and Engineering*, 3:269–289, 3 1974. ISSN 00457825. doi: 10.1016/0045-7825(74)90029-2.

[43] Sherif H. El Tahry. k-epsilon equation for compressible reciprocating engine flows. *Journal of Energy*, 7:345–353, 7 1983. ISSN 0146-0412. doi: 10.2514/3.48086.

[44] Antti Hellsten. Some improvements in menter's k-omega sst turbulence model. American Institute of Aeronautics and Astronautics, 6 1998. doi: 10.2514/6.1998-2554.

[45] Florian R Menter, Martin Kuntz, Robin Langtry, et al. Ten years of industrial experience with the sst turbulence model. *Turbulence, heat and mass transfer*, 4(1):625–632, 2003.

[46] F. R. Menter. Two-equation eddy-viscosity turbulence models for engineering applications. *AIAA Journal*, 32:1598–1605, 8 1994. ISSN 0001-1452. doi: 10.2514/3.12149.

[47] V. Yakhot, S. A. Orszag, S. Thangam, T. B. Gatski, and C. G. Speziale. Development of turbulence models for shear flows by a double expansion technique. *Physics of Fluids A: Fluid Dynamics*, 4:1510–1520, 7 1992. ISSN 0899-8213. doi: 10.1063/1.858424.

[48] Paul A. Libby and Forman A. Williams, editors. *Turbulent Reacting Flows*, volume 44. Springer Berlin Heidelberg, 1980. ISBN 978-3-540-10192-5. doi: 10.1007/3-540-10192-6.

[49] Guy P. Brasseur, Mary Barth, Jan Kazil, Edward G. Patton, and Yuting Wang. Segregation of fast-reactive species in atmospheric turbulent flow. *Atmosphere*, 14:1136, 7 2023. ISSN 2073-4433. doi: 10.3390/atmos14071136.

[50] Ahmed F Ghoniem, Alexandre Joel Chorin, and Antoni K Oppenheim. Numerical modelling of turbulent flow in a combustion tunnel. *Philosophical Transactions of the Royal Society of London. Series A, Mathematical and Physical Sciences*, 304(1484):303–325, 1982.

[51] H. Nagasawa, N. Aoki, and K. Mae. Design of a new micromixer for instant mixing based on the collision of micro segments. *Chemical Engineering & Technology*, 28:324–330, 3 2005. ISSN 0930-7516. doi: 10.1002/ceat.200407118.

[52] Henning Bockhorn, Dieter Mewes, Wolfgang Peukert, and Hans-Joachim Warnecke, editors. *Micro and Macro Mixing*. Springer Berlin Heidelberg, 2010. ISBN 978-3-642-04548-6. doi: 10.1007/978-3-642-04549-3.

[53] D.L. Marchisio and R.O. Fox. *Reacting Flows and the Interaction between Turbulence and Chemistry*. Elsevier, 2016. doi: 10.1016/B978-0-12-409547-2.11526-4.

[54] Charles G Speziale. Turbulence modeling for time-dependent rans and vles: a review. *AIAA journal*, 36(2):173–184, 1998.

[55] Pankaj Mishra and KR Aharwal. A review on selection of turbulence model for cfd analysis of air flow within a cold storage. In *IOP conference series: Materials science and engineering*, volume 402, page 012145. IOP Publishing, 2018.

[56] Robert D Moser, Sigfried W Haering, and Gopal R Yalla. Statistical properties of subgrid-scale turbulence models. *Annual Review of Fluid Mechanics*, 53:255–286, 2021.

[57] Wolfgang Rodi. Turbulence modeling and simulation in hydraulics: A historical review. *Journal of Hydraulic Engineering*, 143(5):03117001, 2017.

[58] Florian R Menter. Review of the shear-stress transport turbulence model experience from an industrial perspective. *International journal of computational fluid dynamics*, 23(4):305–316, 2009.

[59] C. Walker, A. Manera, B. Niceno, M. Simiano, and H. M. Prasser. Steady-state rans-simulations of the mixing in a t-junction. *Nuclear Engineering and Design*, 240:2107–2115, 9 2010. ISSN 0029-5493. doi: 10.1016/J.NUCENGDES.2010.05.056.

[60] Tobias Schikarski, Marc Avila, Holger Trzenschiok, Andreas Güldenpfennig, and Wolfgang Peukert. Quantitative modeling of precipitation processes. *Chemical Engineering Journal*, 444, 9 2022. ISSN 13858947. doi: 10.1016/j.cej.2022.136195.

[61] *Transport phenomena, R. B. Bird, W. E. Stewart, and E. N. Lightfoot, John Wiley and Sons, Inc., New York(1960).*, volume 7. 6 1961. doi: 10.1002/aic.690070245.

[62] Norbert Peters. *Turbulent Combustion*. Cambridge University Press, 8 2000. ISBN 9780521660822. doi: 10.1017/CBO9780511612701.

[63] Thierry Poinsot and Denis Veynante. *Theoretical and numerical combustion*. RT Edwards, Inc., 2005.

[64] Rodney O. Fox. *Computational Models for Turbulent Reacting Flows*. Cambridge University Press, 10 2003. ISBN 9780521650496. doi: 10.1017/CBO9780511610103.

[65] Jerzy Bałdyga and John R Bourne. *Turbulent mixing and chemical reactions*. John Wiley & Sons, 1999.

[66] S. P. Burke and T. E. W. Schumann. Diffusion flames. *Industrial & Engineering Chemistry*, 20:998–1004, 10 1928. ISSN 0019-7866. doi: 10.1021/ie50226a005.

[67] HL Toor. Mass transfer in dilute turbulent and non-turbulent systems with rapid irreversible reactions and equal diffusivities. *AIChE Journal*, 8(1):70–78, 1962.

[68] Ryszard Pohorecki and Jerzy Baldyga. New model of micromixing in chemical reactors. 1. general development and application to a tubular reactor. *Industrial & engineering chemistry fundamentals*, 22(4):392–397, 1983.

[69] Rodney O Fox. On the relationship between lagrangian micromixing models and computational fluid dynamics 1, 1998.

[70] J Baldyga, W Podgorska, and R Pohorecki. Mixing-precipitation model with application to double feed semibatch precipitation. *Chemical Enqineering Science*, 50:1281–1300, 1995.

[71] D. L. Marchisio, A. A. Barresi, and R. O. Fox. Simulation of turbulent precipitation in a semi-batch taylor-couette reactor using cfd. *AIChE Journal*, 47:664–676, 3 2001. ISSN 00011541. doi: 10.1002/aic.690470314.

[72] Mohsen Shiea, Andrea Querio, Antonio Buffo, Gianluca Boccardo, and Daniele Marchisio. Cfd-pbe modelling of continuous ni-mn-co hydroxide co-precipitation for li-ion batteries. *Chemical Engineering Research and Design*, 177:461–472, 1 2022. ISSN 02638762. doi: 10.1016/j.cherd.2021.11.008.

[73] Ying Liu and R. O. Fox. Cfd predictions for chemical processing in a confined impinging-jets reactor. *AIChE Journal*, 52:731–744, 2 2006. ISSN 00011541. doi: 10.1002/aic.10633.

[74] Jerzy Bałdyga. A closure model for homogeneous chemical reactions. *Chemical Engineering Science*, 49:1985–2003, 6 1994. ISSN 00092509. doi: 10.1016/0009-2509(94)80082-0.

[75] J. Bałdyga and R. Pohorecki. Turbulent micromixing in chemical reactors — a review. *The Chemical Engineering Journal and the Biochemical Engineering Journal*, 58:183–195, 6 1995. ISSN 09230467. doi: 10.1016/0923-0467(95)02982-6.

[76] J.A. Dirksen and T.A. Ring. Fundamentals of crystallization: Kinetic effects on particle size distributions and morphology. *Chemical Engineering Science*, 46:2389–2427, 1991. ISSN 00092509. doi: 10.1016/0009-2509(91)80035-W.

[77] Gary Nichols, Stephen Byard, Mark J. Bloxham, Joanne Botterill, Neil J. Dawson, Andrew Dennis, Valerie Diart, Nigel C. North, and John D. Sherwood. A review of the terms agglomerate and aggregate with a recommendation for nomenclature used in powder and particle characterization. *Journal of Pharmaceutical Sciences*, 91:2103–2109, 10 2002. ISSN 00223549. doi: 10.1002/jps.10191.

[78] Anthony Singer, Zein Barakat, Subhra Mohapatra, and Shyam S. Mohapatra. Nanoscale drug-delivery systems, 2019.

[79] Jerzy Bałdyga. Mixing and fluid dynamics effects in particle precipitation processes. *KONA Powder and Particle Journal*, 33:127–149, 2016. ISSN 0288-4534. doi: 10.14356/kona.2016021.

[80] Ronald W. Rousseau. Crystallization processes, 2003.

[81] Alfons. Mersmann. *Crystallization technology handbook*. Marcel Dekker, 2001. ISBN 0824705289.

[82] L. Vicum, M. Mazzotti, and J. Baldyga. Applying a thermodynamic model to the non-stoichiometric precipitation of barium sulfate. *Chemical Engineering & Technology*, 26:325–333, 3 2003. ISSN 09307516. doi: 10.1002/ceat.200390050.

[83] J. Bałdyga, M. Jasińska, and W. Orciuch. Barium sulphate agglomeration in a pipe – an experimental study and cfd modeling. *Chemical Engineering & Technology*, 26:334–340, 3 2003. ISSN 09307516. doi: 10.1002/ceat.200390051.

[84] Daniele L. Marchisio, Antonello A. Barresi, and Mirko Garbero. Nucleation, growth, and agglomeration in barium sulfate turbulent precipitation. *AIChE Journal*, 48:2039–2050, 9 2002. ISSN 00011541. doi: 10.1002/aic.690480917.

[85] D. Kashchiev and G. M. van Rosmalen. Review: Nucleation in solutions revisited. *Crystal Research and Technology*, 38:555–574, 7 2003. ISSN 02321300. doi: 10.1002/crat.200310070.

[86] Piero M Armenante and Donald J Kirwan. Mass transfer to microparticles in agitated systems. *Chemical Engineering Science*, 44(12):2781–2796, 1989.

[87] Stanislav V. Sokolov, Kristina Tschulik, Christopher Batchelor-McAuley, Kerstin Jurkschat, and Richard G. Compton. Reversible or not? distinguishing agglomeration and aggregation at the nanoscale. *Analytical Chemistry*, 87(19): 10033–10039, 2015. doi: 10.1021/acs.analchem.5b02639. PMID: 26352558.

[88] Benjamin Radel, Marco Gleiß, and Hermann Nirschl. Crystal breakage due to combined normal and shear loading. *Crystals*, 12:644, 4 2022. ISSN 2073-4352. doi: 10.3390/cryst12050644.

[89] Marian von Smoluchowski. Versuch einer mathematischen theorie der koagulationskinetik kolloider lösungen. *Zeitschrift fuer physikalische Chemie*, 92: 129 – 168, 1917.

[90] P G Saffman and J S Turner. On the collision of drops in turbulent clouds. *Journal of Fluid Mechanics*, 1:16–30, 1956. ISSN 0022-1120. doi: DOI: 10.1017/S0022112056000020.

[91] J. Abrahamson. Collision rates of small particles in a vigorously turbulent fluid. *Chemical Engineering Science*, 30:1371–1379, 11 1975. ISSN 00092509. doi: 10.1016/0009-2509(75)85067-6.

[92] Jerzy Bałdyga, Grzegorz Tyl, and Mounir Bouaifi. Perikinetic and orthokinetic aggregation of small solid particles in the presence of strong repulsive forces. *Chemical Engineering Research and Design*, 136:491–501, 8 2018. ISSN 02638762. doi: 10.1016/j.cherd.2018.06.021.

[93] KO Higashitani, Kiyoyuki Yamauchi, Yoshizo Matsuno, and Gijiro Hosokawa. Turbulent coagulation of particles dispersed in a viscous fluid. *JOURNAL OF CHEMICAL ENGINEERING OF JAPAN*, 16:299–304, 1983. ISSN 0021-9592. doi: 10.1252/jcej.16.299.

[94] Gerald Wilemski. On the derivation of smoluchowski equations with corrections in the classical theory of brownian motion. *Journal of Statistical Physics*, 14:153–169, 1976. ISSN 1572-9613. doi: 10.1007/BF01011764.

[95] J. Bałdyga, M. Jasińska, and W. Orciuch. Barium sulphate agglomeration in a pipe – an experimental study and cfd modeling. *Chemical Engineering & Technology*, 26:334–340, 3 2003. ISSN 09307516. doi: 10.1002/ceat.200390051.

[96] Christian Lindenberg and Marco Mazzotti. Continuous precipitation of l-asparagine monohydrate in a micromixer: Estimation of nucleation and growth kinetics. *AIChE Journal*, 57:942–950, 4 2011. ISSN 00011541. doi: 10.1002/aic.12326.

[97] René David, Philippe Marchal, Jean Paul Klein, and Jacques Villermaux. Crystallization and precipitation engineering-iii. a discrete formulation of the agglomeration rate of crystals in a crystallization process. *Chemical Engineering Science*, 46:205–213, 1991. ISSN 00092509. doi: 10.1016/0009-2509(91)80130-Q.

[98] Caliane Bastos Borba Costa, Maria Regina Wolf Maciel, and Rubens Maciel Filho. Considerations on the crystallization modeling: Population balance solution. *Comput. Chem. Eng.*, 31:206–218, 2007.

[99] D. Randolph and A. Larson. *Theory of Particulate Processes*. Elsevier, 1971. ISBN 9780125796507. doi: 10.1016/B978-0-12-579650-7.X5001-5.

[100] Jingcai Cheng, Chao Yang, Zai-Sha Mao, and Chengjun Zhao. Cfd modeling of nucleation, growth, aggregation, and breakage in continuous precipitation of barium sulfate in a stirred tank. *Industrial & Engineering Chemistry Research*, 48:6992–7003, 8 2009. ISSN 0888-5885. doi: 10.1021/ie9004282.

[101] Mohsen Shiea, Antonio Buffo, Marco Vanni, and Daniele Marchisio. Numerical methods for the solution of population balance equations coupled with computational fluid dynamics. *Annual Review of Chemical and Biomolecular Engineering*, 11:339–366, 6 2020. ISSN 1947-5438. doi: 10.1146/annurev-chembioeng-092319-075814.

[102] Daniele L Marchisio, Jesse T Pikturna, Rodney O Fox, R Dennis Vigil, and Antonello A Barresi. Quadrature method of moments for population-balance equations. *AlChE Journal*, 49:1266–1276, 2003.

[103] Daniele L. Marchisio, R. Dennis Vigil, and Rodney O. Fox. Quadrature method of moments for aggregation-breakage processes. *J. Colloid Interface Sci.*, 258:322–334, 2 2003. ISSN 00219797. doi: 10.1016/S0021-9797(02)00054-1.

[104] Daniele L. Marchisio and Antonello A. Barresi. Cfd simulation of mixing and reaction: The relevance of the micro- mixing model. *Chemical Engineering Science*, 58:3579–3587, 2003. ISSN 00092509. doi: 10.1016/S0009-2509(03)00264-1.

[105] Vinay Kariwala, Yi Cao, and Zoltan K Nagy. Automatic differentiation based qmom for population balance equations. *IFAC Proceedings Volumes*, 43(5):397–402, 2010.

[106] G. Battaglia, S. Romano, A. Raponi, F. Volpe, L. Bellanca, M. Ciofalo, D. Marchisio, A. Cipollina, G. Micale, and A. Tamburini. Mixing phenomena in circular and rectangular cross-sectional t-mixers: Experimental and numerical assessment. *Chemical Engineering Research and Design*, 201:228–241, 2024. ISSN 0263-8762. doi: https://doi.org/10.1016/j.cherd.2023.11.056.

[107] S Wong, M Ward, and C Wharton. Micro t-mixer as a rapid mixing micromixer. *Sensors and Actuators B: Chemical*, 100:359–379, 5 2004. ISSN 09254005. doi: 10.1016/j.snb.2004.02.008.

[108] Th. Frank, C. Lifante, H.-M. Prasser, and F. Menter. Simulation of turbulent and thermal mixing in t-junctions using urans and scale-resolving turbulence models in ansys cfx. *Nuclear Engineering and Design*, 240:2313–2328, 9 2010. ISSN 00295493. doi: 10.1016/j.nucengdes.2009.11.008.

[109] J.B.W Kok and S van der Wal. Mixing in t-junctions. *Applied Mathematical Modelling*, 20:232–243, 3 1996. ISSN 0307904X. doi: 10.1016/0307-904X(95)00151-9.

[110] Solomon Bello and Seth Debrah. *Analysis of Fluid-Solid Interaction Contributing to Thermal Fatigue in T-Junction Pipes of Nuclear Power Reactors using STAR-CCM+*. PhD thesis, 07 2017.

[111] Pierre Coste, Patrick Quemere, Pierre Roubin, Philippe Emonot, Masaaki Tanaka, and Hideki Kamide. Large eddy simulation of highly fluctuational temperature and velocity fields observed in a mixing-tee experiment. *Nuclear Technology*, 164:76–88, 10 2008. ISSN 0029-5450. doi: 10.13182/NT08-A4009.

[112] Jerzy Bałdyga and Wojciech Orciuch. Some hydrodynamic aspects of precipitation. *Powder Technology*, 121:9–19, 11 2001. ISSN 00325910. doi: 10.1016/S0032-5910(01)00368-0.

[113] Allan S. Myerson, Deniz Erdemir, and Alfred Y. Lee, editors. *Handbook of Industrial Crystallization*. Cambridge University Press, 6 2019. ISBN 9781139026949. doi: 10.1017/9781139026949.

[114] R. J. Santos and M. A. Sultan. State of the art of mini/micro jet reactors. *Chemical Engineering & Technology*, 36:937–949, 6 2013. ISSN 09307516. doi: 10.1002/ceat.201200678.

[115] Joëlle Aubin, Montse Ferrando, and Vladimir Jiricny. Current methods for characterising mixing and flow in microchannels. *Chemical Engineering Science*, 65:2065–2093, 3 2010. ISSN 00092509. doi: 10.1016/j.ces.2009.12.001.

[116] Emmanuela Gavi, Daniele L. Marchisio, Antonello A. Barresi, Michael G. Olsen, and Rodney O. Fox. Turbulent precipitation in micromixers: Cfd simulation and flow field validation. *Chemical Engineering Research and Design*, 88:1182–1193, 9 2010. ISSN 02638762. doi: 10.1016/j.cherd.2010.01.025.

[117] Peicheng Luo, Haiyan Jia, Chuanxian Xin, Guozhao Xiang, Zhen Jiao, and Hua Wu. An experimental study of liquid mixing in a multi-orifice-impinging transverse jet mixer using plif. *Chemical Engineering Journal*, 228:554–564, 7 2013. ISSN 13858947. doi: 10.1016/j.cej.2013.05.051.

[118] Krzysztof Wojtas, Wojciech Orciuch, Łukasz Wysocki, and Łukasz Makowski. Modeling and experimental validation of subgrid scale scalar variance at high schmidt numbers. *Chemical Engineering Research and Design*, 123:141–151, 7 2017. ISSN 02638762. doi: 10.1016/j.cherd.2017.05.003.

[119] Haiyan Bie, Licheng Xue, Yue Wang, Zongrui Hao, Gang Liu, Yunxia Li, Zixin Lin, and Weizhong An. Effects of secondary impinging on flow features

and mixing performance in t-t jet reactors. *Chemical Engineering Journal*, 454:140368, 2 2023. ISSN 13858947. doi: 10.1016/j.cej.2022.140368.

[120] A. Mariotti, C. Galletti, E. Brunazzi, and M.V. Salvetti. Mixing sensitivity to the inclination of the lateral walls in a t-mixer. *Chemical Engineering and Processing - Process Intensification*, 170:108699, 1 2022. ISSN 02552701. doi: 10.1016/j.cep.2021.108699.

[121] Chunhui Li, Bin Wu, Junjie Zhang, and Peicheng Luo. Effect of swirling addition on the liquid mixing performance in a t-jets mixer. *Chinese Journal of Chemical Engineering*, 50:108–116, 10 2022. ISSN 10049541. doi: 10.1016/j.cjche.2022.07.008.

[122] Jason M. Gillian and Donald J. Kirwan. Identification and correlation of mixing times in opposed-jet mixers. *Chemical Engineering Communications*, 195:1553–1574, 8 2008. ISSN 0098-6445. doi: 10.1080/00986440802115614.

[123] Christian Lindenberg, Jochen Schöll, Lars Vicum, Marco Mazzotti, and Jörg Brozio. Experimental characterization and multi-scale modeling of mixing in static mixers. *Chemical Engineering Science*, 63:4135–4149, 8 2008. ISSN 00092509. doi: 10.1016/j.ces.2008.05.026.

[124] Claudio Chicchiero, Lorenzo Siconolfi, and Simone Camarri. Investigation of the symmetry-breaking instability in a t-mixer with circular cross section. *Physics of Fluids*, 32, 12 2020. ISSN 1070-6631. doi: 10.1063/5.0031924.

[125] A. Farahinia and W. J. Zhang. Numerical analysis of a microfluidic mixer and the effects of different cross-sections and various input angles on its mixing performance. *Journal of the Brazilian Society of Mechanical Sciences and Engineering*, 42:190, 4 2020. ISSN 1678-5878. doi: 10.1007/s40430-020-02275-9.

[126] M. Roudgar, E. Brunazzi, C. Galletti, and R. Mauri. Numerical study of split t-micromixers. *Chemical Engineering & Technology*, 35:1291–1299, 7 2012. ISSN 0930-7516. doi: 10.1002/ceat.201100611.

[127] Cláudio P. Fonte, M. Ashar Sultan, Ricardo J. Santos, Madalena M. Dias, and José Carlos B. Lopes. Flow imbalance and reynolds number impact on mixing in confined impinging jets. *Chemical Engineering Journal*, 260:316–330, 1 2015. ISSN 13858947. doi: 10.1016/j.cej.2014.08.090.

[128] Stephen B. Pope. *Turbulent Flows*, volume 427. Cambridge University Press, 8 2000. ISBN 9780521591256. doi: 10.1017/CBO9780511840531.

[129] E. Merzari, A. Khakim, H. Ninokata, and E. Baglietto. Toward an accurate approach for the prediction of the flow in a t-junction: Urans. *Nuclear Engineering and Technology*, 41:1191–1204, 11 2009. ISSN 1738-5733. doi: 10.5516/NET.2009.41.9.1191.

[130] Jing-Wei Zhang, Wei-Feng Li, Xin-Lei Xu, M. El Hassan, Hai-Feng Liu, and Fu-Chen Wang. Effect of geometry on engulfment flow regime in t-jet reactors. *Chemical Engineering Journal*, 387:124148, 5 2020. ISSN 13858947. doi: 10.1016/j.cej.2020.124148.

[131] C.P.M. Roelands, J.J. Derksen, J.H. ter Horst, H.J.M. Kramer, and P.J. Jansens. An analysis of mixing in a typical experimental set-up to measure nnucleation rates of precipitation processes. *Chemical Engineering & Technology*, 26: 296–303, 3 2003. ISSN 09307516. doi: 10.1002/ceat.200390045.

[132] Antonello Raponi, Salvatore Romano, Giuseppe Battaglia, Antonio Buffo, Marco Vanni, Andrea Cipollina, and Daniele Marchisio. Computational modeling of magnesium hydroxide precipitation and kinetics parameters identification. *Crystal Growth & Design*, 23:4748–4759, 7 2023. ISSN 1528-7483. doi: 10.1021/acs.cgd.2c01179.

[133] M.M.M.G.P.G. Mantilaka, H.M.T.G.A. Pitawala, D.G.G.P. Karunaratne, and R.M.G. Rajapakse. Nanocrystalline magnesium oxide from dolomite via poly(acrylate) stabilized magnesium hydroxide colloids. *Colloids and Surfaces A: Physicochemical and Engineering Aspects*, 443:201–208, 2 2014. ISSN 09277757. doi: 10.1016/j.colsurfa.2013.11.020.

[134] Gregory V. Lowry, Reghan J. Hill, Stacey Harper, Alan F. Rawle, Christine Ogilvie Hendren, Fred Klaessig, Ulf Nobbmann, Philip Sayre, and John Rumble. Guidance to improve the scientific value of zeta-potential measurements in nanoehs. *Environmental Science: Nano*, 3:953–965, 2016. ISSN 2051-8153. doi: 10.1039/C6EN00136J.

[135] J.X. Lin and L. Wang. Adsorption of dyes using magnesium hydroxide-modified diatomite. *Desalination and Water Treatment*, 8:263–271, 8 2009. ISSN 1944-3994. doi: 10.5004/dwt.2009.786.

[136] C Henrist, J.-P Mathieu, C Vogels, A Rulmont, and R Cloots. Morphological study of magnesium hydroxide nanoparticles precipitated in dilute aqueous solution. *Journal of Crystal Growth*, 249:321–330, 2 2003. ISSN 00220248. doi: 10.1016/S0022-0248(02)02068-7.

[137] George A. Parks. The isoelectric points of solid oxides, solid hydroxides, and aqueous hydroxo complex systems. *Chemical Reviews*, 65:177–198, 4 1965. ISSN 0009-2665. doi: 10.1021/cr60234a002.

[138] V.A. Phillips, J.L. Kolbe, and H. Opperhauser. Effect of ph on the growth of mg(oh)2 crystals in an aqueous environment at 60°c. *Journal of Crystal Growth*, 41:228–234, 12 1977. ISSN 00220248. doi: 10.1016/0022-0248(77)90050-1.

[139] Kefeng Tong, Xingfu Song, Guoping Xiao, and Jianguo Yu. Colloidal processing of mg(oh) 2 aqueous suspensions using sodium polyacrylate as dispersant. *Industrial & Engineering Chemistry Research*, 53:4755–4762, 3 2014. ISSN 0888-5885. doi: 10.1021/ie5002857.

[140] Antonello Raponi, Ramona Achermann, Salvatore Romano, Silvio Trespi, Marco Mazzotti, Andrea Cipollina, Antonio Buffo, Marco Vanni, and Daniele Marchisio. Population balance modelling of magnesium hydroxide precipitation: Full validation on different reactor configurations. *Chemical Engineering Journal*, 477:146540, 2023. ISSN 1385-8947. doi: https://doi.org/10.1016/j.cej.2023.146540.

[141] Georgi Kalitzin, Gorazd Medic, Gianluca Iaccarino, and Paul Durbin. Near-wall behavior of rans turbulence models and implications for wall functions. *Journal of Computational Physics*, 204:265–291, 3 2005. ISSN 00219991. doi: 10.1016/j.jcp.2004.10.018.

[142] Salvatore Romano, Giuseppe Battaglia, Simone Bonafede, Daniele Marchisio, Michele Ciofalo, Alessandro Tamburini, Andrea Cipollina, and Giorgio Micale. Experimental assessment of the mixing quality in a circular cross-sectional t-shaped mixer for the precipitation of sparingly soluble compounds. *Chemical Engineering Transactions*, 86:1165–1170, 2021. ISSN 22839216. doi: 10.3303/CET2186195.

[143] Leroy A Bromley. Thermodynamic properties of strong electrolytes in aqueous solutions. *AIChE Journal*, 19:313–320, 3 1973. ISSN 0001-1541. doi: 10.1002/aic.690190216.

[144] Hsing Yu Wang and Jeffrey D. Ward. Seeding and optimization of batch reactive crystallization. *Ind. Eng. Chem. Res.*, 54:9360–9368, 2015. ISSN 15205045. doi: 10.1021/acs.iecr.5b00185.

[145] Piotr H. Karpiński and Jerzy Bałdyga. *Precipitation processes*, pages 216–265. Cambridge University Press, 1 2019. ISBN 9781139026949. doi: 10.1017/9781139026949.008.

[146] Noriaki Kubota, Norihito Doki, Masaaki Yokota, and Akira Sato. Seeding policy in batch cooling crystallization. *Powder Technol.*, 121(1):31–38, nov 2001. ISSN 00325910. doi: 10.1016/S0032-5910(01)00371-0.

[147] Carmelo Morgante, Fabrizio Vassallo, Giuseppe Battaglia, Andrea Cipollina, Fabrizio Vicari, Alessandro Tamburini, and Giorgio Micale. Influence of operational strategies for the recovery of magnesium hydroxide from brines at a pilot scale. *Industrial & Engineering Chemistry Research*, 61(41):15355–15368, 2022. doi: 10.1021/acs.iecr.2c02935.

[148] Antonello Raponi and Daniele Marchisio. Deep learning for kinetics parameters identification: A novel approach for multi-variate optimization. *Chemical Engineering Journal*, page 151149, 2024. ISSN 1385-8947. doi: https://doi.org/10.1016/j.cej.2024.151149.

[149] A. Guisasola, J.A. Baeza, J. Carrera, G. Sin, P.A. Vanrolleghem, and J. Lafuente. The influence of experimental data quality and quantity on parameter estimation accuracy. *Education for Chemical Engineers*, 1:139–145, 1 2006. ISSN 17497728. doi: 10.1205/ece06016.

[150] Mehrdad Rezaie, Keyvan karamnejadi azar, Armin kardan sani, Ehsan Akbari, Noradin Ghadimi, Navid Razmjooy, and Mojtaba Ghadamyari. Model parameters estimation of the proton exchange membrane fuel cell by a modified golden jackal optimization. *Sustainable Energy Technologies and Assessments*, 53:102657, 10 2022. ISSN 22131388. doi: 10.1016/j.seta.2022.102657.

[151] Yajie Zhang, Ye Tian, and Xingyi Zhang. Improved sparseea for sparse large-scale multi-objective optimization problems. *Complex & Intelligent Systems*, 9:1127–1142, 4 2023. ISSN 2199-4536. doi: 10.1007/s40747-021-00553-0.

[152] Guodong Ma, Hui Lin, Wenhui Jin, and Daolan Han. Two modified conjugate gradient methods for unconstrained optimization with applications in image restoration problems. *Journal of Applied Mathematics and Computing*, 68: 4733–4758, 12 2022. ISSN 1598-5865. doi: 10.1007/s12190-022-01725-y.

[153] Abdulkarim Hassan Ibrahim, Poom Kumam, Ahmad Kamandi, and Auwal Bala Abubakar. An efficient hybrid conjugate gradient method for unconstrained optimization. *Optimization Methods and Software*, 37:1370–1383, 7 2022. ISSN 1055-6788. doi: 10.1080/10556788.2021.1998490.

[154] Marcio Schwaab, Evaristo Chalbaud Biscaia Jr., José Luiz Monteiro, and José Carlos Pinto. Nonlinear parameter estimation through particle swarm optimization. *Chemical Engineering Science*, 63:1542–1552, 3 2008. ISSN 00092509. doi: 10.1016/j.ces.2007.11.024.

[155] Ahmed G. Gad. Correction to: Particle swarm optimization algorithm and its applications: A systematic review. *Archives of Computational Methods in Engineering*, 30:3471–3471, 6 2023. ISSN 1134-3060. doi: 10.1007/s11831-022-09762-3.

[156] Yilin Chen, Zhi Ye, Bo Gao, Yiqi Wu, Xiaohu Yan, and Xiangyun Liao. A robust adaptive hierarchical learning crow search algorithm for feature selection. *Electronics*, 12:3123, 7 2023. ISSN 2079-9292. doi: 10.3390/electronics12143123.

[157] Vijendra Kumar and S. M. Yadav. A state-of-the-art review of heuristic and metaheuristic optimization techniques for the management of water resources. *Water Supply*, 22:3702–3728, 4 2022. ISSN 1606-9749. doi: 10.2166/ws.2022.010.

[158] Bara'a A. Attea, Amenah D. Abbood, Ammar A. Hasan, Clara Pizzuti, Mayyadah Al-Ani, Suat Özdemir, and Rawaa Dawoud Al-Dabbagh. A review of heuristics and metaheuristics for community detection in complex networks: Current usage, emerging development and future directions. *Swarm and Evolutionary Computation*, 63:100885, 6 2021. ISSN 22106502. doi: 10.1016/j.swevo.2021.100885.

[159] James Kennedy and Russell Eberhart. Particle swarm optimization. In *Proceedings of ICNN'95-international conference on neural networks*, volume 4, pages 1942–1948. IEEE, 1995.

[160] Fude Duan, Fei Song, Sainan Chen, Majid Khayatnezhad, and Noradin Ghadimi. Model parameters identification of the pemfcs using an improved design of crow search algorithm. *International Journal of Hydrogen Energy*, 47: 33839–33849, 9 2022. ISSN 03603199. doi: 10.1016/j.ijhydene.2022.07.251.

[161] Indranil Pan, Lachlan R. Mason, and Omar K. Matar. Data-centric engineering: integrating simulation, machine learning and statistics. challenges and opportunities. *Chemical Engineering Science*, 249:117271, 2 2022. ISSN 00092509. doi: 10.1016/j.ces.2021.117271.

[162] Alexander I. J. Forrester, András Sóbester, and Andy J. Keane. *Engineering Design via Surrogate Modelling*. Wiley, 7 2008. ISBN 9780470060681. doi: 10.1002/9780470770801.

[163] M Bevacqua, F Vassallo, A Cipollina, G Micale, A Tamburini, M Papapetrou, and F Vicari. Reattore e processo di precipitazione di un prodotto solido. *Application IT 102021000012473*, 202, 2021.

Appendix A

A.1 Modelling of fast and irreversible reactions

The description of a fast and irreversible reaction can be addressed by combining the mixture fraction and its variance through a Probability Density Function (PDF). Once a PDF is assumed (for this thesis a β-PDF was used), it is easy to compute the corresponding reactant concentration given certain mixture fractions and variance values (calculated through their transport equations [Eqs. 2.12 and 2.14]). For a reaction of type A + B $\rightarrow$ P, assuming a Reynolds-averaged mixture fraction equal to 0 (1) for pure A (B), the concentrations can be expressed as follows:

$$\begin{aligned}
\bar{c}_{\mathrm{A}} &= \int_0^1 (c_{\mathrm{A}}\beta)(\alpha)\mathrm{d}\alpha \\
&= \frac{c_{\mathrm{A}}^{(\mathrm{in})}}{B(n,w)\alpha_s}\left[\alpha_s \int_0^{\alpha_s} \alpha^{n-1}(1-\alpha)^{w-1}\mathrm{d}\alpha - \int_0^{\alpha_s} \alpha^{n}(1-\alpha)^{w-1}\mathrm{d}\alpha\right] \\
&= \frac{c_{\mathrm{A}}^{(\mathrm{in})}}{B(n,w)\alpha_s}[\alpha_s I(n,w)B(n,w) - I(n+1,w)B(n+1,w)]
\end{aligned} \tag{A.1}$$

$$\begin{aligned}
\bar{c}_{\mathrm{B}} &= \int_0^1 (c_{\mathrm{B}}\beta)(\alpha)\mathrm{d}\alpha \\
&= \frac{c_{\mathrm{B}}^{(\mathrm{in})}}{B(n,w)(1-\alpha_s)}\left[\int_{\alpha_s}^1 \alpha^{n-1}(1-\alpha)^{w-1}\mathrm{d}\alpha - \alpha_s\int_{\alpha_s}^1 \alpha^{n-1}(1-\alpha)^{w-1}\mathrm{d}\alpha\right] \\
&= \frac{c_{\mathrm{B}}^{(\mathrm{in})}}{B(n,w)(1-\alpha_s)}[B(n+1,w)(1-I(n+1,w)) - \alpha_s B(n,w)(1-I(n,w))] \qquad \text{(A.2)}
\end{aligned}$$

$$\begin{aligned}
\bar{c}_{\mathrm{P}} &= \int_0^1 (c_{\mathrm{P}}\beta)(\alpha)\mathrm{d}\alpha \\
&= \int_0^{\alpha_s} c_{\mathrm{B}}^{(\mathrm{in})}\alpha\frac{\alpha^{n-1}(1-\alpha)^{w-1}}{B(n,w)}\mathrm{d}\alpha + \int_{\alpha_s}^1 c_{\mathrm{B}}^{(\mathrm{in})}\alpha_s\frac{(\alpha-1)\alpha^{n-1}(1-\alpha)^{w-1}}{B(n,w)}\mathrm{d}\alpha \\
&= \frac{c_{\mathrm{B}}^{(\mathrm{in})}\alpha_s}{B(n,w)(\alpha_s-1)}\left[\int_{\alpha_s}^1 \alpha^{n}(1-\alpha)^{w-1}\mathrm{d}\alpha - \int_{\alpha_s}^1 \alpha^{n-1}(1-\alpha)^{w-1}\mathrm{d}\alpha\right] \\
&\quad + \frac{c_{\mathrm{B}}^{(\mathrm{in})}}{B(n,w)}\int_0^{\alpha_s}\alpha^{n}(1-\alpha)^{w-1}\mathrm{d}\alpha \\
&= \frac{c_{\mathrm{B}}^{(\mathrm{in})}}{B(n,w)}I(n+1,w)B(n+1,w) \\
&\quad + \frac{c_{\mathrm{B}}^{(\mathrm{in})}\alpha_s}{B(n,w)(\alpha_s-1)}[B(n+1,w)(1-I(n+1,w)) - B(n,w)(1-I(n,w))] \qquad \text{(A.3)}
\end{aligned}$$

A.2 Product Difference algorithm

To explain the PD algorithm the definition of the matrix **P** is provided:

$$P_{i,1} = \delta_{i1} \qquad i \in [1,...,2N+1] \ , \qquad \text{(A.4)}$$

$$P_{i,2} = (-1)^{i-1}m_{i-1} \qquad i \in [1,...,2N+1] \ . \qquad \text{(A.5)}$$

The other components are calculated as:

$$\begin{aligned}
P_{i,j} = P_{1,j-1}P_{i+1,j-2} - P_{i,j-2}P_{i+1,j-1} \qquad & i \in [1,...,2N+2-j] \\
& j \in [3,...,2N+1]
\end{aligned} \qquad \text{(A.6)}$$

At this point, we define a vector g_i starting from $\mathbf{P}$, where $g_1 = 0$ and

$$g_i = \frac{P_{1,i+1}}{P_{1,i}P_{1,i-1}} \qquad i \in [2, ..., 2N] \tag{A.7}$$

from which a symmetric tridiagonal matrix is defined. The elements on the diagonal are defined as:

$$a_i = g_{2i} + g_{2i-1} \qquad i \in [1, ..., 2N-1] \tag{A.8}$$

while the off-diagonal elements are defined as:

$$b_i = -\sqrt{g_{2i+1} + g_{2i-1}} \qquad i \in [1, ..., 2N-2] \ . \tag{A.9}$$

This procedure transforms an ill-conditioned problem (finding the roots of a polynomial expression) into a well-conditioned one: finding the coordinates of interpolation points from the eigenvalues of this matrix and the weights from the eigenvectors $\mathbf{v}_j$:

$$w_j = m_0 v_{j1}^2 \ . \tag{A.10}$$

A.3 Adaptive Wheeler Algorithm

The coefficients, in the case of the Wheeler algorithm, are calculated based on the definition of modified moments:

$$\nu_k = \int \pi_k(\xi) n(\xi) \mathrm{d}\xi, \ \ k = 0, 1, \ldots 2N-1 \ . \tag{A.11}$$

It is also assumed that $\pi_k(\xi)$ satisfies the following relation:

$$\pi_{-1}(\xi) = 0 \tag{A.12}$$

$$\pi_0(\xi) = 1 \tag{A.13}$$

$$\pi_{\alpha+1}(\xi) = (\xi - a'_\alpha)\pi_\alpha(\xi) - b'_\alpha \pi_{\alpha-1}(\xi) \tag{A.14}$$

where a'_α and b'_α are known. Wheeler thus developed an algorithm for calculating the coefficients of the Jacobian matrix based on the definition of $\sigma_{\alpha,\beta}$:

$$\sigma_{\alpha,\beta} = \int n(\xi)\pi_\alpha(\xi)\pi_\beta(\xi)\mathrm{d}\xi, \ \ \alpha, \beta \geq 1 \ . \tag{A.15}$$

These quantities are calculated starting from the following initialization:

$$\sigma_{-1,\alpha} = 0 \; \alpha = 1, 2, \cdots 2N_q - 2 \tag{A.16}$$

$$\sigma_{0,\alpha} = \nu_\alpha \;\; \alpha = 0, 1, \cdots 2N_q - 1 \tag{A.17}$$

$$\alpha_0 = \alpha'_0 + \frac{\nu_1}{\nu_0} \tag{A.18}$$

$$b_0 = 0 \tag{A.19}$$

Finally, the coefficients of the Jacobian matrix are calculated as follows:

$$a_\alpha = a'_\alpha - \frac{\sigma_{\alpha-1,\alpha}}{\sigma_{\alpha-1,\alpha-1}} + \frac{\sigma_{\alpha,\alpha+1}}{\sigma_{\alpha,\alpha}} \tag{A.20}$$

$$b_\alpha = \frac{\sigma_{\alpha,\alpha}}{\sigma_{\alpha-1,\alpha-1}} \;\; . \tag{A.21}$$

From this matrix, it is possible to calculate the weights and nodes of the quadrature formula.

Appendix B

B.1 Bromley's activity coefficient

At the beginning of the activity calculation for a solute in multi-component solution indexes must be fixed and used for related equations. In this regard, since and OH^- ions are needed for supersaturation, the following indexes were given:

- Mg^{2+} index: 1
- Na^{+} index: 3
- OH^{-} index: 2
- Cl^{-} index: 4

Thus, following the above-mentioned steps, multi-component solution parameters were calculated using these equations:

$$F_1 = Y_{21}\log\left(\gamma_{12}^0\right) + Y_{41}\log\left(\gamma_{14}^0\right) + \frac{A_\gamma I^{0.5}}{1+I^{0.5}}\left[Z_1Z_2Y_{21} + Z_1Z_4Y_{41}\right] \tag{B.1}$$

$$F_2 = X_{12}\log\left(\gamma_{12}^0\right) + X_{32}\log\left(\gamma_{32}^0\right) + \frac{A_\gamma I^{0.5}}{1+I^{0.5}}\left[Z_1Z_2X_{12} + Z_3Z_2X_{32}\right] \tag{B.2}$$

where odd indexes refer to cations and even ones to anions, $A_\gamma = 0.511\sqrt{\frac{\text{kg}}{\text{mol}}}$ and I is the solution ionic strength calculated as:

$$I = \frac{1}{2}\sum_i c_i Z_i^2 \tag{B.3}$$

Here, c_i is the concentration of the i^{th} ions in the solution. Moreover, the parameters needed have this form:

$$Y_{i1} = \left(\frac{Z_i + Z_1}{2}\right)^2 \frac{m_i}{I} \tag{B.4}$$

$$X_{j2} = \left(\frac{Z_2 + Z_j}{2}\right)^2 \frac{m_j}{I} \tag{B.5}$$

m_i represents the molality of the i^{th} ion, and $\log(\gamma_{ij}^0)$ is the ten-based logarithm of the activity coefficient of the pseudo-solution. This pseudo-solution has the same ionic strength as the multi-component one but considers only the i-j ions pair.

$$\log(\gamma_{ij}^0) = -\frac{A_\gamma |Z_i Z_j| I^{0.5}}{1 + I^{0.5}} + \frac{(0.06 + 0.6B)|Z_i Z_j| I}{(1 + \frac{1.5}{|Z_i Z_j| I})^2} + BI \tag{B.6}$$

B is an empirical parameter which can be calculated or found in the literature [143]. For $MgCl_2$, NaOH, and NaCl, B values from the table were used, while for $Mg(OH)_2$, the B value was estimated using the Bromley correlation:

$$B = B_{\text{cation}} + B_{\text{anion}} + \delta_{\text{cation}} \delta_{\text{cation}} \tag{B.7}$$

where B_{cation}, B_{anion}, δ_{cation}, and δ_{anion} are values obtained from literature tables. Eventually, concluding with the three steps list, it is possible to evaluate $\log(\gamma_{12})$ for $Mg^{2+} - OH^-$ in the considered multi-component solution with the equation:

$$\log(\gamma_\pm) = -\frac{A_\gamma \left(\frac{\sum_i \nu_i Z_i^2}{\nu}\right) I^{0.5}}{1 + I^{0.5}} + \frac{1}{\nu} \sum_i \nu_i F_i \tag{B.8}$$

where $\nu = \sum_i \nu_i$. This general form is simplified because the i index refers only to the ions generated by the salt for which activity is required. In this case, $i = 1, 2$ refers to Mg^{2+} and OH^- ions. Therefore, in the present work, it results in the equation:

$$\log(\gamma_{12}) = -\frac{A_\gamma (\nu_1 Z_1^2 + \nu_2 Z_2^2) I^{0.5}}{1 + I^{0.5}} + \frac{1}{\nu}(\nu_1 F_1 + \nu_2 F_2) \tag{B.9}$$

B.2 Micro-mixing modelling

As a test, we turned off the variance calculation in our model, effectively assuming instantaneous mixing and precipitation upon entering the T-mixers. However, the predictions for mean particle sizes based on this assumption were off, as shown in Figure B.1:

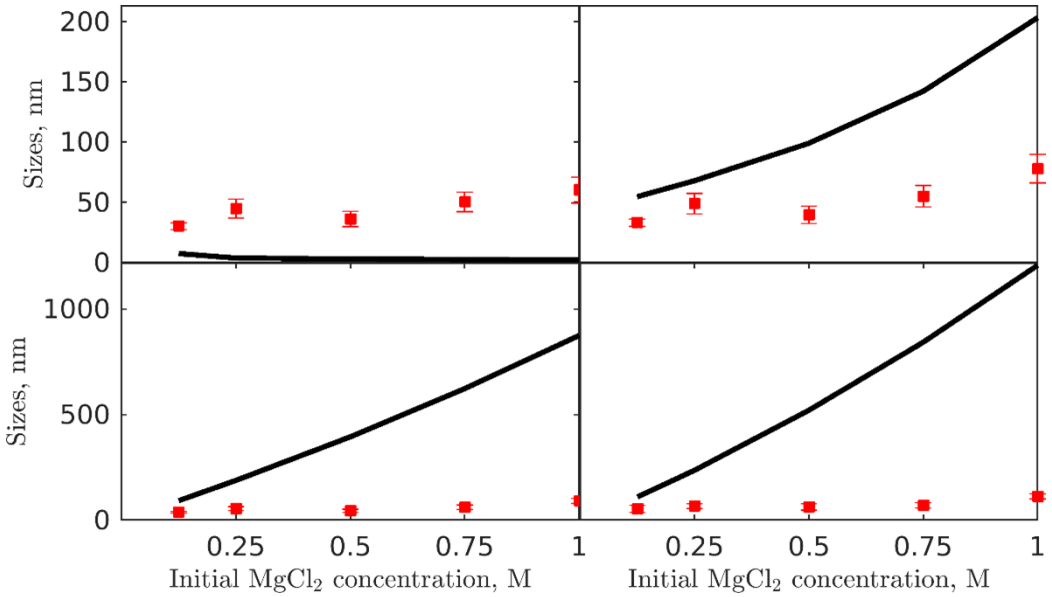

Figure B.1 Characteristic sizes, from left to right and top to bottom, d_{10}, d_{21}, d_{32}, d_{43}, derived from the measured PSD and predicted by the model. Comparison between the model's predictions using the inferred kinetics parameters set, deactivating the micro-mixing model, and the experimental data (dataset #1).

The predictions failed to capture the correct values and trends observed in experimental data. We further understood the importance of the micro-mixing model by comparing the supersaturation evolution predicted by the model both with and without the micro-mixing, as shown in Figure B.2. Only when accounting for the micro-mixing (Figure B.2, *top*) the correct trend was observed, with supersaturation first generated by mixing and then consumed by precipitation. On the other hand, when micro-mixing was neglected (Figure B.2, *bottom*), precipitation started immediately, resulting in larger supersaturation levels.

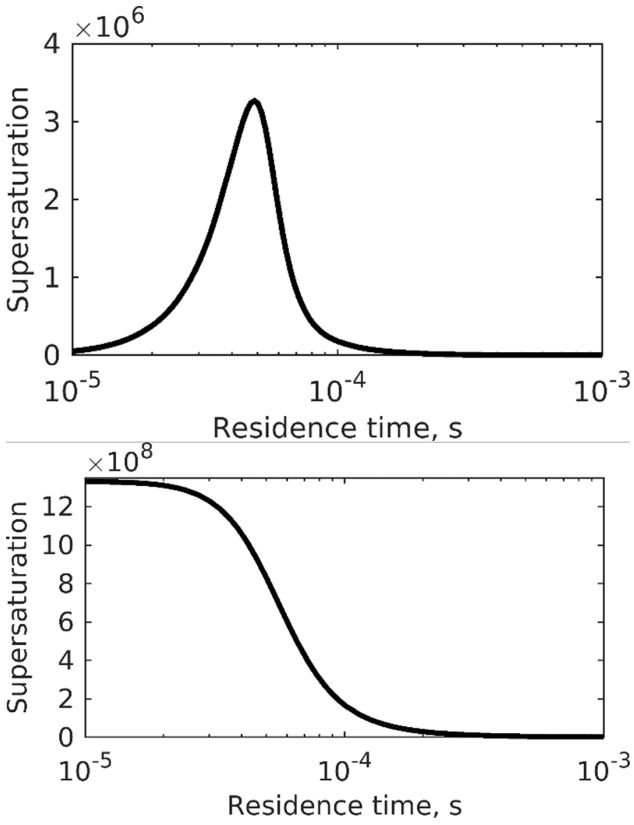

Figure B.2 Supersaturation profile obtained by employing the micro-mixing model (*top*). Supersaturation profile obtained without employing the micro-mixing model (*bottom*).

We also optimized the model parameters by fitting the experimental data without the micro-mixing model. Despite having the same number of parameters as the full model, the resulting set was unable to reproduce the experimental trends shown in Figure B.3:

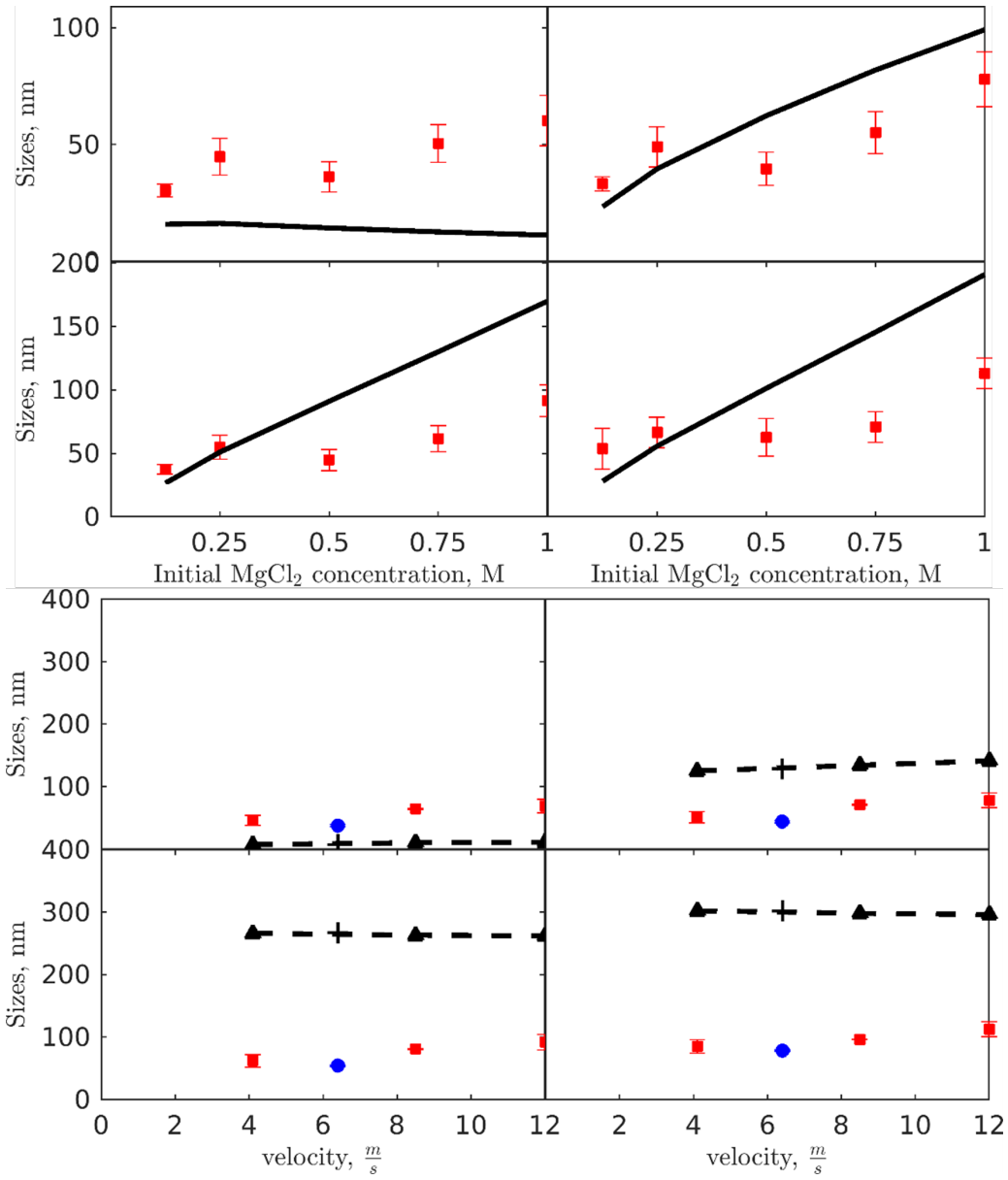

Figure B.3 Characteristic sizes, from left to right and top to bottom, d_{10}, d_{21}, d_{32}, d_{43}, derived from the measured PSD and predicted by the model. Comparison between model (without micro-mixing) outcome and experimental data used for fitting (dataset #1, *top*). Comparison between model predictions and experimental data used for testing (dataset #2, *bottom*). Effect of velocity on the PSDs in two different systems. Experimental results in the T_{2mm}-mixer (red squares) (i), experimental results in the T_{3mm}-mixer (blue dot) (ii), simulations for the T_{2mm}-mixer (dashed line) (iii), computational prediction for the T_{3mm}-mixer (cross marker) (iv)

We observed significant differences in all the parameters (Table B.1), especially A_1, which is involved in the homogeneous nucleation rate. The fact that A_1 decreased by three orders of magnitude, roughly corresponding to the increase in supersaturation shown in Figure B.2, highlights the crucial role of micro-mixing in our description.

Parameter	A_1	A_2	B_1	B_2	k_g	g	C_1	A_p
Set	10^{23}	10^{15}	315	50	$10^{-12.2}$	1.1	4.4	2.67

Table B.1 The optimal set of parameters obtained from the comparison between the model without micro-mixing and experimental data (dataset #1).

B.3 Computational Fluid Dynamics Simulations

CFD simulations might be used to estimate the mixing time and the Kolmogorov timescale, which are important parameters in predicting the particle size distribution.

$$\left(\bar{u}\frac{\mathrm{d}\bar{\alpha}'^2}{\mathrm{d}y}\right) = -\frac{C_\phi}{2}\frac{\varepsilon(y)}{k(y)}\bar{\alpha}'^2 \tag{B.10}$$

$$\beta_{ij}^{(\mathrm{turb})} = \sqrt{\frac{8\pi}{15}}\sqrt{\frac{\varepsilon}{\nu}}\left(\frac{L_i + L_j}{2}\right)^3 \tag{B.11}$$

The mixing time is the time required for two fluids to mix, and it is proportional to the ratio between the turbulent kinetic energy (k) and the turbulent dissipation rate (ε) (Eq. B.10). The Kolmogorov timescale is the smallest timescale at which energy is dissipated in a turbulent flow, and it is proportional to the square root of the kinematic viscosity (ν) divided by the turbulent dissipation rate (Eq. B.11). These two parameters affect the degree of mixing, which in turn affects all the precipitation phenomena, and therefore, the resulting particle size distribution. While it is true that mixing time can be estimated using empirical correlations, such as those discussed in our previous [11], the accuracy of the estimates for the ε value may not always be high. For instance, it could be possible to estimate the ε value by passing through the pressure drops. Nevertheless, empirical correlations would not provide a detailed estimation of pressure drops, especially those due to the impingement between fluids.

In this case, an underestimate of the ε value, could lead to a quite important deviation of the model predictions as shown in Figure B.4.

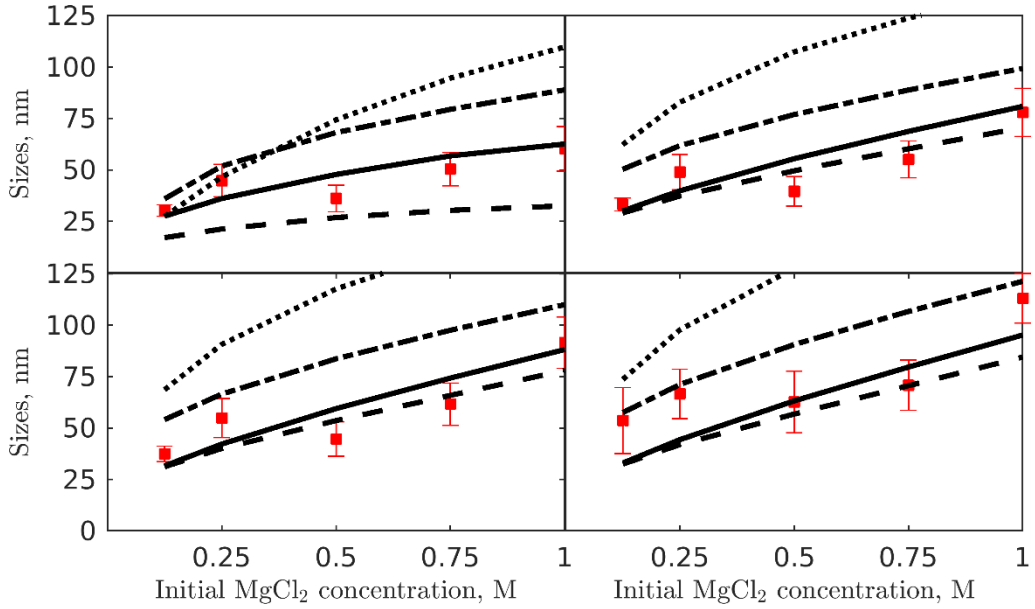

Figure B.4 Characteristic sizes, from left to right and top to bottom, d_{10}, d_{21}, d_{32}, d_{43}, derived from the measured PSD and predicted by the model. Model predictions at different values (constants) of ε. The solid line refers to the model with the integration of the CFD component. The dashed line refers to the model with a constant ε value of $10^5\,\mathrm{m}^2/\mathrm{s}^3$. The dash-dotted line refers to the model with a constant ε value of $10^3\,\mathrm{m}^2/\mathrm{s}^3$. The dotted line refers to the model with a constant ε value of $10\,\mathrm{m}^2/\mathrm{s}^3$.

On the other hand, CFD simulations provide a more comprehensive understanding of the mixing process and can account for the effect of various parameters, such as fluid properties, mixer geometry, and flow rates, on the turbulence characteristics. Therefore, although other methods may be used to estimate the mixing time and turbulence parameters, CFD simulations remain a valuable tool for obtaining reliable and comprehensive information on the mixing process.

B.4 Model parameters identification

A constrained optimization of the 8 model parameters was conducted by comparing the model outcomes with experimental data. The experimental data were obtained using the two different setups (T- and Y-mixer), which allowed us to generate 14

PSDs. From each PSD, we calculated four characteristic sizes (d_{10}, d_{21}, d_{32}, d_{43}), leading to a total of 56 experimental data points. We utilized 5 PSDs (equivalent to 20 experimental data points) obtained using the T-mixer to examine the influence of $MgCl_2$ concentration. These experimental data served as the tuning data set. Additionally, 3 more PSDs (equivalent to 12 experimental data points) from the T-mixer setup were used to validate the model's performance under varying flow rates. In this contribution, we extend our analysis by testing the model's predictive capability with a different system, namely the Y-mixer, and a broader range of concentrations that were not included in the tuning dataset. For this purpose, we utilized 6 PSDs (equivalent to 24 experimental data points). It is important to notice that we used all the experimental data points during the tuning, validation, and predictive capability assessments. The influence of the initial concentration of MgCl2 on the characteristic sizes is shown in the Figure B.5 for the T-mixer and in Figure B.6 for the Y-mixer:

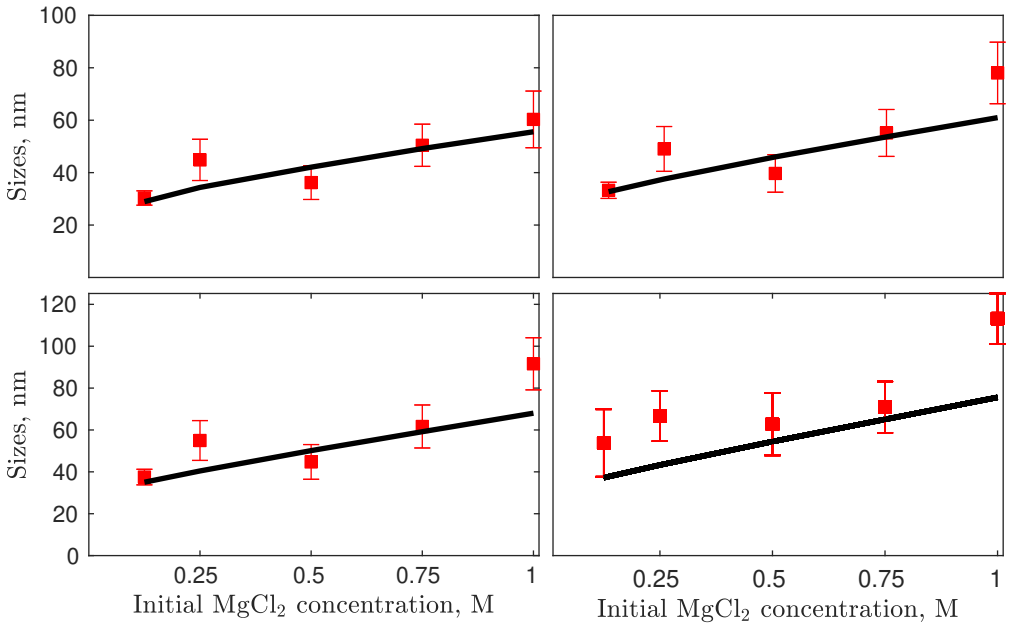

Figure B.5 Experimental sizes vs. model outcomes (T-mixer): d_{10} (top – left), d_{21} (top – right), d_{32} (bottom – left), d_{43} (bottom – right)

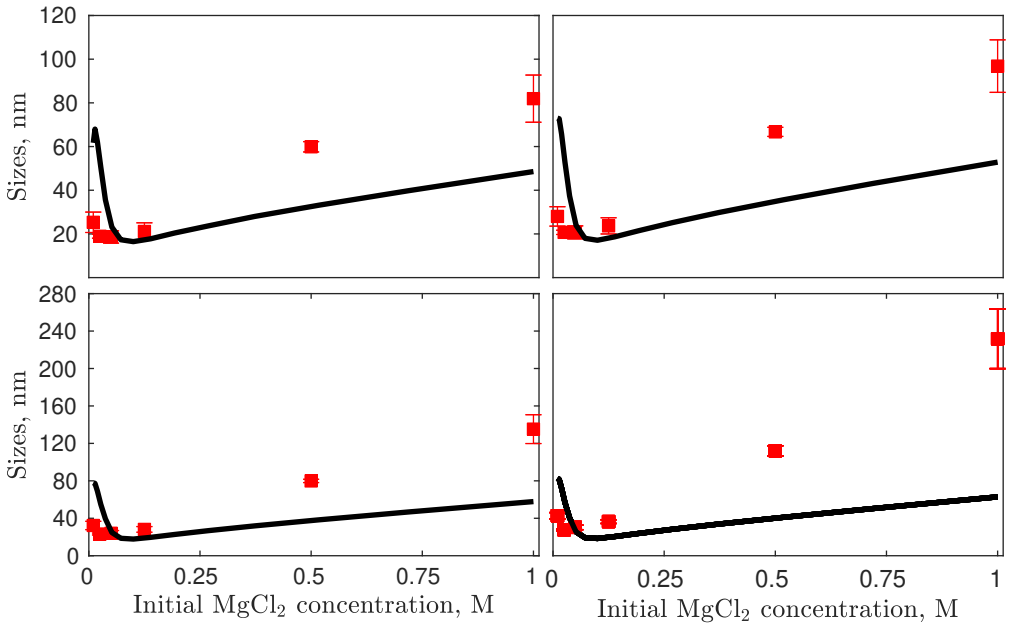

Figure B.6 Experimental sizes vs model outcomes (Y-mixer): d_{10} $(\text{top}-\text{left})$, d_{21} $(\text{top}-\text{right})$, d_{32} $(\text{bottom}-\text{left})$, d_{43} $(\text{bottom}-\text{right})$

However, for clarity and focus, we have chosen to report and discuss the results primarily based on the d_{10} characteristic size.

B.5 Confidence interval and simulation stability

In the process of parametric identification, it is advisable to give a first-attempt estimate of the confidence interval for each parameter. Indeed, it should be remembered that there are no rigorous methods for identifying this range but only rules of thumb. In this work, therefore, we chose to run a statistically significant number of simulations (i.e., 25) for each concentration by randomly varying the value of the i-th parameter between $\pm$ 5 % of the mean value (i.e., for the i-th parameter is the value given in Tables 2 and 3 reported in the manuscript):

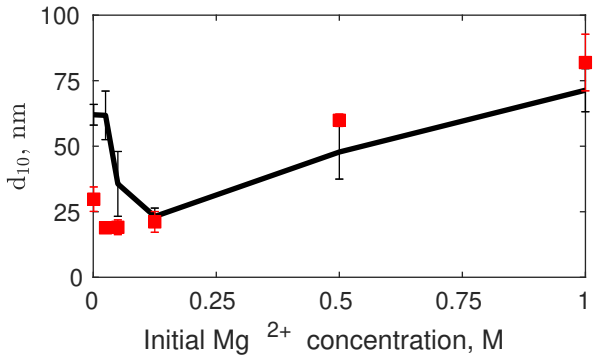

Figure B.7 d_{10} mean trend (solid black line) and d_{10} standard deviation (black bars)

Figure B.7 shows the confidence interval (in terms of the standard deviation of the 25 simulations run) for the model with no modifications.

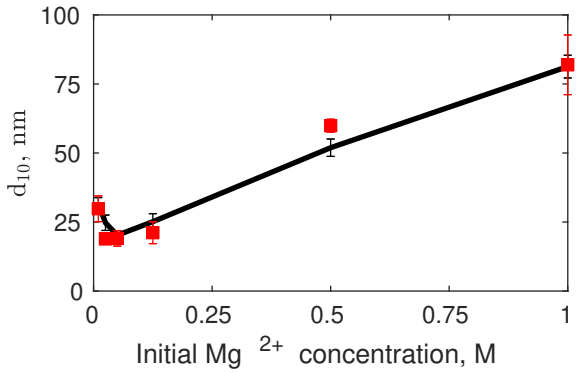

Figure B.8 d_{10} mean trend (solid black line) and d_{10} standard deviation (black bars). Simulations are run using the novel correction factor.

On the other hand, Figure B.8 shows the confidence interval (in terms of the standard deviation of the 25 simulations run) for the model employing the novel correction factor. In the first case (Figure B.7) we see that a variation of $\pm$ 5 % has a fairly significant impact while in the second Figure B.8) such variation is less significant resulting in a numerically more stable pattern.

B.6 Aggregation contribution

Figure B.9 can be used to indirectly analyze the effect of aggregation efficiency. It shows an additional d_{10} trend as a function of the initial $MgCl_2$ concentration. The

orange line represents the d_{10} trend that 'particles' would have if the C_1 parameter were halved. A comparison of the green and orange lines shows that parameter C_1 only contributes to the downward shift of d_{10} as the collision frequency decreases and it does not change the trend (i.e., the minimum is preserved). It follows that the collision frequency modulates the intensity of aggregation, and the aggregation efficiency is responsible for the occurrence of the minimum.

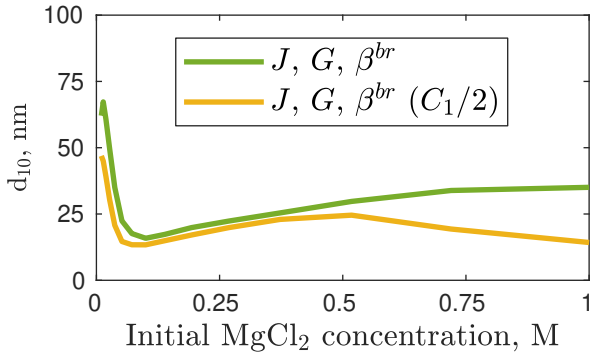

Figure B.9 d_{10} trends as a function of the initial $MgCl_2$ concentration neglecting the turbulent contribution of aggregation.

B.7 Turbulent properties

Computational fluid dynamics (CFD) simulations were used to extract turbulent parameters, such as the turbulent kinetic energy (k) and the turbulent dissipation rate (ε), which are needed for the prediction of the final particle size distribution (PSD) of $Mg(OH)_2$. A RANS simulation approach can be adopted to describe turbulence, and the standard $k-\varepsilon$ turbulence model was used. In RANS simulations, flow field and turbulent properties are strongly related. The velocity is chosen based on the experimental operative conditions. Orlewski and Mazzotti [41] performed a preliminary mesh study to ensure a solution independent of the mesh. It resulted in a final total cell number mesh of around 93000. Since spatial variations exist along the mixing channel coordinates, k and ε profiles are extracted. For this, circular cross-sections were taken, starting from the mixing point down the mixing channel. The corresponding values were averaged along the cross-section surface at a given mixing channel coordinate. Averaged profiles are reported in Figure B.10

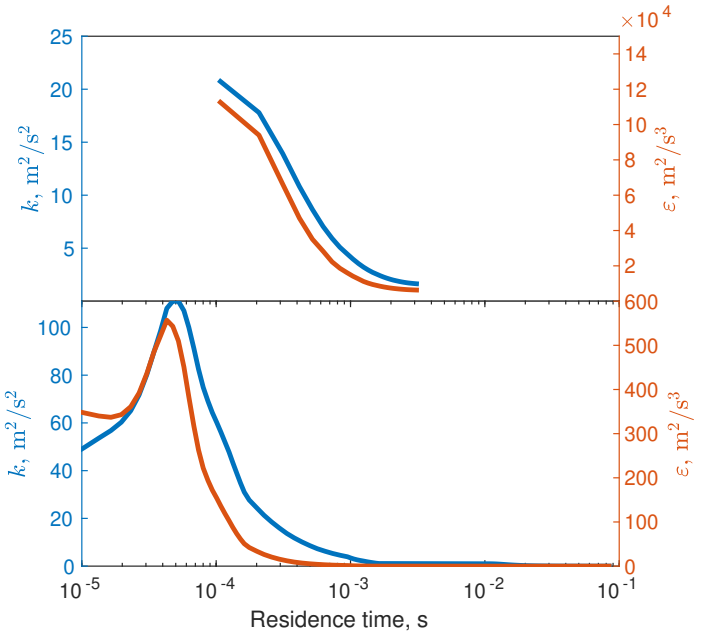

Figure B.10 The averaged $k-\varepsilon$ profiles extracted from CFD simulations are shown for the T-mixer setup (top) and the Y-mixer setup (bottom).

The turbulent properties in the T-mixer are one order of magnitude lower than those in the Y-mixer. Indeed, this justifies that the dissipation of variance is slower in the T-mixer than in the Y-mixer. Note that the flow and turbulent fields affect both the molecular processes (i.e., nucleation and growth) as well as the secondary process (i.e., aggregation) considered here. Thus, by comparing different systems, one can investigate the effect of the fluid flow and compare the T-mixer with the Y-mixer.

B.8 Deep learning training

The neural network used in this contribution is a deep learning fully-connected neural network. The architecture consists of an input, three hidden, and an output layer. A schematic representation is shown in Figure B.11

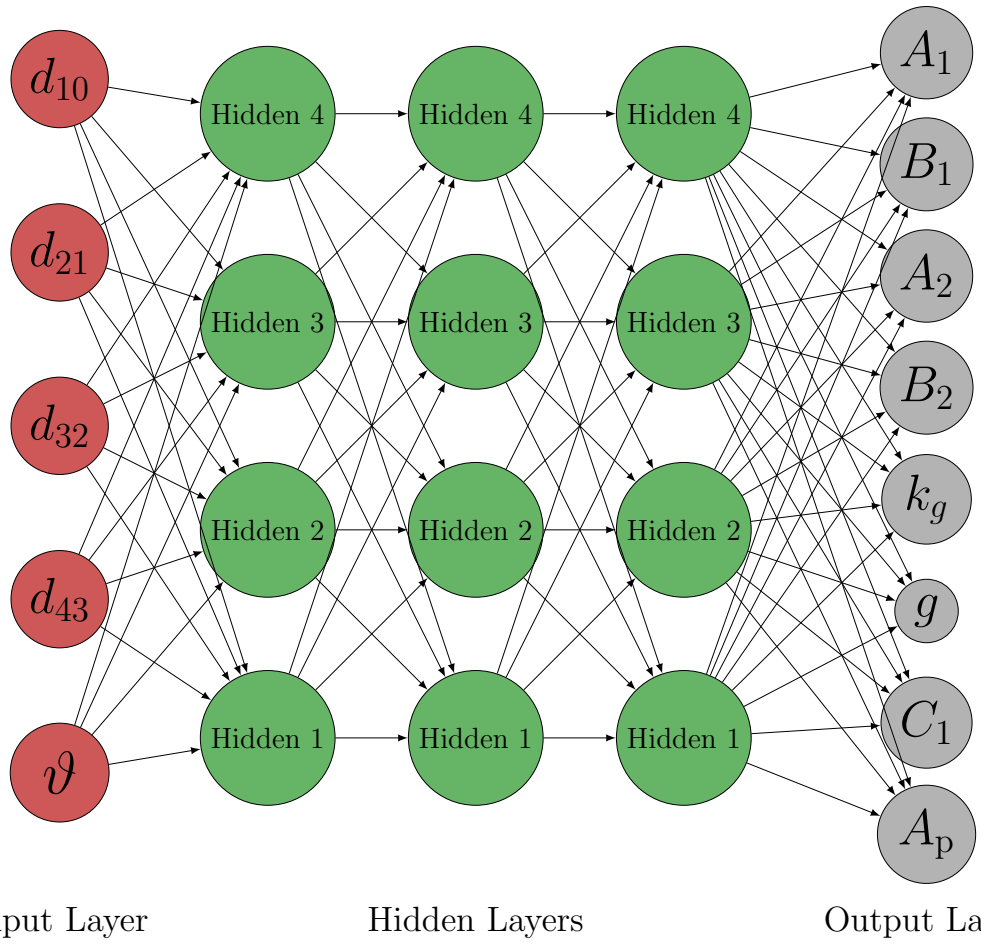

Figure B.11 Schematic representation of the Mirror Model focusing on inputs and outputs

The input layer has five neurons: four are dedicated to the characteristic sizes ($d_{10}, d_{21}, d_{32}, d_{43}$) and one to the initial Mg^{2+} concentration (ϑ). The output layer has eight neurons dedicated to the kinetics parameters ($A_1, A_2, B_1, B_2, k_g, g, C_1, A_\mathrm{p}$). Four combinations of hidden layers were explored: (1) 32-32, (2) 32-64-32, (3) 64-128-64, (4) 64-128-128-64 (the x-axis of each parameter in Figure B.12). Four dataset sizes were explored: (a) 100, (b) 200, (c) 300 and (d) 400 (the four subplots in Figure B.12) simulations with a 0.8/0.2 (training/testing) ratio.

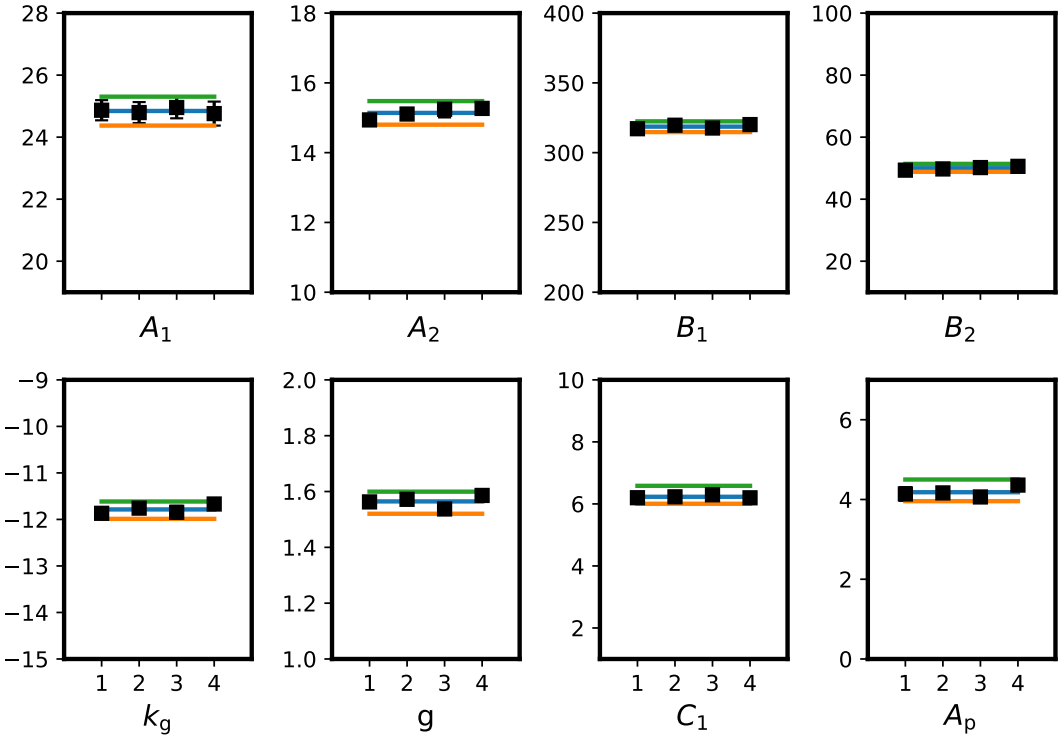

(a) 100 simulations

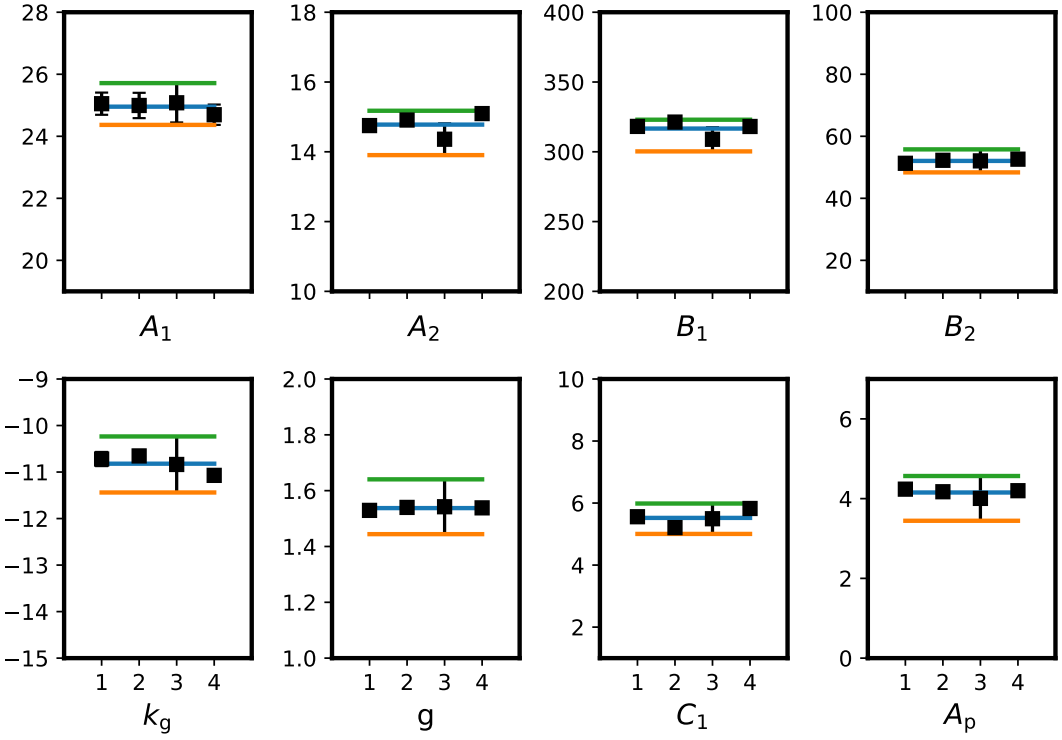

(b) 200 simulations

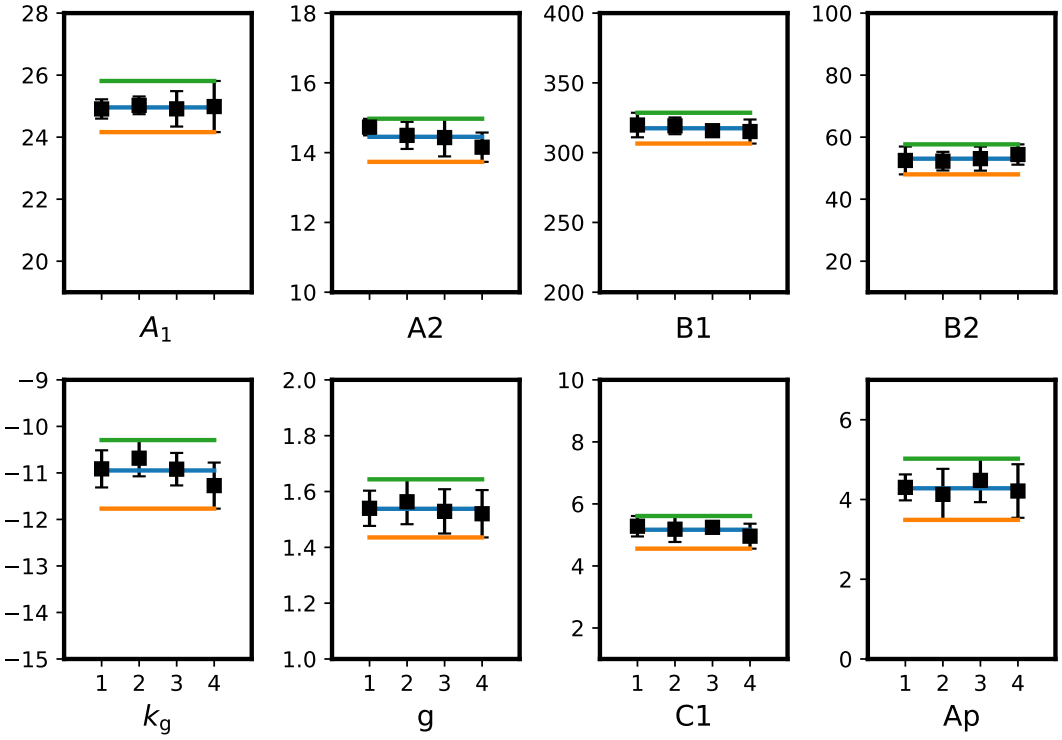

(c) 300 simulations

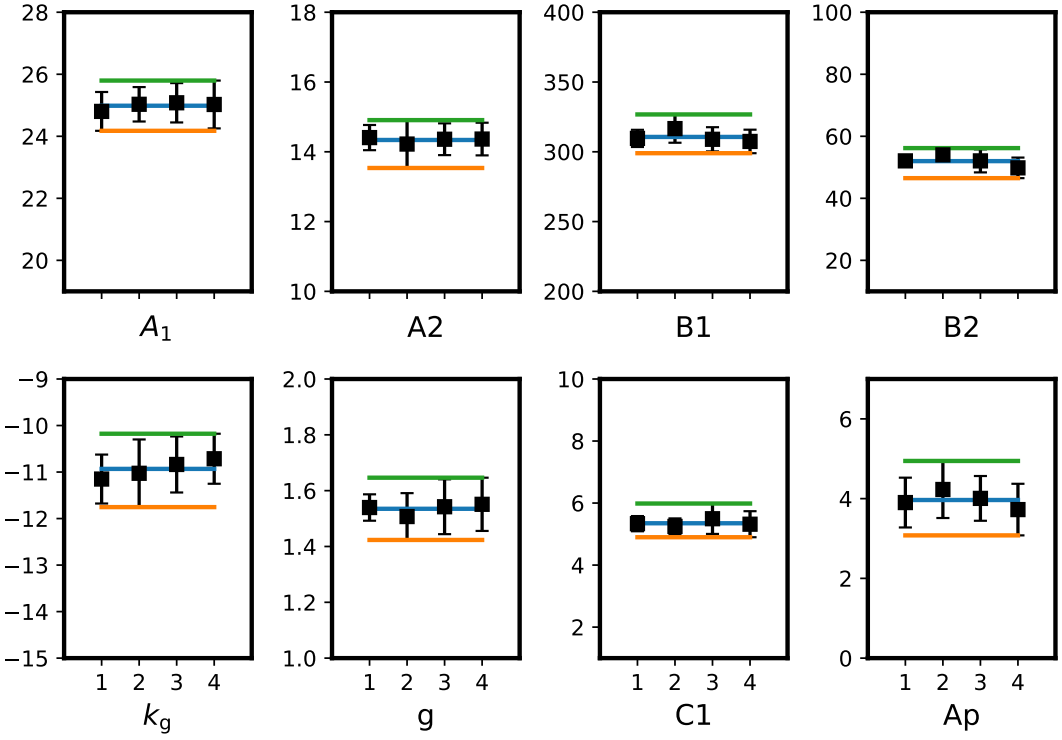

(d) 400 simulations

Figure B.12 Mirror model predictions using different dataset sizes (the four subplots) and different architectures (the x-axis of all the parameters in each subplot)

Figure B.12 reports the mirror model predictions for the four architectures at different dataset sizes and at a constant value of learning rate (10^{-4}) and epochs (5000). The comparison shows that (i) the architecture has little influence on the mirror model predictions and therefore the one reporting the largest standard deviation was chosen to be conservative and (ii) the dataset size beyond which the model predictions remain nearly unchanged is 200. After choosing the dataset size, the influence of learning rate on mirror model predictions was studied as shown in Figure B.13:

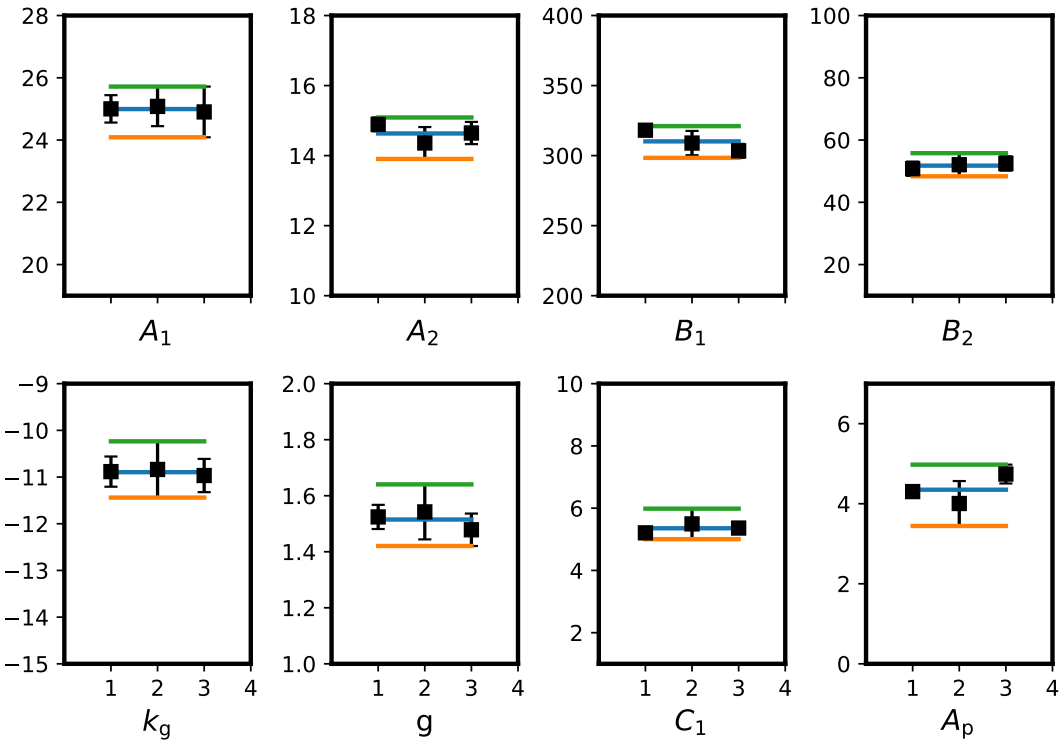

Figure B.13 Mirror model predictions using three learning rates: (1) 10^{-5}, (2) 10^{-4}, (3) 10^{-3}

Figure B.13 illustrates that the impact of the learning rate on mirror model predictions is limited. In contrast, Figure B.14 depicts the trend in loss, representing the disparity between predicted values and actual ground truth, across both training and testing datasets.

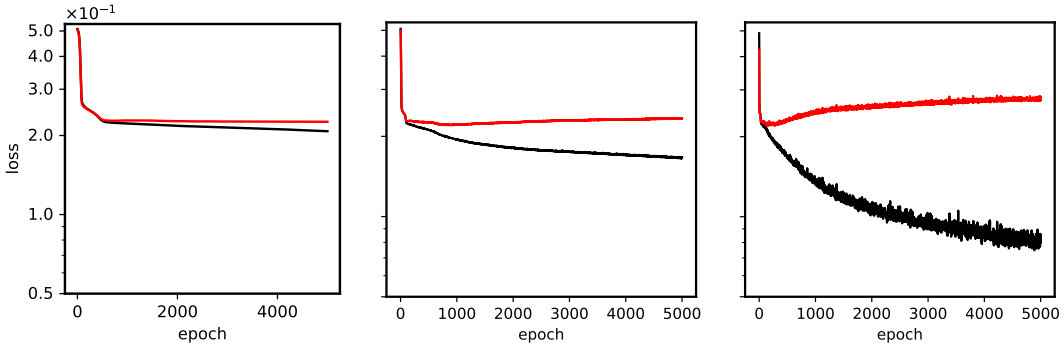

(a) (b) (c)

Figure B.14 Losses for the training (black) and testing (red) datasets for three learning rates: (a) 10^{-5}, (b) 10^{-4}, (c) 10^{-3}

While the model predictions exhibit minimal variation, the loss trends for the testing dataset (depicted by the red curves in Figure B.14) reveal three distinct patterns. The first trend, illustrated in Figure B.14-(a), lacks a discernible minimum. This suggests that the learning rate is relatively low concerning the number of epochs. However, this is not the case for the other two learning rates. Between the second (Figure B.14-(b)) and third (Figure B.14-(c)) trends, the former was ultimately chosen as a compromise between computational cost and accuracy of results.

B.9 PBM: average trend and confidence interval

The mirror model was employed to generate predictions based on experimental sizes under various operating conditions (dataset #1). Since there were five different operating conditions in dataset #1, five parameter vectors ($\overrightarrow{\varphi}$) were derived. Subsequently, we computed a vector that consists of both the average values ($\overrightarrow{\bar{\varphi}}$) and their corresponding standard deviations ($\overrightarrow{\bar{\varphi}'^2}$). We randomly selected 100 parameter vectors. For each parameter, the value ranged between $\overrightarrow{\bar{\varphi}}_i - \overrightarrow{\bar{\varphi}'^2}_i$ and $\overrightarrow{\bar{\varphi}}_i + \overrightarrow{\bar{\varphi}'^2}_i$. Subsequently, we conducted PBM simulations.